Construction and characterization of a Paul trap for laser spectroscopy of exotic radionuclides in an MR-ToF device

Master's Thesis in Physics

Presented by
Carina Kanitz
November 4, 2021

Lehrstuhl für Laserphysik
Friedrich-Alexander-Universität Erlangen-Nürnberg

Supervisor: Prof. Dr. Peter Hommelhoff (FAU)
Dr. Stephan Malbrunot (CERN)

Abstract

The Multi-Ion Reflection Apparatus for Collinear Laser Spectroscopy (MIRACLS) seeks to improve the sensitivity of Collinear Laser Spectroscopy (CLS) by confining ions of short-lived radionuclides in a Multi-Reflection Time-of-Flight (MR-ToF) device. In such an instrument an ion beam is reflected back and forth between two electrostatic mirrors. Thus, the novel MIRACLS apporach allows probing the ion several thousands of time compared to one single passage through an ion-laser interaction region in conventional CLS. After a successful proof-of-principle experiment establishing the technique, a new high-resolution instrument is currently under construction at the radioactive ion beam facility ISOLDE at CERN.

The MIRACLS technique requires a small energy spread of the injected ion bunch for high-resolution laser spectroscopy as well as a small time spread for the operation of the MR-ToF device. As these requirements are not fulfilled by the ISOLDE beam, a linear, square wave-driven Paul trap acting as radiofrequency cooler and buncher is built.

In this thesis, the optimal operation parameters of the MIRACLS Paul trap were determined in simulations and the resulting performance was characterized. This simulation study comprises the injection and trapping efficiency as well as the cooling process by buffer gas cooling. The ion bunching process was systematically studied in order to obtain optimal beam properties. The resulting ion bunches are suitable for the subsequent CLS measurements in MIRACLS' unique 30-keV MR-ToF device.

The progress in assembling the Paul trap and associated infrastructure is presented, along with the planned setup of a test beamline. Exploiting the latter, the Paul trap can be characterized before connecting it to the ISOLDE beamline, where space for beam diagnostics is limited. The process of fully commissioning the Paul trap is outlined.

Finally, an active voltage stabilization for high-voltage sources was implemented. This aims to improve the quality of the supplied ion bunches by reducing the energy spread induced by fluctuations in the voltage supplied to the electrodes. This is especially important for the acceleration potential once the ions are extracted from the Paul trap. The technique was tested on the mirror potentials of the MR-ToF device of the MIRACLS proof-of-principle experiment, which are particularly sensitive to voltage fluctuations. An improvement of 36% in the stability of the ion time of flight signal was achieved. Adding such a voltage stabilization to all mirror electrodes promises an even larger improvement in stability in the near future.

Contents

1 Introduction

The development of ion traps in the 1950s allowed for the first time to store ions over extended periods. This presented a breakthrough for atomic and molecular physics, also enabling precision tests of quantum electrodynamics (QED), as one fundamental force in the standard model of particle physics. In the 1970s those traps allowed to study single ions and electrons, laying the fundaments for precision spectroscopy experiments. Wolfgang Paul and Hans G. Dehmelt shared half of the Nobel prize in 1989 for the development of ion traps. W. Paul developed a trap where the confining field is generated by an alternating electric field, which was later named *Paul trap*.

Nowadays, Paul traps find application in a variety of fields, from chemistry over quantum physics to nuclear physics, as presented in this thesis. A main goal of modern experimental nuclear physics is to study nuclear properties of exotic, short-lived radionuclides, such as nuclear masses, binding energies, charge radii, or electric and magnetic moments of the nuclei. These measurements are used to benchmark theories, which seek to describe nuclear physics all across the entire chart of nuclides with one consistent theoretical framework.

Laser spectroscopy is a common experimental technique to access those nuclear properties. The transition energy of the electronic levels of the hyperfine structure in atoms or ions is determined by probing the electronic transitions with a laser. Nuclear properties can be extracted from these measurements, as the hyperfine structure is governed by the interaction of the electron cloud with the atomic nucleus.

At radioactive ion beam facilities, exotic isotopes can be synthesized, which are subsequently studied by a variety of experimental techniques, one of them being collinear laser spectroscopy (CLS). An often encountered obstacle to applying laser spectroscopy on very exotic isotopes is the low production yield of those isotopes together with the limited online time available for individual measurements. These combined result in insufficient statistics for measurements of the ‘most exotic’ radionuclides. The Multi-Ion Reflection Apparatus for Collinear Laser Spectroscopy (MIRACLS) seeks to overcome this limit of CLS by trapping the ion beam in a Multi-Reflection Time-of-Flight (MR-ToF) device. This novel approach allows probing the beam several thousand times compared to a single passage through an ion-laser interaction region in conventional CLS.

A prerequisite for the MIRACLS technique is that the ion beam is supplied in well-defined bunches with small time, energy, and spatial spread. Those requirements are not necessarily fulfilled by the ion beam provided by the ion sources at the radioactive ion beam facility ISOLDE at CERN, where the MIRACLS experiment is currently under construction. Therefore, the MIRACLS setup will feature a dedicated Paul trap, which prepares the beam for subsequent CLS studies in the MIRACLS MR-ToF device.

To this end, the ion beam from ISOLDE is injected into the Paul trap, where the ions are confined by an alternating radial electric field and a static longitudinal field, and cooled by collisions with buffer gas. The cooling process reduces the energy and spatial spread of the ion cloud in the trap. Following the completed cooling, the ion cloud is extracted from the trap as a temporally well-defined ion bunch.

In this thesis, the Paul trap for the MIRACLS experiment is characterized in simulations and the construction of the Paul trap is presented. In Chapter 2, the MIRACLS experiment at the ISOLDE facility is presented together with an overview of topics in modern nuclear physics motivating the experiment. In Chapter 3, the operating principle of a Paul trap is explained in more detail. A theoretical description of the ion motion in the trap is given, and a design overview of the Paul trap at MIRACLS is presented. In Chapter 4, the ion behavior in the Paul trap is simulated, mainly using the ion optical simulation software SIMION. These results identified the optimal operating parameters for the Paul trap. In Chapter 5, the mechanical and electrical design of the Paul trap is presented. The current status of a test beamline is shown. This will allow the MIRACLS collaboration to commission and characterize the performance of the Paul trap prior to online operation with short-lived radionuclides. In Chapter 6, the setup and results for an active voltage stabilization system for beamline potentials are presented, which can also be applied to the Paul trap to further improve the trap performance. Finally, the results are discussed and concluded in Chapter 7 and an outlook for future work and science opportunities is given.

2 Short-lived radionuclides and the Multi-Ion Reflection Apparatus for Collinear Laser Spectroscopy

In this chapter, the ISOLDE facility, that hosts the Multi-Ion Reflection Apparatus for Collinear Laser Spectroscopy (MIRACLS), and the methods of radioactive ion beam production are described. The technique of collinear laser spectroscopy and its role in nuclear physics is explained. The MIRACLS principle is introduced, which seeks to improve the sensitivity of collinear laser spectroscopy on radioactive ions by performing the measurements in an ion trap. Finally, the experimental setup of the MIRACLS experiment is presented.

2.1 The ISOLDE facility

Coupled to CERN's unique complex of particle accelerators, the Isotope Separator On-Line Device (ISOLDE) facility is a world-leading facility for the production of radioactive ion beams [1]. More than 1000 isotopes of over 70 different chemical elements can be synthesized and delivered to a variety of complementary experimental stations. A schematic drawing of the radioactive ion beam production area is shown in figure 2.1.

Protons with $1.4\,\mathrm{GeV}$ energy from the Proton Synchrotron Booster are directed onto the ISOLDE production targets, which are composed of different materials, depending on the isotopes of interest. In collisions of high-energy protons and target material, a variety of different radionuclides is created in nuclear fission, spallation, and fragmentation processes. The synthesized atoms diffuse out of the heated target and reach a suitable ion source. The ionization is achieved in the target-ion-source unit by surface or plasma ionization, or for an element-specific ionization, by the Resonance Ionization Laser Ion Source (RILIS) [3]. Subsequently, the ions are accelerated electrostatically to an ion beam energy of 30 to $60\,\mathrm{keV}$ and are separated according to their mass to charge ratio. For this purpose, ISOLDE features two magnetic mass separators, each linked to its own, dedicated target area. The general-purpose mass separator (GPS) has a mass resolving power of $R = {}^{m}/_{\Delta m} \approx 800$. The high-resolution mass separator (HRS) consists of two dipole magnets such that a mass resolving power of a few thousands can be achieved [4]. Ion beams delivered by HRS can be cooled and bunched by ISCOOL, a buffer gas-filled radiofrequency trap, similar to the later presented Paul trap of the MIRACLS experiment. Ion beams of GPS or HRS are finally transported via electrostatic beamlines to various experimental setups in the ISOLDE hall, one of which is MIRACLS.

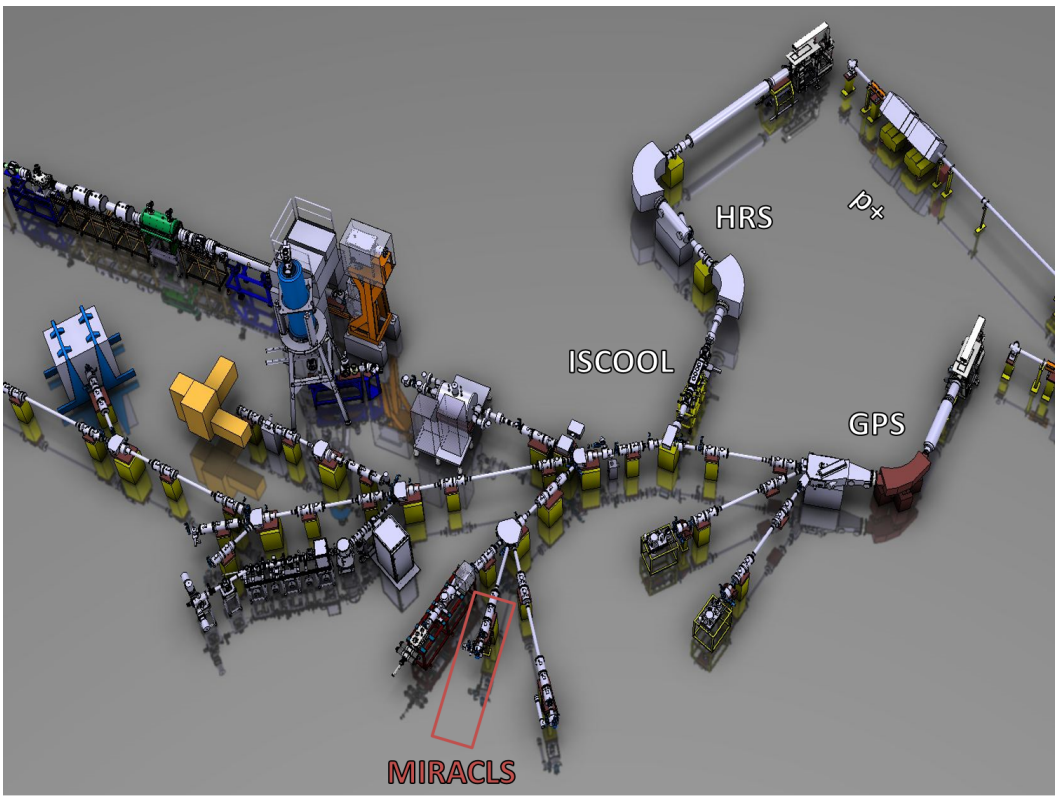

Fig. 2.1: Schematics of the production area for radioactive ion beams at ISOLDE and of select associated beamlines. Protons are delivered to two target zones that supply radioactive ions to two magnetic mass separators, HRS and GPS, respectively. Mass separated ion beams are subsequently delivered via electrostatic transfer beamlines to various experimental stations. The position of the MIRACLS beamline, currently under construction, is marked in red. Figure modified from [2].

One area of research at ISOLDE focuses on nuclear structure physics by determining nulcear properties of short-lived radionuclides such as their masses, charge radii, spins, electric and magnetic moments, half-lives, decay strengths, etc. These properties allow investigations of the shell structure of atomic nuclei, the shapes of nuclei or the overall behavior when approaching the driplines, i.e. the boundaries of proton and neutron numbers that allow the formation of bound nuclei. Additionally, research at ISOLDE is conducted in the fields of nuclear astrophysics, solid state physics, life sciences, and low-energy tests of the standard model of particle physics.

2.2 Collinear Laser Spectroscopy as a tool for nuclear physics

The nuclear shell model describes the ordering of protons and neutrons in separate shells, similar to the atomic shell model describing the ordering of electrons. This fundamental concept of low-energy nuclear physics is capable to explain a variety of nuclear properties and phenomena, most notably the prediction of magic numbers, i.e. a certain number of protons or neutrons leading to a shell closure and thus to nuclides of extraordinary stability and increased binding energy. Moreover, spin, parity, and magnetic dipole moments of nuclear ground states can be predicted.

However, far from the center of the chart of isotopes (the so-called *valley of stability*), a large imbalance in the number of neutrons and protons is encountered. In neutron-rich nuclides, some magic numbers are disappearing while other, new ones are emerging. This so-called shell evolution is not predicted by the classic nuclear shell model and its exact mechanism remains a major focus of contemporary research [5]. For certain mass regions on the nuclide chart, phenomenological theories have been developed and optimized to that region, which are very sucessful in reproducing nuclear observables. However, the ultimate goal of nuclear physics is to formulate a theoretical framework which is applicable to the entire range of nuclides and is derived solely from fundamental interactions. In this endeavor, *ab initio* theories present an appealing approach to model and calculate nuclear properties from first principles [5]. To this end, ab initio methods employ nuclear potentials, which are rooted in the underlying forces of quantum chronodynamics (QCD). Different approximation or simplification approaches exist to reduce the complexity of this computationally costly problem to a scale that presently allows the calculation of light to medium mass nuclei on high-performance computers [6].

To benchmark different theoretical models, experimental data in the regions far away from stability is of particular importance.Therefore, the measurement of nuclear observables of exotic short-lived radionuclides is one core aspect of modern nuclear physics. One tool for this endeavor is collinear laser spectroscopy (CLS), which allows experimenters to accurately determine spins, electromagnetic moments and charge radii of nuclear ground states and long-lived isomers [7].

Atomic spectroscopy aims to investigate the structure of the energy levels of electrons in an atom. In particular, laser spectroscopy probes the hyperfine structure (HFS) of an atom or ion. The gross structure of energy levels is described by non-relativistic

quantum mechanics without considering the spin of the electron. For hydrogen atoms it is governed by the principal quantum number n of the electron. The fine structure splitting is caused by the coupling of the electron spin and its orbital momentum l [8]. Additionally, relativistic corrections have to be considered in the fine structure. The hyperfine structure splitting is caused by the interaction of the electron cloud with the atomic nuleus. In particular, it is a consequence of the coupling of the total electron momentum **J** with the nuclear spin **I** to the total angular momentum $\mathbf{F} = \mathbf{I} + \mathbf{J}$. Considering the interaction of the electron cloud with the nucleus' magnetic moment, the energies of the hyperfine levels can be calculated by [8]

$$E_{\mathrm{HFS}} = A\langle \mathbf{I} \cdot \mathbf{J} \rangle = \frac{A}{2}\{F(F+1) - I(I+1) - J(J+1)\} \quad . \tag{2.1}$$

Here, $\langle \mathbf{I} \cdot \mathbf{J} \rangle$ denotes the expectation value of the product of nuclear spin **I** and total electron momentum **J**. A is a hyperfine structure constant, which can be expressed as

$$A = \frac{\mu B_e(0)}{\langle \mathbf{I} \cdot \mathbf{J} \rangle} \quad . \tag{2.2}$$

Here, $B_e(0)$ is the magnetic field generated by the electrons at the site of the nucleus and μ is the nucleus' magnetic moment. Hence, by measuring the hyperfine structure constant A, the magnetic moment of the atomic nucleus can be determined. A common technique to determine the magnetic moment without the knowledge of further atomic parameters is the comparison of the measured A value to a reference isotope of the same element [9]

$$\mu = \mu_{\mathrm{ref}} \frac{AI}{A_{\mathrm{ref}} I_{\mathrm{ref}}} \quad . \tag{2.3}$$

In a similar manner, the quadrupole moment and charge radius of a nucleus can be extracted from measured hyperfine spectra.

Experimentally, the hyperfine structure can be studied by laser spectroscopy. In the context of short-lived radionuclides, collinear laser spectroscopy is known for its high spectroscopic resolution [10]. In this technique a fast atom or ion beam is co-linearily overlapped with a laser beam. When the energy of the photons of the laser beam, characterized by the laser frequency, matches the energy of an electronic transition, the photon can be absorbed and the atom or ion is excited to a higher electronic level. These states are usually short lived and decay by emitting a photon to a lower energy level. By measuring the rate of emitted fluorescence photons as a function of the laser frequency, the hyperfine structure of the selected transition is revealed. The relevant frequency is the resonance frequency in the rest frame of the atom or ion. The laser frequency measured in the laboratory system is shifted by the (relativistic) Doppler effect due to fast moving ions. To vary the frequency in the rest frame of the ion, two methods exist: either the laser frequency itself is scanned or

the ions' velocity is varied while the laser frequency in the laboratory frame is kept constant.

2.3 The MIRACLS principle

In CLS measurements, the ion laser interaction time is limited to the time of flight through a dedicated CLS beamline region. This implies that the ions are usually probed by the spectroscopy laser during one single passage through the interaction region, typically lasting from a few $100\,\mathrm{ns}$ up to a few $\mu\mathrm{s}$. Moreover, the yield of exotic nuclei provided by radioactive ion beam facilities like ISOLDE can be as low as a few (tens of) ions per second. In combination with the limited time-availability of radioactive beams, as the facility is shared among numerous experimental programs, a variety of radionuclides is out of reach for conventional, fluorescence-based CLS as not enough statistics can be acquired to isolate the CLS signal from the photon background. The Multi Ion Reflection Apparatus for CLS (MIRACLS) aims to overcome this limitation by performing CLS in a Multi Reflection Time of Flight (MR-ToF) ion trap, such that an ion bunch can be probed for several ten thousand times compared to the single passage through the ion-laser interaction region in conventional CLS [11].

MR-ToF devices are nowadays well established in mass spectroscopy and allow separating different isobares with mass resolving powers exceeding $R = {}^{m}/_{\Delta m} > 10^5$. In an MR-ToF device, ion bunches are confined between two electrostatic mirrors. The latter consist of several ring electrodes to which electrostatic potentials are applied to create a barrier such that the ions are back-reflected. Hence, the ion beam of typically a few kiloelectronvolts energy is bouncing back and forth between the two electrostatic mirrors, see Figure 2.2. Between the two mirrors a field-free region, the central drift tube, is located. During confinement in the MR-ToF device, ions can accumulate a flight distance of several kilometers in a table-top instrument of a typical length of $\approx 1\,\mathrm{m}$.

For injection of the ion bunches, two techniques are available, as illustrated in Figure 2.3. The first technique is mirror switching, where the electrostatic potential of the mirror on the entrance side is lowered until the ion bunch enters the field-free region. The second technique is called in-trap-lift, in which the ions are injected with an energy high enough to pass above the mirror potential. At the moment when they are in the center of the field-free drift tube in the middle of the MR-ToF device, the potential of that drift tube is lowered, thus lowering the potential energy of the ions below the potential of the electrostatic mirrors. Thus, the ions are reflected from mirror to mirror until they are ejected, by applying once again the in-trap lift however in opposite direction or by lowering the potential on the mirror of the ejection side.

During their revolutions inside the MR-ToF ion trap, the ions are separated by time-of-flight (ToF) according to their mass. The mean kinetic energy of ions of different masses is the same as it is determined by the ions' starting potential U outside the MR-ToF device, which is common for all ions, e.g. the ions are often released from a

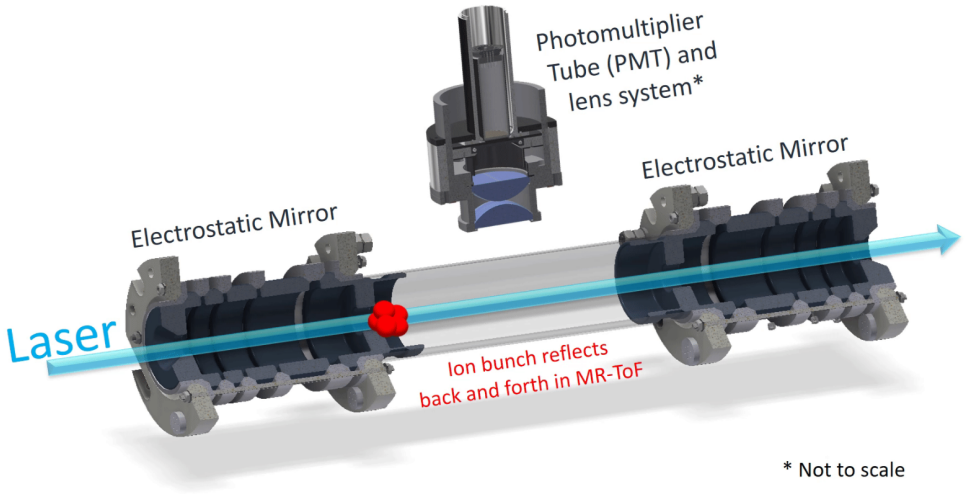

Fig. 2.2: Illustration of an MR-ToF ion trap designed for the purpose of CLS. Two ion mirrors consisting of several electrodes enclose the drift tube. The spectroscopy laser is co-linearly overlapped with the ion beam. Above, the optical detection system is mounted. See text for details. Figure taken from [12].

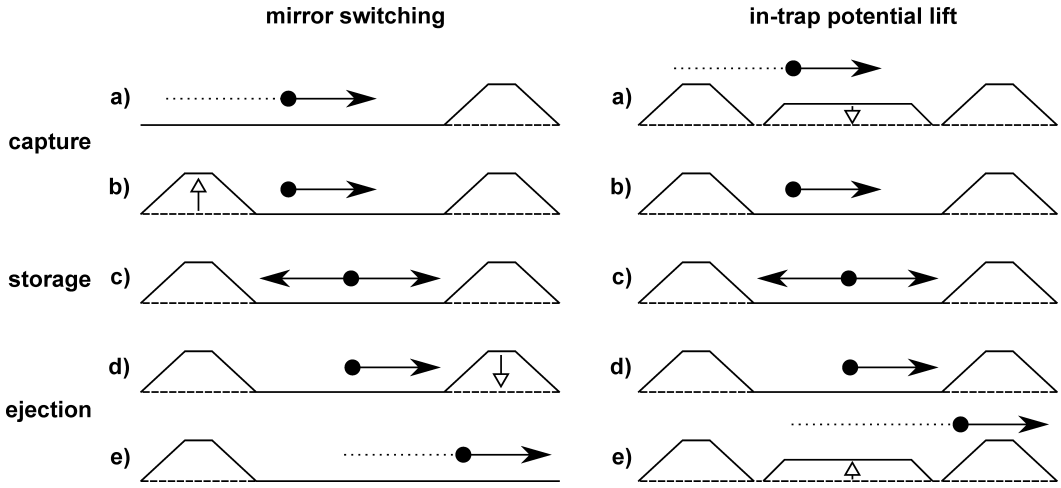

Fig. 2.3: Illustration of the two possible injection techniques. For the mirror switching technique (left), the potential of the mirror on the injection side is lowered, until the ion bunch passes the mirror. After increasing the potential again, the ion bunch is confined and bounces between the two mirrors until the mirror potential on the ejection side is lowered. For the in-trap potential lift technique, the ions are injected with sufficient kinetic energy to pass the mirror potentials. When the ion bunch is in the field-free drift tube, the electrostatic potential of the drift tube is lowered by a fast HV switch and with it the potential energy of the ion bunch. Again the ion bunch is confined. For extraction, the potential of the drift tube is increased again when the ions are in the center of the tube. For MIRACLS, the in-trap potential lift technique is applied. Figure taken from [13].

buffer gas filled Paul trap. This leads to different velocities v_i for different ion masses m_i,

$$v_i = \sqrt{\frac{2E_{\text{kin}}}{m_i}} = \sqrt{\frac{2z_i eU}{m_i}} \tag{2.4}$$

which results in a mass-specific revolution time, assuming the ions all possess the same charge $z_i e$. Due to the different revolution times, the ion species are drifting apart. The mass resolving power is defined by the total ToF of the ion species t and the temporal width of an ejected ion bunch Δt [14]

$$R = \frac{m}{\Delta m} = \frac{t}{2\Delta t} \quad . \tag{2.5}$$

Therefore, the temporal width of an ion bunch is limiting the mass resolving power. Several techniques exist to keep the dispersion of the ion bunch of one species in the MR-ToF and thus also Δt as low as possible, for instance by a specific shape of the ion mirror potential [15].

In order to perform CLS in an MR-ToF device, several modifications have to be performed, as illustrated in Figure 2.2. First, an optical detection region (ODR) has to be added to the central region of the MR-ToF ion trap. This is achieved by replacing parts of the central drift tube with a mesh with enhanced photon transparency. A photomultiplier tube (PMT) with a lens system is mounted above the mesh to detect the fluorescence photons. Second, laser access into the MR-ToF device has to be added. For this purpose, the ion beam needs to be electrostatically bent befor the MR-ToF such that the laser beam can be directed straight into the MR-ToF device.

The technique of CLS demands a small energy spread of the ion bunch to reduce the Doppler broadening of the line width measured in the experiment. For this reason, a buffer gas filled linear Paul trap is mounted upstream of the MR-ToF device. This ion trap cools the incoming beam and allows one to extract well-defined ion bunches with a small energy spread. Furthermore, it is desirable to increase the energy of the ion beam inside the MR-ToF ion trap from the usual few kiloelectronvolts to higher values, as the Doppler width scales as $\propto {}^{\delta_E}/\sqrt{E}$, where δ_E the energy spread within an ion bunch and E the ion beam energy [10]. For this reason, conventional single-passage CLS is typically performed at $E = 30 - 60\,\text{keV}$. At these energies, the width of the spectroscopic transition approaches the natural linewidth.

Additionally to the mechanical changes of the MR-ToF device, also the operation parameters have to be adapted to the requirements of CLS. In mass resolving mode, the highest priority is to keep the dispersion of the ion bunch low, i.e. to maintain Δt to be small. For the performance of CLS, a high ion-laser overlap is desirable to probe a high fraction of the ions contained in the bunch. The second important parameter is the angle of the ion trajectory to the beam axis, which contributes to the Doppler broadening and therefore should be minimized. New combinations of

potentials applied to the MR-ToF device's electrostatic mirror electrodes suitable for CLS were determined by a Monte Carlo simulation approach, see [16].

The concept of performing CLS in an MR-ToF ion trap was succesfully demonstrated in a MIRACLS proof-of-principle experiment in a low-energy ($1.3\,\mathrm{keV}$) MR-ToF device by measuring the isotope shift of stable magnesium isotopes [11]. Following the experiences gained in this work, a dedicated setup with an MR-ToF device specifically designed for CLS measurements and with an increased ion beam energy of $30\,\mathrm{keV}$ is currently being built.

2.4 The MIRACLS setup

The MIRACLS setup is designed to perform CLS on exotic nuclides supplied by ISOLDE in a $30\,\mathrm{keV}$-MR-ToF ion trap according to the above described MIRACLS principle [17]. A CAD model of the beamline currently under construction can be seen in Figure 2.4. The radioactive ion beam is delivered with typical energies of 30 - $60\,\mathrm{keV}$ either from the GPS beamline or from the HRS beamline as a pre-cooled beam from ISCOOL, see Figure 2.1. It is injected into MIRACLS' Paul trap. There, the ions are cooled by collisions with room-temperature helium atoms and, after a well-defined cooling time, are ejected from the trap as short ion bunches.

Following the ejection from the Paul trap, the ion bunches are accelerated to $2\,\mathrm{keV}$ and pass two ion-optical lenses with steering elements and a quadrupole bender, which lets the ion pass in a straight direction. Subsequently, the ions are passing a $30°$ deflector, which is needed to facilitate laser access into the MR-ToF device. The deflector also allows laser access into the Paul trap, for instance for the advanced cooling technique of laser cooling, as explained later in Chapter 4.4 [8]. Following the $30°$ deflector, the ions enter into another set of focussing and steering ion optics. At this point, the ions are leaving the floated beamline section, surrounding the Paul trap, and are accelerated further to $30-50\,\mathrm{keV}$. Finally, they are injected and captured in the MR-ToF device via the technique of in-trap lift switching and the CLS measurements are performed. After a set number of revolutions, the ions are ejected from the MR-ToF device and impinge on a retractable ion detector, which can be used for ion-beam optimization.

The MR-ToF device operates at an energy of $30\,\mathrm{keV}$ and is specifically designed for performing CLS measurements. One of the added features is the large optical detection region consisting of three rows of two PMTs each. This increases the sensitivity of CLS measurements and also allows to study the laser ion interaction over a larger region of the MR-ToF device. Furthermore, a highly UV light absorbing black coating inside the chamber and on apertures in front of the optical system is used to suppress stray light and hence, increase the signal-to-noise ratio of the measurement. Through those properties, the MIRACLS setup will allow performing CLS on isotopes currently out of reach for regular CLS experiments. Advantages of the high energy MR-ToF device, in addition to the MIRACLS operation itself, are a faster mass separation time and an improved ion capacity. Both will be critical features of a future ISOLDE MR-ToF device, which will provide purified ISOLDE beams to downstream experiments. Hence, in addition to its own CLS science

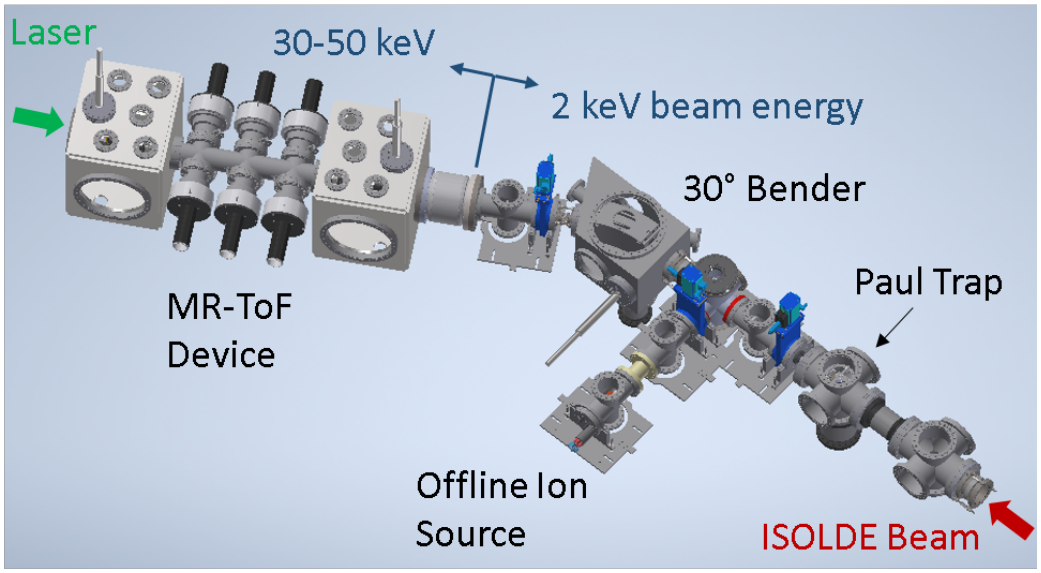

Fig. 2.4: CAD model of the MIRACLS beamline. The radioactive ion beam enters the beamline in the direction of the red arrow. In the Paul trap the ions are accumulated, cooled and bunched. Cold ion bunches are reaccelerated to $2\,\mathrm{keV}$ and directed towards the $30°$-bender, which guides the ion beam onto the laser beam axis. Finally, the ions are accelerated to $50\,\mathrm{keV}$ before entering the MR-ToF device, where the CLS measurements are taking place.

program, the MIRACLS setup will serve as a prototype of such a general purpose ISOLDE MR-ToF mass separator.

For commissioning and optimization purposes, the setup also features an offline ion source, see Figure 2.4. It is floated to $\approx 2\,\mathrm{kV}$, such that the ions from this ion source are accelerated to $2\,\mathrm{keV}$ as explained before. Via a quadrupole bender, the ions are deflected by $90°$ onto the Paul trap axis and injected through the downstream end of the Paul trap in a so-called reverse injection. This configuration was necessary due to space constraints at the beamline site at ISOLDE. The focusing and steering ion optics between the quadrupole bender and Paul trap, as well as the quadrupole bender are controlled by fast high voltage (HV) switches to apply the electrostatic potentials to the optical elements as necessary for each transport direction.

The beamline section following the first vacuum cross of the MIRACLS beamline, is floated to a high potential, to decelerate the ISOLDE beam. The Paul trap itself is floated to a potential corresponding to almost the energy of the ion beam, such that the remaining energy of the ions is sufficiently low to facilitate the trapping, typically a few eV. The following beamline is floated to a potential $2\,\mathrm{kV}$ lower than the Paul trap, such that the ion bunches extracted from the Paul trap are accelerated to an beam energy of $2\,\mathrm{keV}$. The steering, focusing, and bending the ion beam onto the laser axis is performed in the high potential region, before the ions are accelerated towards the ground potential of the MR-ToF device. The beamline segments of different potentials are separated by ceramic insulators and the whole high potential region is encaged for HV safety.

3 Linear Paul traps as ion coolers and bunchers

In this chapter, the general operational principle of a Paul trap is presented. The theoretical description of the ion motion inside the trap is derived for a classical sinusoidal-driven Paul trap as well as for a squarewave-driven Paul trap. The mechanism of ion cooling via the two techniques of buffer-gas cooling and laser cooling is explained. The principle of ion bunching in the trap is described and the properties of the extracted ion bunch in terms of beam emittance are discussed. Finally, the design of the Paul trap for the MIRACLS experiment is presented.

3.1 Paul trap principle

Earnshaw's theorem states that charges in a static electric field cannot form a stable equilibrium, as no local electric field minima can exist in free space, only saddle points [8]. For trapping ions in three dimensions, therefore, either magnetic fields or dynamic electric fields are employed. In a Paul trap, an ion-confining electric quadrupole field is generated by applying a radiofrequency (RF) field between a set of opposing electrodes. Averaged over time, this results for ions in an attractive force towards the center of the trap.

In linear Paul traps, a two-dimensional quadrupole field is generated by a set of four hyperbolic rods, to which the RF potentials are applied in order to confine ions radially, see Figure 3.1. An additional electrostatic potential is used to confine the ions in the longitudinal direction of the trap.

In the following, z will describe the longitudinal coordinate of the trap and x and y the radial coordinates. When a voltage $V(t) = \pm 1/2 V_0 \cos(\Omega t)$ is applied between the two pairs of rod electrodes, which are separated each by a distance of $2r_0$, a quadrupole potential

$$\Phi = \frac{V_0}{2r_0^2} \cos(\Omega t)(x^2 - y^2) \tag{3.1}$$

is generated [8]. The electric field for deriving the equations of ion motion in the trap is calculated by the Laplace equating, which strictly speaking is only allowed for a static potential. The treatment of the potential by electrostatic methods is justified as the wavelength corresponding to frequencies usually employed for ion trapping ($\approx$ MHz) are far longer ($\approx 300\,\mathrm{m}$) than the length of the rod electrodes

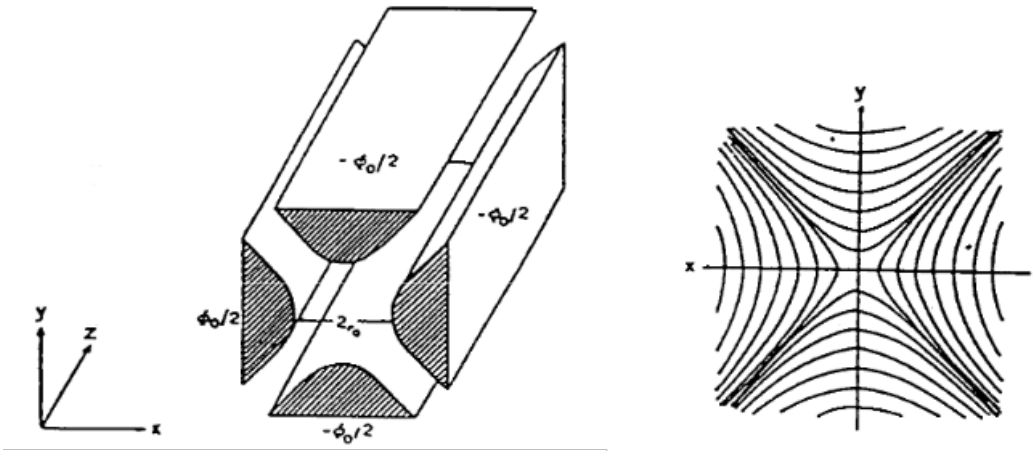

Fig. 3.1: Drawing of the quadrupole generating electrodes of a linear Paul trap and the resulting field lines. For trapping the ions in three dimensions, an additiona static field is applied at the front and at the back of the trap. Figure taken from [18]

[8]. According to $E = -\nabla\Phi$, the electric field E can be obtained and the equation of motion for a particle of charge e and mass m in the electric field is expressed by

$$m\ddot{x} = -\frac{eV_0}{r_0^2}\cos(\Omega t)x \quad , \tag{3.2}$$

analogous, but with opposite sign, for the y-direction. Equation 3.2 can be compared to the Mathieu equation [8], substituting $\tau = {}^{\Omega t}/_{2}$, known from mechanical physics:

$$\frac{d^2x}{d\tau^2} + (a_x - 2q_x\cos(2\tau))x = 0 \quad . \tag{3.3}$$

Here,

$$q_x = \frac{2eV_0}{\Omega^2 m r_0^2} \tag{3.4}$$

and

$$a_x = \frac{4eV_{\mathrm{r,DC}}}{\Omega^2 m r_0^2} \tag{3.5}$$

represent the stability parameters of the differential equation, where $V_{\mathrm{r,DC}}$ is the static potential applied between the RF electrode rods. For this thesis, $V_{\mathrm{r,DC}} = 0$, and thus $a = 0$ is assumed. Figure 3.2 illustrates the stability diagram of the solutions dependent on the parameters q and a. The stability regions describe combinations of operation parameters that lead to stable ion trajectories, i.e. trajectories on which

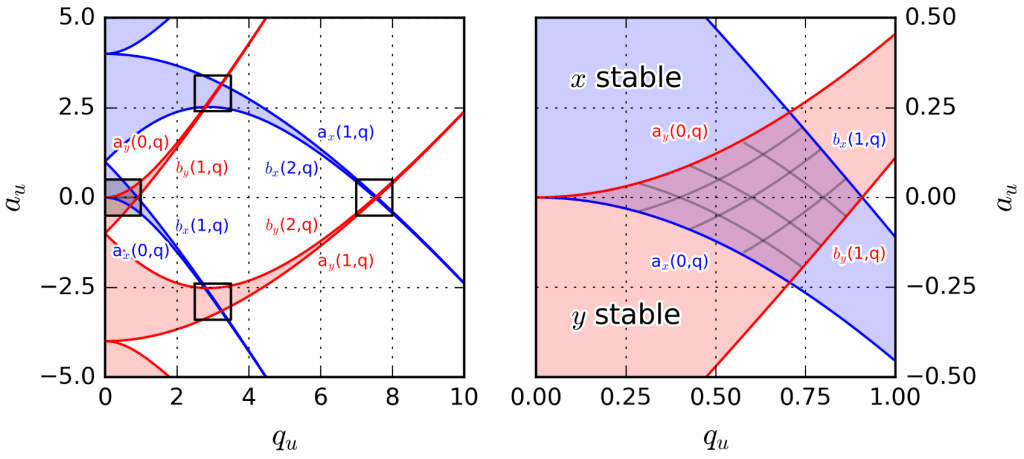

Fig. 3.2: Stability diagram of the solutions of the Mathieu equations dependent on the parameters a_u and q_u. Colored regions are stable in the respective direction, bold lines present the edges of stability. $a_x\,(l,q)$ and $a_y\,(l,q)$ denote even Mathieu functions, $b_x\,(l,q)$ and $b_y\,(l,q)$ odd Mathieu functions. $l \in \mathbb{Z}$ numerate the solutions, that present a transition from stable to unstable solutions. Only regions with stability in x- and y- direction represent an overall stable solution. On the right, a magnification of the first stability region is shown, shaded in grey in the left plot. Figure taken from [19].

an ion remains confined in the ion trap. The first region of stability (shaded grey in Figure 3.2) is usually chosen for the Paul trap operation, as RF fields with lower amplitude are required than for the higher regions. For $a = 0$, this means that for $q \lesssim 0.9$ the trajectories are stable and the ions remain trapped.

The solutions of the Mathieu equation show that the ion motion in the linear Paul trap is composed of a fast oscillation with the frequency of the RF field applied to the electrodes, the so-called *micromotion*, and a slow oscillation with larger amplitude, the *macromotion*:

$$\omega_{\text{macro}} = \frac{q_x \Omega}{2\sqrt{2}}, \quad A_{\text{macro}} = x_0 \tag{3.6}$$

$$\omega_{\text{micro}} = \Omega, \quad A_{\text{micro}} = x_0 \frac{q_x}{2} \tag{3.7}$$

The amplitude of the macromotion A_{macro} depends on the initial position x_0 of the ion in the trap. Due to symmetry, the same solution to the equation of motion is valid for the y-direction and the macromotion frequency will be referred to as the radial frequency ω_r. The macromotion can be approximately described as a motion in a radial harmonic potential [20]

$$\Phi_{RF}(r) = \frac{q_r V_0}{8 r_0^2} r^2 \quad . \tag{3.8}$$

In a linear Paul trap, the ions are confined in longitudinal direction by an electrostatic potential by applying a voltage to the endcaps of the trap, to segmented quadrupole electrodes or to independent DC electrodes in close proximity to the quadrupole rods. Although the details of the axial potential depend on the details of the geometry and applied DC potentials, the potential close to the potential minimum can be approximated by a harmonic potential along the trap's axis z

$$\Phi(z) = \frac{V_{DC}}{z_0^2} z^2 \quad . \tag{3.9}$$

Here, z_0 is a geometric parameter of the longitudinal potential, determining the depth of the trapping potential together with V_{DC} [21]. In this potential well the ions are oscillating axially with a frequency

$$\omega_z = \sqrt{\frac{2eV_{DC}}{mz_0^2}} \quad . \tag{3.10}$$

The ions are longitudinally trapped when the kinetic energy is lower than the potentials applied to the endcaps.

When the potential in longitudinal direction is non-negligible compared to the radial trapping potential, the effective pseudo-potential, combining the two potentials should be considered [20] [1]

$$\Phi_{\text{eff}}(r, z) = \frac{V_{DC}}{z_0^2} z^2 + \left(\frac{q_r V_0}{8 r_0^2} - \frac{V_{DC}}{2 z_0^2} \right) r^2 \tag{3.11}$$

Thus, a deep axial trap reduces the trap depth in radial direction.

3.2 Digital Ion Trap

In a digital ion trap, the sinusoidal RF field is replaced by a square-wave voltage signal. This replacement exhibits several advantages, especially a simplification of the electronics used to control the trap and the possibility to change the trap frequency in a wider range, which is useful for trapping ions of different masses [22].

[1] This equation for the effective potential does not fulfill $\Delta\Phi = 0$ as the time-dependent potential radial potential is approximated by the static potential (see equation 3.8). Using equation 3.1 for the radial component, results in an expression for the potential, that fulfills the Laplace equation.

For a rectangular wave with a 50% duty cycle, the voltage supplied to one pair of electrodes is

$$V_\delta(t) = \begin{cases} \frac{V_0}{2} & \text{for } 0 < t \leq \frac{T}{2} \\ -\frac{V_0}{2} & \text{for } \frac{T}{2} < t \leq T \end{cases} \tag{3.12}$$

with T the period of the voltage signal. For the other electrode pair the same potential but with opposite sign is applied. This voltage signal generates a quadrupole potential as in the case before. The equations of motion become [23]

$$m\ddot{x} = -\frac{e}{r_0^2} V_\delta(t) x \quad . \tag{3.13}$$

By substitution of t for τ with $\Omega = {}^{2\pi}/_{T}$, introducing $u = {}^{\Omega^2}/_{4}x$ and using the stability parameter q as before, the equations can be brought into the form of Meissner equations [23]:

$$\frac{d^2u}{d\tau^2} \pm 2qu = 0 \tag{3.14}$$

The stability criterion is known from the theory of Hill's equations, to which the Meissner and also the above used Mathieu equation belong. It is found, that $q < 0.712$ results in stable ion trajectories [23]. Once again, the solutions show a fast oscillation component with the frequency of the driving field Ω, the micromotion. The second part of the solution is a Fourier series composed of the frequencies [23]

$$\omega_n = |\omega_s + n\Omega| \tag{3.15}$$

with $n \in \mathbb{Z}$. The frequency of the dominant motion, the secular frequency ω_s, is given by

$$\omega_s = \frac{\beta\Omega}{2} \tag{3.16}$$

with

$$\beta = \frac{1}{\pi} \arccos[\cos(\pi\sqrt{\frac{q}{2}}) \cosh(\pi\sqrt{\frac{q}{2}})] \quad . \tag{3.17}$$

As an approximation, for small q values it is often assumed that the motion can be described by a harmonic oscillation with the secular frequency. The depth of this pseudo-potential is given by [24]

$$D = \frac{m\omega_s^2}{2e} r_{max}^2 \approx \alpha q V_0 \quad , \tag{3.18}$$

where α is a correction factor for the digital trap potential. In a sinusoidal driven linear Paul trap $\alpha = 1/8$. For a digital ion trap and $q < 0.3$, $\alpha \approx 0.206$, which implies that for the same applied RF amplitude, a square wave driven trap exhibits a trapping potential which is a factor of ≈ 1.5 deeper. In this work $q = 0.4$ was chosen to achieve a higher trapping efficiency, as demonstrated later. For this q value the correction factor α cannot be easily estimated analytically.

In summary, the motion of ions confined in a (linear) Paul trap is well understood. It can be described by a set of analytical functions for both sinusoidal and square wave driven linear Paul traps. The analysis of those equations of motion reveals well defined stability regions, for which stable ion confinement is achieved.

3.3 Ion Cooling

At radioactive ion beam (RIB) facilities, linear Paul traps are commonly employed as cooler-bunchers to accumulate and cool a continuous ion beam of exotic radionuclides. These ions are subsequently released in ion bunches of well-defined temporal width. Given its simplicitiy, efficiency, and element universality, buffer-gas cooling is typically applied in cooler-bunchers at RIB facilities. In this technique 'hot' incoming ions are thermalized by collisions with the 'cold' buffer gas leaked into the ion trap. As the ions loose energy in these collisions, they 'cool down' into the trap minimum while newer hot ions enter the trap. Furthermore, this buffer-gas cooling allows reducing the energy and time spread of the extracted ion bunches, which is a critical requirement for CLS measurements in the MR-ToF device.

The decrease in ion energy through the elastic collisions with the cold buffer-gas atoms can be described in a linear drag model with the damping force F proportional to the ion velocity v leading to an exponential decrease of energy over time:

$$F = -\delta m v \tag{3.19}$$

where

$$\delta = \frac{e}{m\mu} \frac{p/p_N}{T/T_N} \tag{3.20}$$

with μ being the ion mobility in the buffer gas. p and T are pressure and temperature of the buffer gas relative to normal pressure $p_N = 1013\,\mathrm{mbar}$ and normal temperature $T_N = 273.16\,\mathrm{K}$, respectively [20].

The ions are cooled until the equilibrium temperature of the ions is reached. In longitudinal direction, the equilibrium temperature is determined by the temperature of the buffer gas T. The temperature in radial direction is additionally influenced by the process of RF reheating: collisions between ions and buffer-gas atoms in the dynamic radial potential lead to a heating effect of the ions [25]. As the motions in longitudinal and radial direction are not coupled in a first order approximation, the temperatures in radial and axial direction will thus not be equal.

In the pseudo-potential approximation of a sinus-driven Paul trap, the final radial temperature can be estimated by [25]

$$T_{\text{eff}} = \frac{2T}{(1 - \frac{m_g}{m})} \tag{3.21}$$

where m is the mass of the ion and m_g is the mass of the buffer-gas atom. For the square-wave operated Paul trap no analytical description for the RF heating process could be found in literature.

Laser cooling is another cooling technique applied in ion traps, which can reach sub-Kelvin ion temperatures. It is routinely employed in precision experiments with stable ion species [26, 27]. However, it has been exploited for short-lived radioactive ions only in specific applications [28, 29]. As part of the MIRACLS project it has been successfully demonstrated that laser cooling can be utilized also for ion beam preparation of radionuclides. By sympathetic cooling with co-trapped laser-coolable ions, a 'universal' technique to obtain ultra-cold radioactive ions has been developed [30].

The laser cooling method employed as part of this work is also called Doppler cooling [26]. A laser beam of suitable wavelength is directed into the Paul trap. When an ion absorbs a photon moving in the opposite direction as the ion, the ion is decelerated due to momentum conservation. To achieve a deceleration, but no acceleration effect for ions moving in the same direction as the laser, the laser wavelength is slightly red detuned from the resonance frequency of the electronic transition used. In this case only ions, which move opposite to the direction of the laser beam, can absorb a photon due to the Doppler-shift of the frequency in their frame of reference. When the excited state decays, a photon is emitted in a random direction, changing again the momentum of the ion. As the direction of the momentum gained by the emission process is randomly distributed, it results in no change in momentum when averaged over many emission processes. In contrast, the loss of momentum by the absorption process always happens in the same direction. This leads to a net cooling of the ions.

Prerequisite for the cooling is a closed level system in the laser-cooling transition which allows repeated photon absorption. The limit for laser cooling of ions is given by the Doppler cooling limit $T = \hbar\Gamma/2k_B$ where $\hbar$ is the reduced Planck constant and

Γ the linewidth of the electronic transition [8]. For typically used fast transitions, the attainable temperature is much lower than temperatures reachable in buffer-gas filled traps. Since radial and axial ion motion are decoupled in the ion trap, laser cooling on single ions is only effective in the direction of the laser beam. If the laser beam is directed along the longitudinal axis of the Paul trap, only the longitudinal motion can be damped.

Sympathetic cooling can be employed when the ion species of interest is not suitable for direct laser cooling, for instance due to a multilevel electronic structure [31]. In this case, an additional ion species, that is laser-coolable can be co-trapped with the species of interest. The laser cooled species cools the second species via collisions and space-charge effects.

In the context of radioactive ion-beam facilities, buffer-gas cooling is generally employed in Paul traps, which act as cooler and bunchers. This is a consequence of the ease of operation. While laser cooling of ions has been used for dedicated experiments, work at MIRACLS and as part of this thesis has successfully demonstrated laser and sympathetic cooling as 'universal' tools to obtain cold ion bunches for subsequent experimental instruments [30]. As shown at MIRACLS, this can be done in a time frame compatable with short half lives of $<1\,\mathrm{s}$ and in existing instruments available at RIB facilities.

3.4 Ion Bunching

The Paul trap is capable of accumulating and transforming a continuous ion beam into a bunched beam, i.e. a beam consisting of temporally separated bunches of ions, each of which is typically as short as a few nano to microseconds. To this end, the potential on the injection endcap is lowered and ions from the continuous beam are entering the Paul trap. There they are trapped by the radial and axial confining potentials and cooled by collisions with the buffer gas. After a well-defined *loading time*, the potential at the endcap is increased again to prevent additional ions from entering the trap. This allows for thermalization of all ions in the buffer gas until, after the *cooling time*, the ions are extracted from the trap. For the extraction, the potential applied to the extraction endcap is lowered to accelerate the ions out of the trap.

The extracted ion bunches can be characterized by their beam emittance. The longitudinal emittance is defined by the area, which the ions 'occupy' in the energy-time (E-t) action plane, i.e. the projection of the phase space on the 2-dimensional E-t plane. Quantitatively, this can be expressed by the root-mean-square emittance [32]

$$\epsilon_{rms,\mathrm{long}} = \sqrt{< E^2 >< t^2 > - < Et >^2} \quad . \tag{3.22}$$

Here, $< E^2 >$ denotes the variance of the energy and $< t^2 >$ the variance of the time of flight. If E and t are not correlated, equation 3.22 simplifies to $\epsilon_{rms,\mathrm{long,\,n}} = \sigma_E \cdot \sigma_t$ where σ_E is the ion bunch's energy spread and σ_t its temporal width at the time

focus point. Other definitions of emittance are common as well, for instance, the $\epsilon_{95\%}$ emittance, i.e. the area in the action plane which envelops 95% of all ions. If the ion distribution is Gaussian, $\epsilon_{95\%}$ can be calculated from ϵ_{rms} by multiplying the latter with a factor of 6 [23]. For ions extracted from the Paul trap, the longitudinal emittance can be estimated by calculating the phase space that is filled by the ions confined in a harmonic potential and in thermal equilibrium with the buffer gas [33]

$$\epsilon_{rms,\text{long}} \approx \pi \frac{k_B T}{\omega_z} \quad . \tag{3.23}$$

Here, ω_z represents the longitudinal oscillation frequency as defined in equation 3.10.

The transversal emittance is defined by the position x and momentum p_x of the ion transversal to the main beam direction [32]

$$\epsilon_{rms,\text{trans, n}} = \sqrt{< x^2 >< p_x^2 > - < x p_x >^2} \quad . \tag{3.24}$$

The subscript n denotes that the emittance is normalized with respect to the beam energy, i.e. the normalized beam emittance does not change, when the beam is accelerated or decelerated. For the transversal emittance, the unnormalized emittance is often used which is given in units of $\pi\,\mathrm{mm\,mrad}$. The normalized emittance is related to ϵ by $\epsilon_n = \epsilon p$, where p is the average momentum of the ions in the direction of the beam propagation.

For ions extracted from a Paul trap, the transverse emittance can be estimated by [33]

$$\epsilon_{rms,\text{trans}} \approx \pi \frac{k_B T}{\omega_r} \quad . \tag{3.25}$$

According to Liouville's theorem the occupied volume in the 6-dimensional phase space is conserved when the bunch is exclusively subjected to conservative forces. As long as the equation of motions are not coupling transverse and longitudinal motions and higher-order, non-linear forces can be neglected, the areas of the projections, i.e. longitudinal and (normalized) transversal emittance are themselves individually conserved as well [34]. To first order this is the case for ion acceleration and ion optics along beam transport. Thus, the emittance is a very useful concept to describe ion beam properties. In the Paul trap itself, the phase space of the incoming beam is reduced by cooling the ions, which is a non-conservative process.

3.5 The Paul trap for MIRACLS

In the MIRACLS experiment, the Paul trap cools and bunches the incoming online or offline beam for the subsequent injection into the MR-ToF device. One key requirement is that the Paul trap needs to be able to accept and trap the ISOLDE online beam with minimal ion losses. As far as the beam quality of the ejected ion bunches is concerned, the requirements are dictated by the combination of the two measurement methods; for CLS a low energy spread is required to reduce Doppler broadening, while for the MR-ToF operation ion bunches narrow in time are needed. At the same time, the ion bunches should possess a small spatial spread (for optimal ion-laser overlap) and close to parallel trajectories in the MR-ToF device (again to minimize the experimental CLS line width). The time and energy spread cannot be minimized at the same time, due to the conservation of longitudinal emittance, see equation 3.22. The same is true for the transverse spread in space and momentum, of which latter translates into an angular spread. Thus, a suitable trade-off has to be found for the trap design and operation parameters. The mechanical design and verification of the design in ion-optical simulations were performed by Simon Lechner [35].

Three dimensional CAD models of the MIRACLS Paul trap can be seen in Figure 3.3. It is a linear segmented Paul trap with separated RF and DC electrodes. The cylindrical DC electrodes are used to define the longitudinal trapping potential and position of the trapping minimum in addition to applying potentials at the endcaps. The DC electrodes are manufactured in two different lengths, the thinner electrodes are positioned around the trap minimum to control the field more precisely. The RF electrodes are produced as segments of cylindrical rods, which are easier to manufacture than hyperbolic surfaces.

In the cross-section of the Paul trap in the left image of Figure 3.4 it can be seen that the four RF rods are surrounded by the DC electrodes. The DC electrodes feature wedges reaching into the space between the RF rods to enhance the static field that is partially shielded by the RF rods. Additionally, this has the advantage that the capacitance of the RF electrodes to each other is reduced, which allows achieving

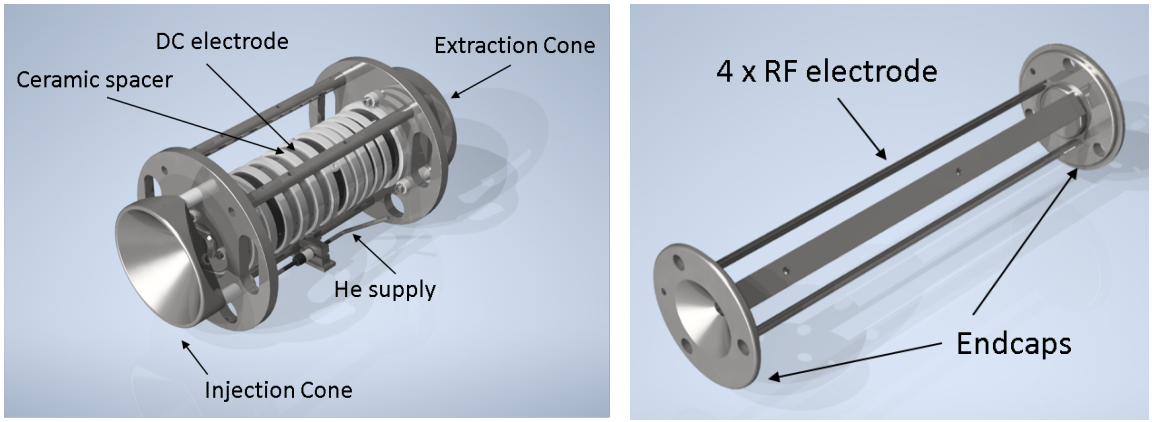

Fig. 3.3: CAD model of the Paul trap for MIRACLS (left) and the RF electrodes and endcaps on the inside of the trap (right).

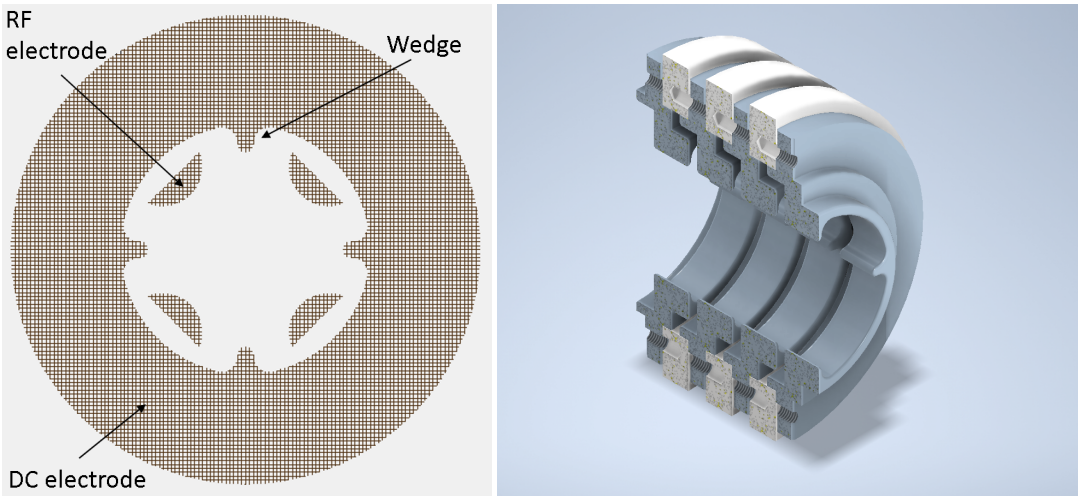

Fig. 3.4: Left: Schematic of the electrode structure in cross sectional view of the Paul trap. The RF electrodes have a radius of $5\,\mathrm{mm}$ and a height of $2.5\,\mathrm{mm}$. The DC electrodes possess a $60\,\mathrm{mm}$ outer diameter and $32\,\mathrm{mm}$ inner diameter. Right: Axial cross sectional view through the DC electrodes (blue) and ceramic insulators (white).

a more accurate waveform of the squarewave voltage signal supplied to the RF electrodes.

The cones at both ends of the Paul trap, see left image of Figure 3.3, provide a large acceptance by decelerating and focusing the incoming beam into the small aperture of the endcap. The aperture of $5\,\mathrm{mm}$ diameter was chosen as a compromise, to allow a large fraction of the incoming beam to enter the trap while limiting the pressure increase around the trap due to helium atoms escaping the trap. To enclose the helium inside the trap and for electrical insulation between DC electrodes, ceramic spacers are placed between the DC electrodes. The DC electrodes are axially formed in a way that no insulator is ever exposed to the ions, see right image of Figure 3.4. This prevents 'lost' ions to accidentally reach the insulators which could alter the electric field inside the Paul trap in an uncontrolled manner.

The evaluation of the optimal operation parameters for this Paul trap design through simulations, such as the RF amplitude and frequency, the DC trapping potential, and the helium pressure, is presented in the next chapter.

4 Simulation of the Paul trap operation

In this chapter, the ideal parameters for operating the Paul trap and its expected performance are determined in simulations. After introducing the simulation methods, the ion transfer from the offline ion source into the Paul trap is optimized. Next, the injection efficiency is studied in dependence on the buffer gas pressure, floating potential, and RF parameters. The cooling process of the ions is explained and the ion motion in the trap is visualized. The properties of ion bunches extracted from the Paul trap are studied in terms of their emittance when the used extraction potential is varied. Finally, gas-flow simulations of the buffer-gas pressure in the MIRACLS beamline are performed to gauge the vacuum performance of the setup.

4.1 Ion-optical simulation methods

In order to simulate the trajectories of ion motions in the electrostatic and RF fields the software package SIMION (version 8.2.0.5) was used [36]. It was used to study the ion injection to, the extraction from, as well as the ion motion in the trap itself.

To this end, electrode geometries are defined and the field in between is calculated by solving the Laplace equation by finite difference methods. In the approach applied in this thesis, the field is calculated separately for each electrode and the fields are combined later with the electrode potential as a weighting factor in a linear combination according to the principle of superposition. This allows adjusting the potentials applied to the electrodes without solving the Laplace equation a second time. Thus, different combinations of potentials applied to the fixed geometry can be simulated in a time-efficient manner. In the resulting field, the ion motion is simulated by creating the ions according to the defined initial conditions and calculating the trajectory for small time steps employing a 4th order Runge-Kutta technique. If an ion hits the surface of an electrode, the trajectory is ended and the ion is lost. In the simulations presented here, no ion-ion interactions are considered.

Additional effects can be implemented via a user program, written in the Lua language. In this work, the RF voltage supplied to the RF rods of the Paul trap is implemented by reassigning the potential applied to the electrodes with the desired frequency. The duration of a time step in simulation is adjusted to be maximally $1/10$ of the RF period.

The interaction of the ions with buffer gas is implemented in terms of a hard-sphere model [37], i.e. the collisions of the ions with the buffer-gas atoms are treated as collisions of inelastic spheres. The velocities of the buffer gas follow a Maxwell-

Boltzmann distribution according the assigned temperature. The temperature of the buffer gas is assumed to not change in interactions with the ions. Furthermore, the trajectories of the buffer-gas atoms are not simulated. For each timestep a propability that an ion-atom collision occurs is calculated based on the mean free path of the ion in the gas and the velocity of the ion. Then a random number is generated and, given the collision probability, it is evaluated whether a collision takes place. In case of a collision, the flight direction and energy of the buffer-gas atom are randomly assigned, considering the Maxwell-Boltzmann distribution at the assigned gas temperature. Finally, the effect of the collision on the ion is calculated, i.e. the direction, velocity, and energy of the ion are adjusted. The mean free path l of the ion in the gas is

$$l = \frac{v_{\text{ion}}/v_{\text{rel}}}{\sigma n} \tag{4.1}$$

where n is the number density of the buffer gas, v_{ion} is the ion velocity and v_{rel} the mean relative velocity between buffer gas and ion [37]. σ is the cross section of the collision of ion and buffer gas, here $^{24}\text{Mg}^{+}$ and ^{4}He. In the hard-sphere model, it can be calculated as

$$\sigma_{Mg-He} \approx \pi(r_{Mg} + r_{He})^2 \approx 3.08 \cdot 10^{-19}\text{m}^2 \tag{4.2}$$

with r_{Mg} and r_{He} the Van-der-Waals radii of the particles [25].

Usually, electrode geometries are defined in text files in a SIMION-specific language using geometric primitives and employing symmetry planes to define a 3D geometry. To achieve a true-to-nature geometry of the Paul trap in SIMION in accordance with the drawings that are used to manufacture the Paul trap, a python tool was written as part of this work. It uses dxf-files of the geometrical cross-section of a multi-electrode model as an input. The dxf-files can be exported from the 3D CAD software Autodesk Inventor. The script transforms it into a file written in the SIMION-native geometry definition language [1]. In contrast to the CAD import supplied by SIMION, this tool employs symmetry planes to define the geometry, which significantly decreases the computational requirements for calculating the electric field and the ion trajectories. The tool was expanded to define 3D geometries from two 2D drawings and to define geometries, which are not completely symmetric. An example for this are the DC electrodes of the Paul trap with their four wedges, which break the cylindrical symmetry, see Figure 3.4.

4.2 Injection simulations

Two methods of injection have to be studied: the online injection from ISOLDE and the reverse injection from an offline ion source providing a beam of stable ions. Availability of stable ions is important for two reasons. First, it is needed for

[1] The code for this tool including examples is accessible at https://gitlab.cern.ch/MIRACLS/dxf-to-gem-file-converter

development work for the MIRACLS setup, which can be effectively done with ions of stable nuclides. Second, the stable ions serve for reference measurements. These are interleaved with online measurements to monitor the system stability and to measure isotope shifts to stable ions with known nuclear charge radii.

The online injection from ISOLDE was studied by Simon Lechner in the design phase of the trap [35]. At this point in time, a slightly different design was pursued: The trap consisted of two regions separated by a plate. A high-pressure region on the injection side to achieve a high stopping power, especially for heavy masses, and a lower pressure region to eject the ions with less disturbance through ion-gas collisions. Furthermore, one more DC electrode was included in the design. The trap was planned to be operated cryogenically at a temperature of $40\,\mathrm{K}$. Simulations were performed at $40\,\mathrm{K}$ and $300\,\mathrm{K}$ for comparison.

For the present work, the design of the trap was changed in favor of a more compact trap design operating at room temperature. Although a cryogenic trap would provide improved beam emittance, the present trap design is capable to meet the MIRACLS requirement for light masses at a reduced system complexity. Nevertheless, the injection simulations of ISOLDE beam in [35] are assumed to hold validity, as the injection region remained unchanged. In these injection simulations, a $40\,\mathrm{keV}$ ion beam with a transverse emittance of $\epsilon_{rms,\mathrm{trans}} = 5\pi\,\mathrm{mm\,mrad}$ and energy spread of $1\,\mathrm{eV}$ was used. An injection efficiency of $\approx 70\%$ was achieved for $^{20}\mathrm{Mg}^{+}$ with a buffer gas pressure of $10^{-2}\,\mathrm{mbar}$ [35].

The present studies are focused on the ion injection from the offline ion source. The simulated beamline for the offline injection can be seen in Figure 4.1. Ions are emitted from the ion source floated to $2\,\mathrm{kV}$. The beam is accelerated to the 'ground' (common floating) potential of the HV plattform, on which the shown beamline is located. The beam is focussed by an einzel lens and passes through a collimator. The latter removes ions far from the center of the beam. The beam is directed onto the axis of the Paul trap by an electrostatic quadrupole bender. A set of two einzel lenses is used to focus the beam into the grounding tube reaching through the insulator that separates the higher potential of the Paul trap chamber from the potential of the beamline. This tube is grounded and keeps the ions in a well-defined potential compared to the insulator. Additionally, the tube acts as a differential pumping section between the elevated pressure in the Paul trap cross and the downstream beamline. Therefore the tube features an aperture of $10\,\mathrm{mm}$ diameter at the side facing the Paul trap. From this grounding tube, the ions are injected into the Paul trap, which is floated to a potential approximately corresponding to the ion beam energy. The injection is facilitated through the injection cone located in front of the endcap of the Paul trap. In this simulation, an ion is counted as injected when it passes through the entrance hole ($5\,\mathrm{mm}$) of the endcap of the Paul trap, which presents the smallest aperture in the Paul trap.

The ion source planned to be used first for the reverse injection is a magnesium electron impact ionization ion source, see Figure 4.2. Solid magnesium is vaporized in an resistively heated oven. Atomic Mg vapor is ionized by the impact of electrons. These electrons are emitted from a heated filament and accelerated towards the ionization region surrounded by the filament, which is shaped into a ring. The ion emission characteristics of this ion source were studied by simulations in [38]. It can

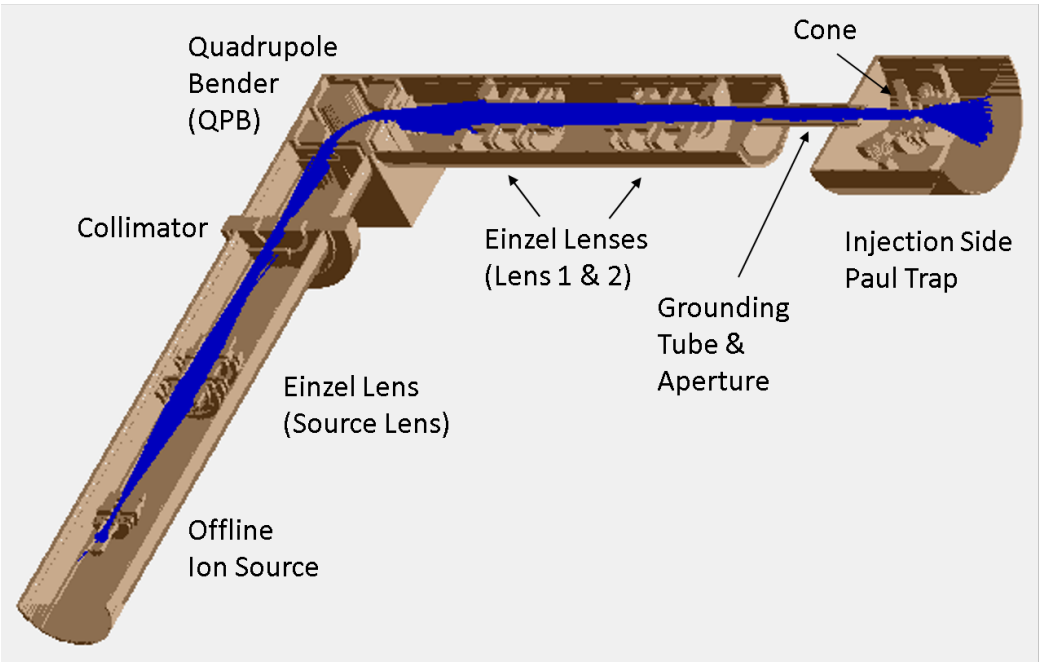

Fig. 4.1: Simulated beamline for the injection of the beam provided by the offline ion source into the Paul trap. The ions are produced in the offline ion source. After acceleration to $2\,\mathrm{keV}$, the ions are focused by an einzel lens (Source Lens), passing through a collimator, and the beam is deflected by an electrostatic quadrupole bender (QPB). The ions are focused by a combination of two einzel lenses (Lens 1 and 2) into a tube with an aperture connecting the beamline and the Paul trap chamber. Finally, the ions are entering the Paul trap. At this simulation step, the Paul trap is only partially modeled and no RF potentials are applied. No buffer gas is considered.

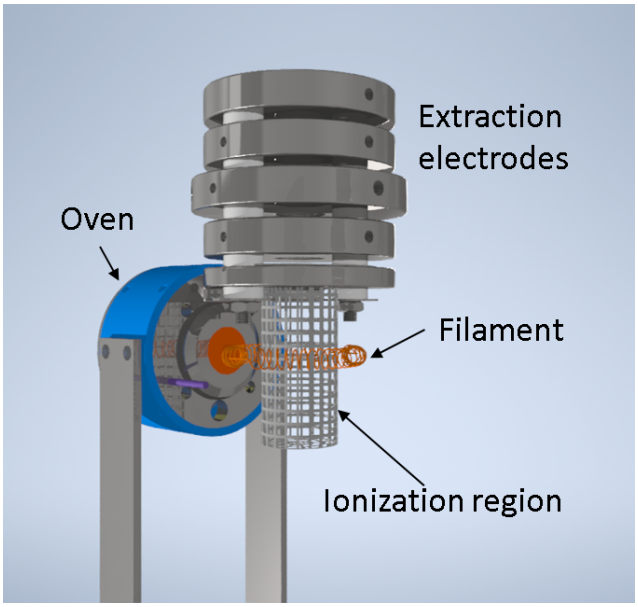

Fig. 4.2: 3D CAD model of parts of the magnesium electron impact ionization ion source.

Tab. 4.1: Optimal potentials for reverse injection from the offline ion source into the Paul trap. Next to the optimal potentials the decrease in the number of injected ions for a variation of the potential of 5% is listed as a measure of the sensitivity of this potential. Furthermore the share of ions lost at each element is displayed (Rel. ion loss (%)). The beamline is shown in Figure 4.1. The elements are listed in the order from the source to the trap.

Element	Potential (V)	+5% V (%)	-5% V (%)	Rel. ion loss (%)
Source Lens	-2675	3.2	6.9	2.4
Collimator	-	-	-	6.8
QPB	1310	10.7	10.3	1.2
Lens 1	-1740	1.4	0.6	7.8
Lens 2	-1340	1.6	0.3	0
Tube	-	-	-	3.5
Cone	1770	0.3	0.4	2.8

be assumed that the ion distribution is homogenous in radial direction inside the ionization region defined by a cylindrical mesh, which has a diameter of $6.8\,\mathrm{mm}$. In the beam direction it is assumed that the ion distribution is homogenous in the region surrounded by the filament, which has a height of $4.6\,\mathrm{mm}$. The filament should be positioned at 50% of the ionization region length to yield the ideal compromise of small energy spread within the extracted beam and a high number of extracted ions [38]. The ions generated in this cylindrical region are assumed to have a mean initial kinetic energy of $E_{\text{kin}} = {}^{3}\!/_{2} k_B T = 50\,\mathrm{meV}$ (with T the vaporization temperature of Magnesium, which is $\approx 450\,\mathrm{K}$ at $10^{-7}\,\mathrm{mbar}$). The energy distribution is assumed to be gaussian with an FWHM of $0.024\,\mathrm{eV}$, calculated from the variance of the Maxwell-Boltzmann probability density function. The used source parameters resulted in a simulated beam energy of $1998.8\,\mathrm{eV}$ with an FWHM of $5.6\,\mathrm{eV}$. This energy spread is dominated by the static potential along the ionization region.

The geometry shown in Figure 4.1 is imported from the Inventor model via the dxf conversion tool and the electric fields are calculated with a resolution of $0.5\,\mathrm{mm}$ per grid unit. The optimal potentials for maximal injection into the Paul trap are found by employing a Simplex optimization algorithm [39]. The resulting beamline element potentials can be found in table 4.1, together with the relative ion losses at the respective element. An injection efficiency of 77.8% from the ion source through the endcap of the Paul trap is achieved in this simulation. The largest ion losses are due to Lens 1, where 7.8% of the ions hit an einzel lens electrode. To investigate the sensitivity of the ion transmission on voltage drifts or fluctuations, the potential of each beamline element is changed by $\pm 5\%$ and the respective ion loss recorded. This study shows that the quadrupole bender (QPB) is most sensitive to voltage changes, i.e. the number of injected ions decreases by 10% for a voltage change of 5%. However this corresponds to a change in potential of $65.5\,\mathrm{V}$, which is far larger than the supplied voltage stability of typical power supplies. Thus, it is demonstrated that voltage source fluctuations or drifts should have a rather minimal effect on the experimental injection efficiency.

4.3 Trapping efficiency simulations

Following the injection into the trap, the trapping of the ions is simulated. The trapping is dependent on the longitudinal trapping potential provided by the DC segments, on the radial potential provided by the RF electrodes, and also the properties of the buffer gas. In continuous injection mode the ions have to be decelerated in collisions with buffer gas.

The simulated geometry can be seen in Figure 4.3 and the longitudinal trapping potential along the trap axis is shown in Figure 4.4. The ions are started in the center of the tube reaching into the chamber with the Paul trap. The spatial distribution, as well as energy and time distribution, of the ion beam, were determined from the previous injection simulation, see section 4.2. The buffer gas is assumed to be only inside the trap itself, confined by the DC electrodes and the endcaps. The buffer gas escaping the trap through the apertures of the endcaps is neglected, i.e. outside of the trap perfect vacuum is assumed.

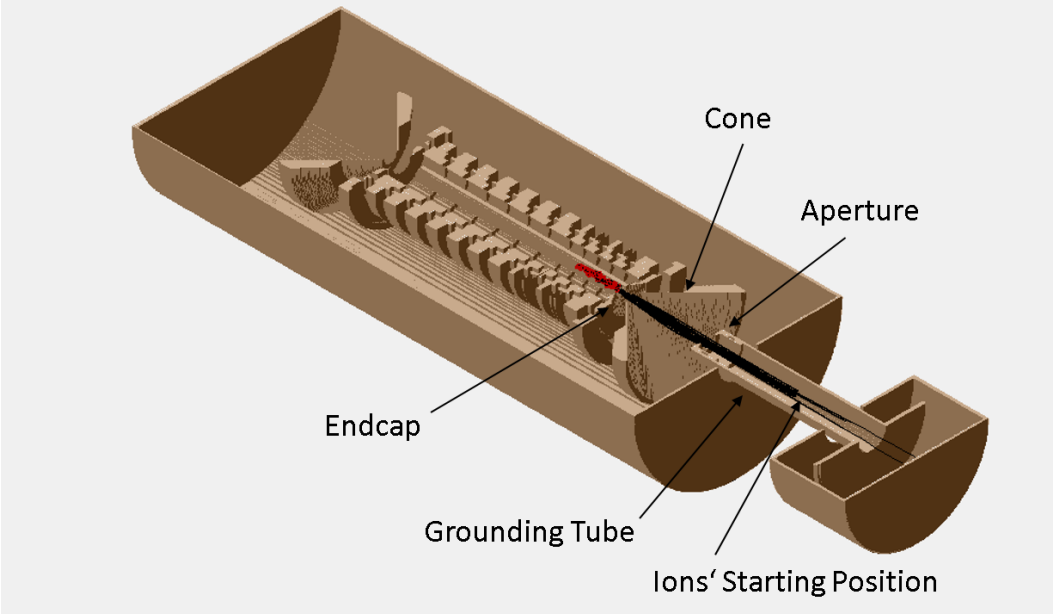

Fig. 4.3: Simulation geometry for trapping efficiency simulations. Ion trajectories are shown in black, red dots mark positions of collisions of ions and buffer gas atoms.

An ion is considered trapped, when it performs more than one full turn, i.e. at least three turnarounds, in the longitudinal direction in the trap. A higher number (50) of minimal turnarounds has also been tested as a trapping criterion, but no difference in the resulting trapping efficiency between the two criteria outside the uncertainty of the simulations is found. Therefore, the trapping criterion of three turnarounds is chosen for a shorter computation time. The trapping efficiency is defined as the share of the injected ions that are trapped, $\epsilon_{\text{trap}} = N_{\text{trapped}}/N_{\text{injected}}$.

In Figure 4.5, the trapping efficiency, together with the injection efficiency and the percentage of ions that are both injected and trapped, is shown as a function of the buffer-gas pressure. At low buffer-gas pressure, the probability of an ion-atom collision is too low to decelerate the ions efficiently. For instance, ions may also

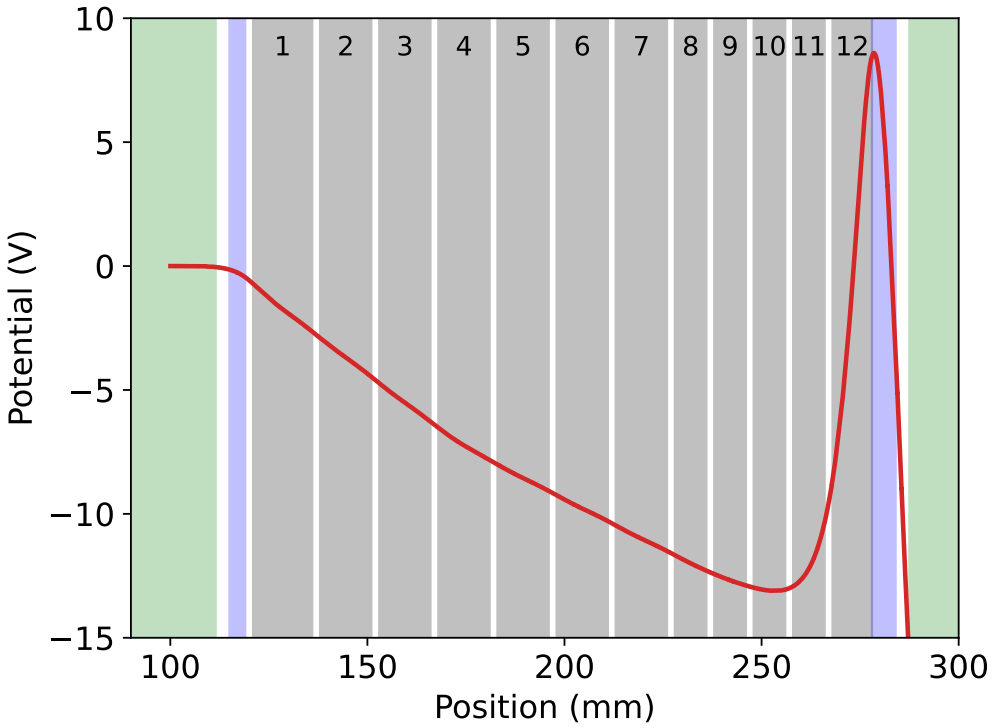

Fig. 4.4: Potential along the axis of the trap extracted from the simulation. The colored background indicate the positions of the DC electrodes (silver), the endcaps (blue) and the cones (green).

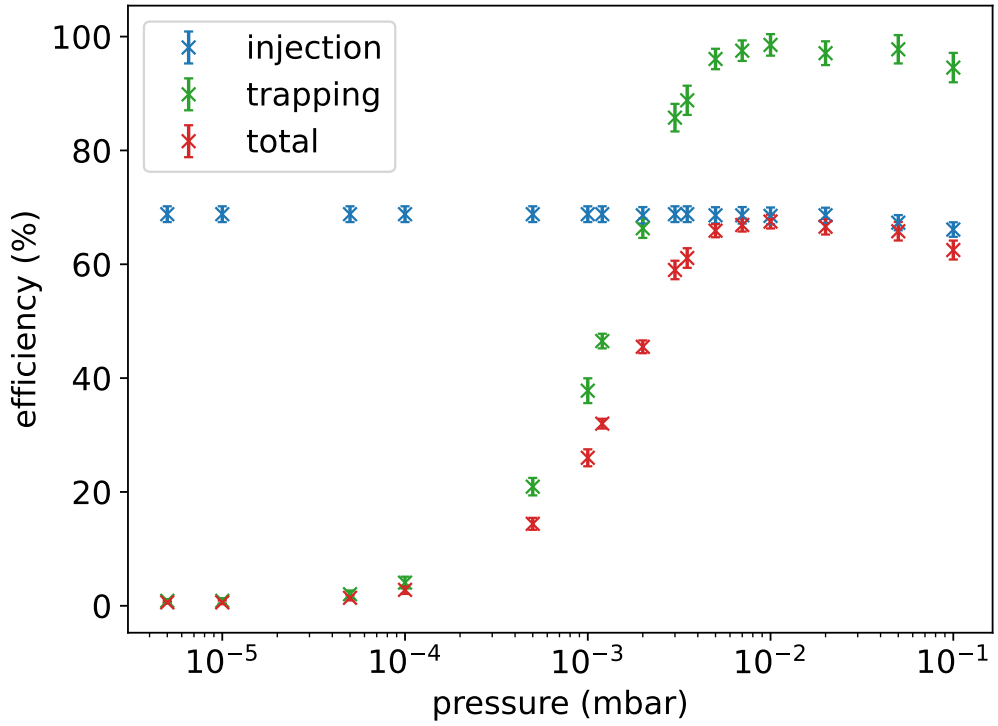

Fig. 4.5: Percentage of the ions that are injected into and trapped in the trap as a function of the buffer gas pressure in the trap. The total efficiency describes ions that are injected and trapped. Simulations are performed for $^{24}Mg^{+}$ ions, with an additional floating bias of $0\,\mathrm{V}$ on top of the chosen floating potential of $2002\,\mathrm{V}$. The RF amplitude is $240\,\mathrm{V}$ and the RF frequency is $1.2\,\mathrm{MHz}$. The used longitudinal potential is shown in Figure 4.4.

pass over the potential of the second endcap and are consequently lost. If a high potential is applied to the endcap opposite to the injection side, the ions are reflected once and leave the trap through the injection side again. After a steep increase of trapping efficiency with increasing pressure, the trapping efficiency saturates around $10^{-2}\,\mathrm{mbar}$. At even higher pressures, the trapping efficiency is decreasing slightly. This is due to more frequent collisions in the front region of the trap, which push the ions radially onto the surface of DC and RF electrodes. Moreover, the injection efficiency is decreasing as the mean-free-path of the ions is decreasing and more collisions are happening directly at the aperture of the endcap, hindering the ions from entering the trap.

The floating potential of the Paul trap is a second important parameter for the trapping and injection efficiency, see Figure 4.6. The standard floating potential of the Paul trap is $2002\,\mathrm{V}$, slightly higher than the mean beam energy. When the potential is increased, fewer ions can enter the trap, as their kinetic energy is not sufficient to overcome the potential at the injection endcap and consequently the ions are reflected. The ions, that are injected into the trap, have lower kinetic energy than in the standard scenario, therefore the trapping efficiency is increased. Towards lower floating potentials, the injection efficiency is constantly high, but the trapping efficiency is decreasing, as the ions are more energetic in the trap. At high pressures,

this decrease is rather slow, as the stopping power of the gas is high, see Figure 4.6a. For lower pressures, see Figure 4.6b, the trapping efficiency is vastly decreased and shows a narrow optimum. Also, the floating potential for the highest total efficiency is different for the two different buffer-gas pressure values.

In a next step, the influence of the radial trapping potential is considered. The potential depends on the amplitude of the applied RF signal and the stability parameter q, which depends on the amplitude and frequency of the RF signal. The q value for $^{24}\mathrm{Mg}^{+}$ ions in the present Paul trap is mapped in Figure 4.7 as a function of RF amplitude and frequency of the square wave. All previously discussed simulations (4.5,4.6) have been performed with an RF amplitude of $240\,\mathrm{V}$ and RF frequency of $1.2\,\mathrm{MHz}$, which results in $q \approx 0.4$. Above $q = 0.712$, the ion motion is unstable (see section 3.2). This is indicated as the white area on the top-left in Figure 4.7.

The simulated trapping efficiency of ions injected into the trap as a function of RF amplitude and frequency is presented in Figure 4.8. There the red lines indicate the theoretical limits on the trapping efficiency. The upper limit is induced by reaching the stability parameter $q = 0.712$, hence the ion trajectories are no longer stable and ions can not be trapped. The lower limit is the minimum radial trap depth required for trapping: Below this limit, no ions can be trapped, as the kinetic energy of the ions is larger than the RF trapping potential. To determine this limit, the minimal kinetic energy of an ion entering the trap has to be known. As the energy can be transferred between the directions of motions, the complete energy of the injected ions has to be considered and not only the radial component. The injection was simulated ten times, the energy of the ion with the lowest energy entering the trap recorded and averaged over the ten simulations. From this value $E_{\mathrm{kin,min}}$, the minimal RF amplitude $V_{0,\mathrm{min}}$ to trap at least one ion was calculated (using equation 3.18) by

$$V_{0,\mathrm{min}} = \sqrt{\frac{E_{\mathrm{kin,min}}}{e\alpha}\frac{mr_0^2}{2e}}\Omega \tag{4.3}$$

with α the correction factor for the digital trap potential.

Finally, the trapping efficiency as a function of the stability parameter q for different RF amplitudes is studied, see Figure 4.9. In all cases, the trapping efficiency is dropping to 0 when approaching $q = 0.712$, where the stability of the trajectories is lost. For stability parameters between 0.3 and 0.6, the highest trapping efficiencies are reached. Generally, higher RF amplitudes result in higher trapping efficiencies. Increasing the RF amplitude of the square-wave drive from $100\,\mathrm{V}$ to $200\,\mathrm{V}$ doubles the trapping efficiency for $q \approx 0.4$. However, when increasing the RF amplitude further, the improvement in efficiency is smaller until it saturates around $400\,\mathrm{V}$. Utilizing large RF amplitudes can present a serious sparking risk due to the small distances in the trap. Thus, a careful compromise has to be found for the operation of the Paul trap.

In summary, it can be concluded that the highest trapping efficiency is achieved for a pressure of $10^{-2}\,\mathrm{mbar}$, a floating potential of the Paul trap slightly lower than the

(a)

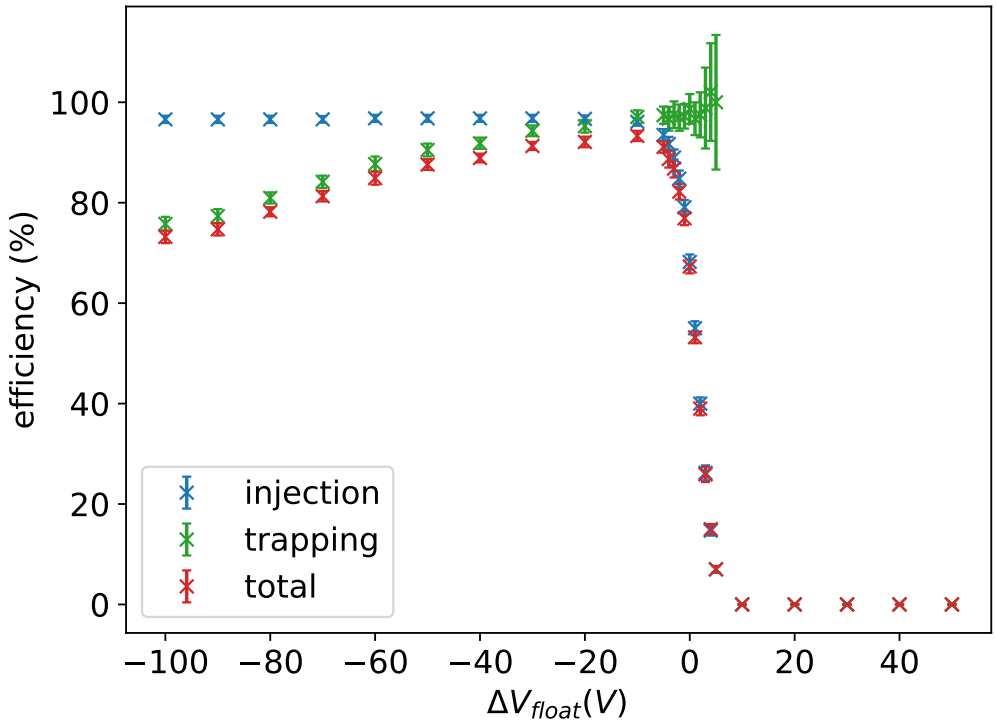

(b)

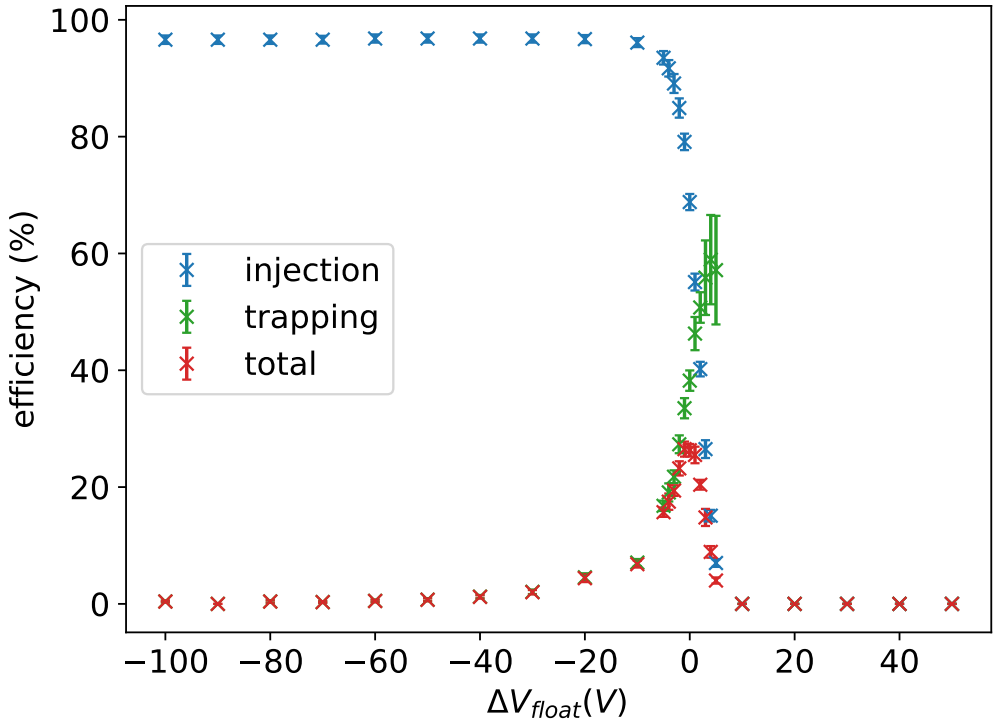

Fig. 4.6: Injection and trapping efficiency as a function of the difference of the floating potential to the standard floating potential of the Paul trap of $2002\,\mathrm{V}$ for two different pressure conditions, $10^{-2}\,\mathrm{mbar}$ (top) and $10^{-3}\,\mathrm{mbar}$ (bottom). Simulations are performed for $^{24}\mathrm{Mg}^{+}$ ions with an RF amplitude of $240\,\mathrm{V}$ and $1.2\,\mathrm{MHz}$ RF frequency. The used longitudinal potential is shown in Figure 4.4.

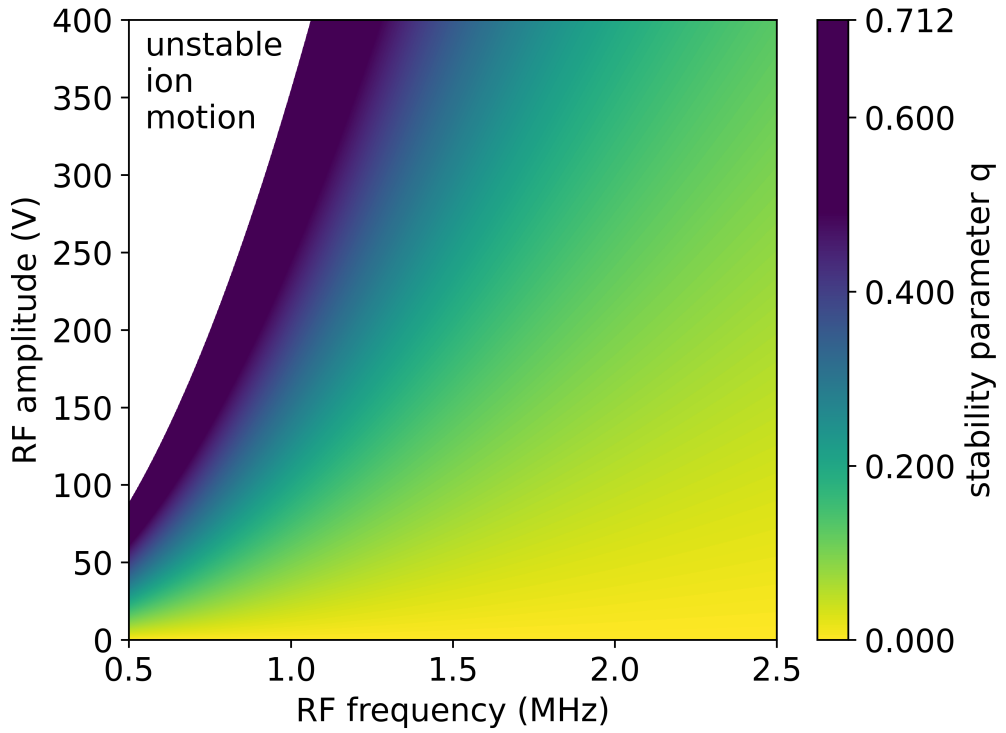

Fig. 4.7: Stability parameter q as dependent on the RF amplitude and frequency for $^{24}\mathrm{Mg}^{+}$. At $q = 0.712$ the stability of the ion motion is lost.

beam energy, and a q parameter between 0.3 and 0.6 with RF amplitudes as high as $300\,\mathrm{V}$. With this combination, a trapping efficiency of 97% is achieved in the simulation.

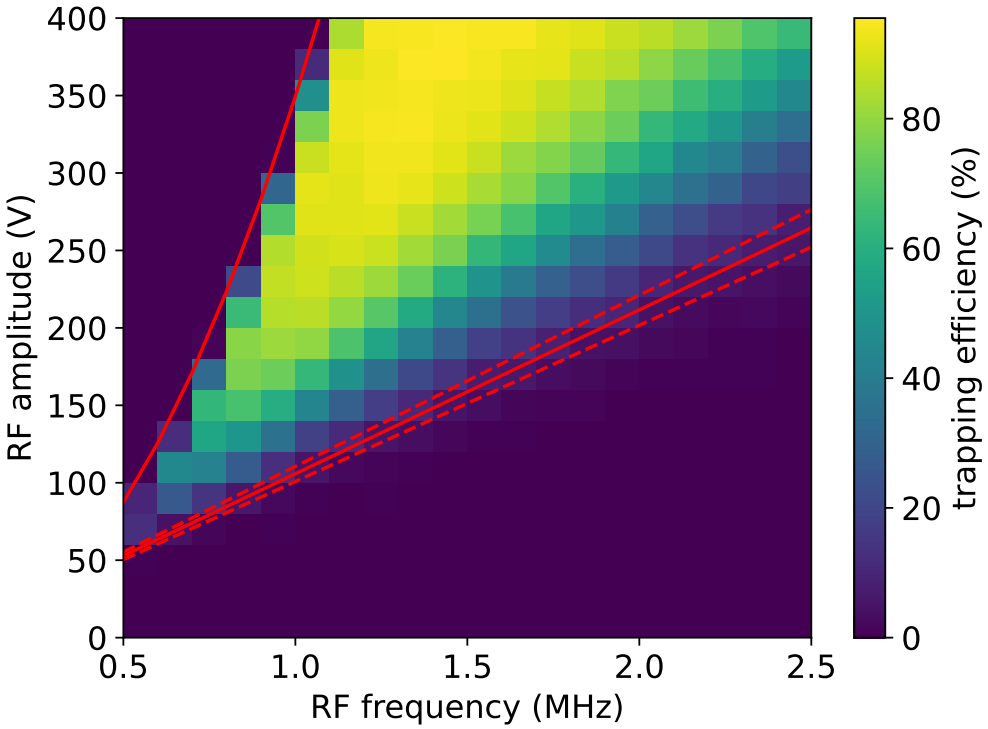

Fig. 4.8: Simulated trapping efficiency as dependent on RF amplitude and frequency. Simulations are performed for $^{24}\mathrm{Mg}^{+}$ ions injected into the Paul trap. In this simulation, the floating potential of the Paul trap is set $22\,\mathrm{V}$ below the standard floating potential of $2002\,\mathrm{V}$ and a helium gas pressure of $10^{-2}\,\mathrm{mbar}$ is assumed. The used longitudinal potential is shown in figure 4.4. In red, theoretical limits on the trapping, are drawn. The upper limit consists of reaching the stability condition $q = 0.712$, the lower limit is imposed by the minimal trap depth calculated from the minimal ion energy using equation 4.3. The error due to the uncertainty of this value is shown in dashed red lines.

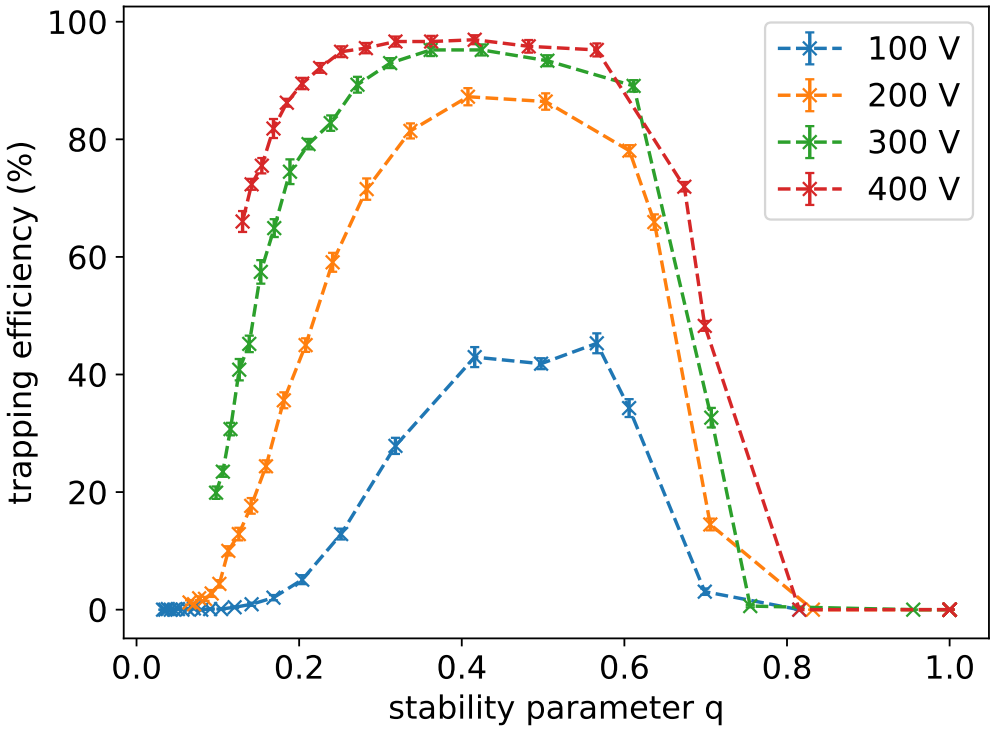

Fig. 4.9: Simulated trapping efficiency as a function of the stability parameter q for different RF amplitudes. Simulations are performed for $^{24}\mathrm{Mg}^{+}$ ions injected into the Paul trap. In this simulation, the floating potential of the Paul trap is set $22\,\mathrm{V}$ below the standard floating potential and a helium gas pressure of $10^{-2}\,\mathrm{mbar}$ is assumed.

4.4 Cooling simulations

As discussed in the previous section, cooling of the ions is important for a successful injection of a continuous beam into the trap. Moreover, a cold ion ensemble results in a small emittance of extracted ion bunches, which is crucial for the operation of the Paul trap as a cooler. The final temperature of the ions and the cooling time, i.e. the time to reach the equilibrium temperature, is studied for a variable buffer-gas pressure in the trap.

Figure 4.10 illustrates the cooling process when injecting ions into the trap. The ion performs several oscillations with decreasing amplitude and energy during the cooling process. Collisions with buffer-gas atoms decrease the total energy of the ion. In thermal equilibrium at the end of the trajectory, heating and cooling collisions have the same probability.

For the following simulations, the simulation geometry is identical to the previous chapter, see Figure 4.3: The ions are released in the grounding tube and injected into the trap. During the simulation of the ion-motion, the trajectory parameters, such as kinetic energy, are sampled in equal time intervals.

In Figure 4.11 the contribution of the ion motion in each direction to the total kinetic energy of an ion bunch is shown over time. A rolling average larger than the oscillation frequencies of the ion motion has been applied to this data and the energy contribution was averaged over 1000 ions. An exponential decrease over time is seen for both radial and axial direction over time. The final ion temperature in the radial direction is significantly higher than in the longitudinal direction as expected due to the RF reheating in radial direction, see section 3.3.

In Figure 4.12, the cooling half time $\tau_{1/2}$ versus buffer-gas pressure is shown. The half time is extracted from the exponential fit

$$E_{\text{kin}}(t) = E_0 e^{-\ln 2 \frac{t}{\tau_{1/2}}} \tag{4.4}$$

to data, see for instance Figure 4.11 for data and fit at $10^{-3}\,\text{mbar}$. As expected, lower pressure results in a longer cooling period, since the time between collisions is longer, because of the longer mean free path of the ions in gas, described in equation 4.1. The cooling time is different for radial and longitudinal motion, as the trajectory components have different velocities, leading to a different time between collisions, see equation 4.1. It can be assumed, that the number of collisions required to reach thermal equilibrium is constant [25]. For higher velocity, this number of collisions is reached faster. Initially, the velocity in the beam direction is much higher than in the radial direction, therefore the cooling half time is larger in the radial direction. Furthermore, the cooling process is counteracted by the RF reheating in radial direction. The expected $1/p$ dependence (from equation 4.1 with n proportional to p) in Figure 4.12 is fitted to the simulated data in radial and longitudinal direction.

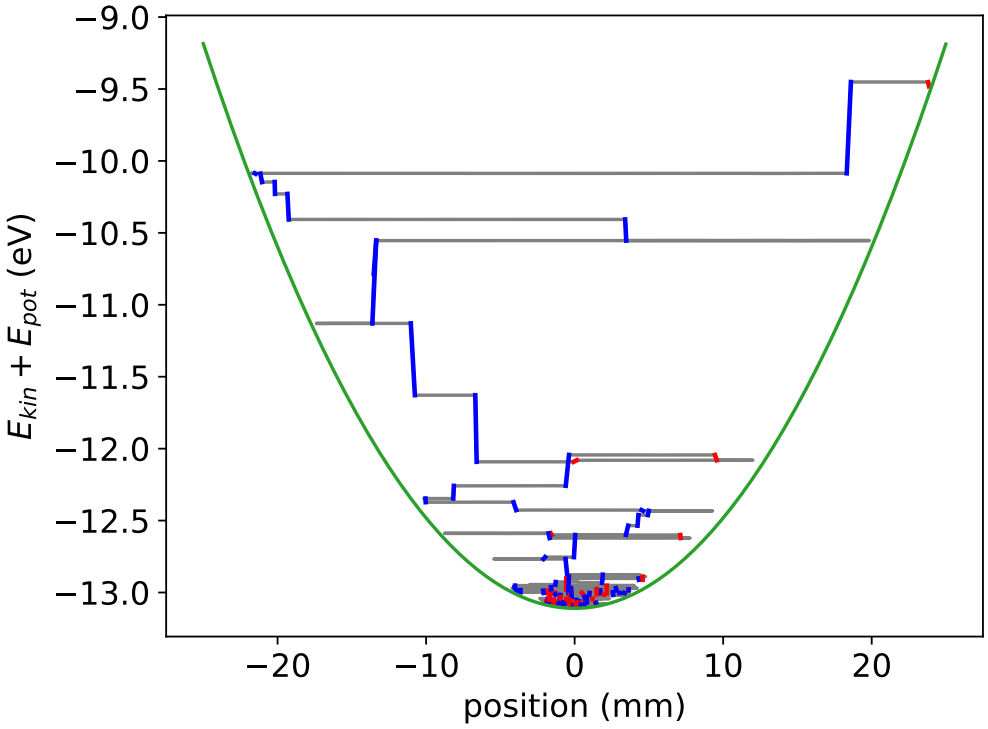

Fig. 4.10: Simulated trajectory (grey) of an $^{24}Mg^{+}$ ion during cooling in the longitudinal potential (green). Vertical colored lines, indicate a collision with buffer gas, which leads to a change in energy. Blue lines indicate an effective cooling through the collision, red lines indicate heating. The simulation was performed in the static effective potential well according to equation 3.11 [2]. The buffer gas pressure is 10^{-2} mbar.

[2] When performing the simulation with a potential generated through an RF squarewave potential, the energy fluctuates between subsequent collisions. For clarity, the static potential was used for this plot, but the overall behavior between the shown and the more realistic scenario remains the same.

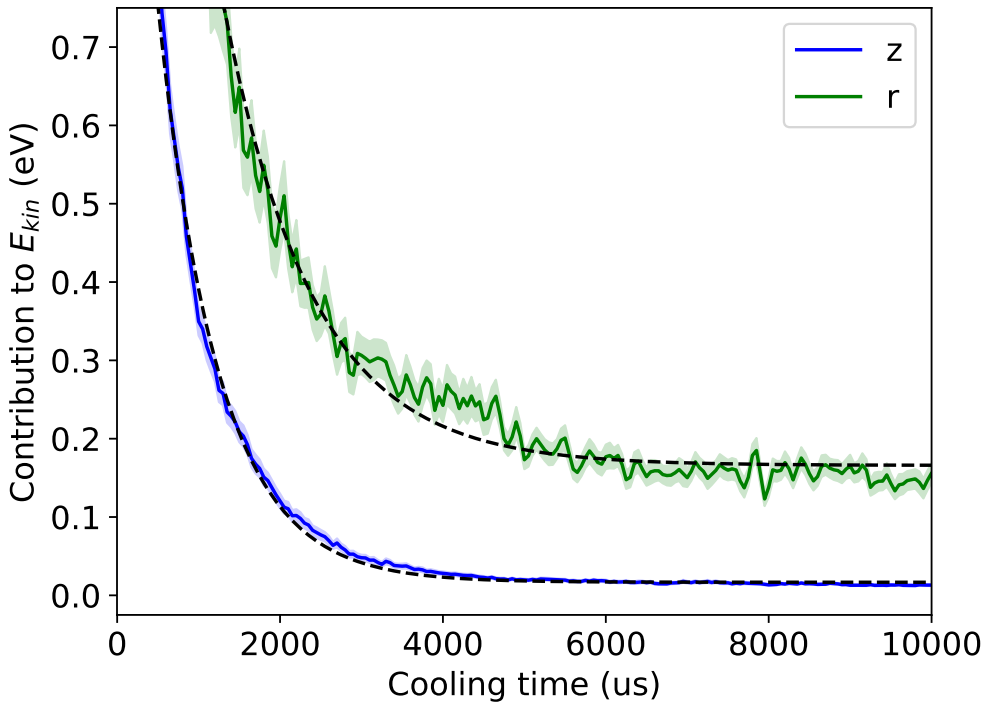

Fig. 4.11: Mean and standard deviation of the kinetic-energy contribution due to radial (r) and longitudinal (z) motion are plotted over time as solid lines and shaded bands, respectively. Exponential fits to the data are shown in dashed lines. The data is based on the trajectories of 1000 ions. Exclusively ions, which survived until the end of the simulation are taken into account for the averaged energy. The simulations are performed for $^{24}\mathrm{Mg}^{+}$ ions at $10^{-3}\,\mathrm{mbar}$ and a buffer gas temperature of $300\,\mathrm{K}$. The RF potential is created by an RF amplitude of $240\,\mathrm{V}$ and an RF frequency of $1.2\,\mathrm{MHz}$. The used longitudinal potential is shown in Figure 4.4.

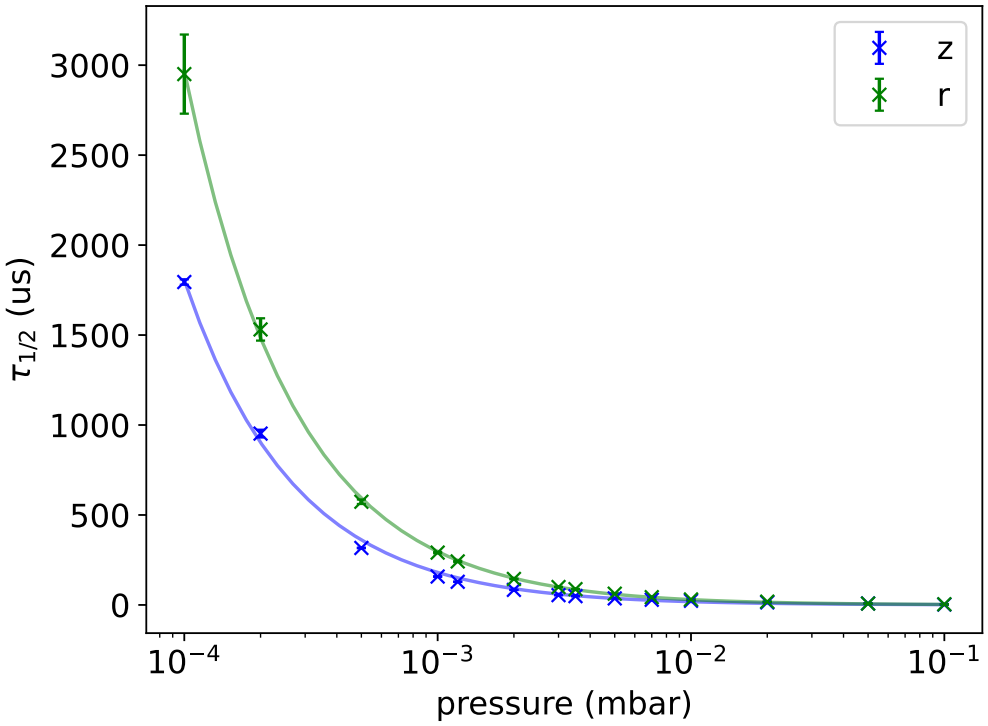

Fig. 4.12: Cooling halftime $\tau_{1/2}$ at different buffer-gas pressures is displayed for radial (r) and axial (z) direction. $^1/_p$ fits to the data are shown as solid lines. The simulations are performed for $^{24}Mg^+$ ions and a buffer gas temperature of $300\,K$. The RF potential is created by an RF amplitude of $240\,V$ and an RF frequency of $1.2\,MHz$. The used longitudinal potential is shown in Figure 4.4.

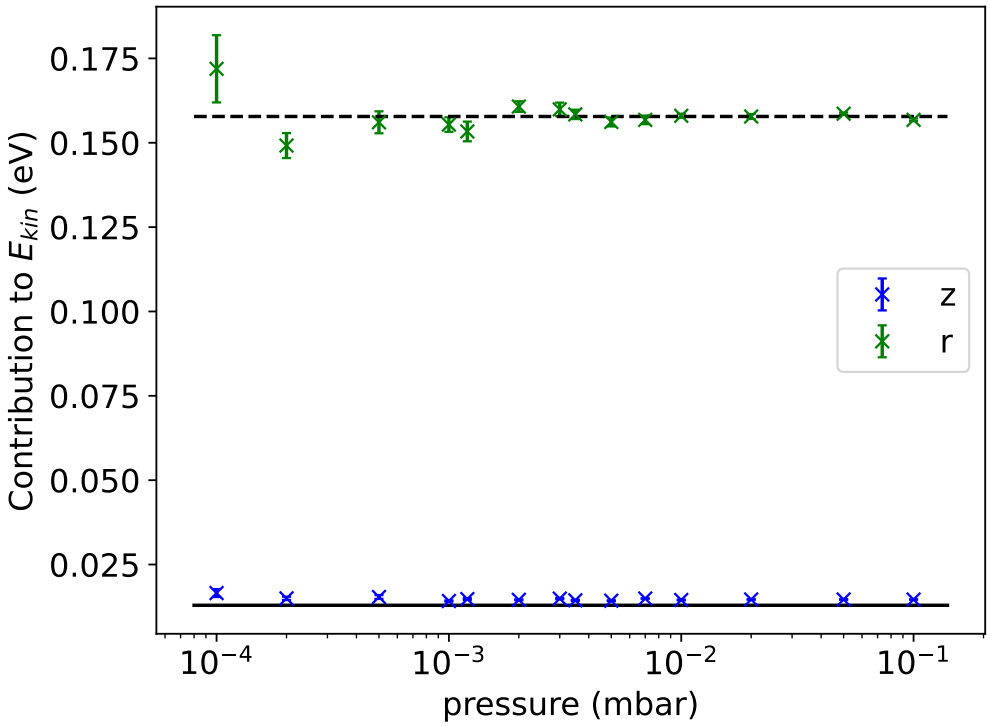

Fig. 4.13: Contribution to the final energy in thermal equilibrium at different buffer gas pressures by the motion in radial (r) and axial (z) direction. The solid black line shows the energy expected energy at $300\,\mathrm{K}$, according to $E = {}^1/_2 k_B T$, the dashed line shows the average of the final energies determined in radial direction. The simulations were performed for $^{24}\mathrm{Mg}^+$ ions and a buffer gas temperature of $300\,\mathrm{K}$. The RF potential is created by an RF amplitude of $240\,\mathrm{V}$ and an RF frequency of $1.2\,\mathrm{MHz}$. The used longitudinal potential is shown in Figure 4.4.

Among the first science cases at MIRACLS is $^{34}\mathrm{Mg}$ with a half-life of $20\,\mathrm{ms}$ [40]. The present simulations indicate that the expected cooling times in the Paul trap are much shorter and hence compatible with short-lived radionuclides in this mass region.

In Figure 4.13, the energy of the ions after complete cooling is shown. Thermal equilibrium is expected to be reached after $\approx 5\tau_{1/2}$ [25]. The trajectories of the ions are simulated for at least this time. For the last $500\,\mu\mathrm{s}$ of the trajectory, the kinetic energy is averaged for each direction. As expected, the final energy is independent of the exact pressure. The final energy in the longitudinal direction was determined to be $0.015\,\mathrm{eV}$, which is slightly higher than what one would assume based on $E = {}^1\!/_2 k_B T$ with $T = 300\,\mathrm{K}$. The small increase in temperature could possibly be explained by a fraction of the energy being gained by the RF reheating process, which is propagated to the longitudinal motion, as the motions are coupled in higher-order and through the collisions with buffer gas. In the radial direction, the average energy is $0.158\,\mathrm{eV}$, which corresponds to a temperature of about $1800\,\mathrm{K}$, according to $E = k_B T$, for the 2-dimensional motion. For the temperature in the radial direction, no theoretical prediction could be made for the square-wave potential.

4.5 Ion trajectories

The trajectory of a trapped ion is simulated for comparison to theoretical expectations. In the simulated geometry as used before, one single ion is randomly selected from the usually studied ion bunch and its simulated trajectory is investigated. For the longitudinal motion component, see Figure 4.14a, the initial cooling process is well visible. Over the first few oscillations, the motion amplitude decreases significantly due to the energy loss in collisions with the buffer gas, of which individual collision events are indicated as red dots. Generally, the amplitude of the motion is governed by the initial conditions. However, the motion is frequently disturbed by buffer-gas collisions, which cause exchange of energy between the directions of motions. Thus, the amplitude of the longitudinal motion after the cooling is not fixed.

For the radial motion, see Figure 4.14b, the macromotion is visible as the main motion. The micromotion is modulated onto this motion with a higher frequency. Due to transfer of energy between the longitudinal and radial oscillation in collisions, the amplitude of the macromotion varies.

The sudden phase jumps and changing amplitudes following the collision events do not allow to fit the expected theoretical functions to the motion components. Instead, the frequencies of the reorded ion motions are analyzed using a Fourier transform. The results are shown in Figure 4.15. At the top of the Figure, the longitudinal frequency spectrum is shown along with the theoretical prediction for the central frequency, according to equation 3.10. This frequency is governed by the shape of the longitudinal potential. For low ion energies and axial amplitudes, the lowest

(a)

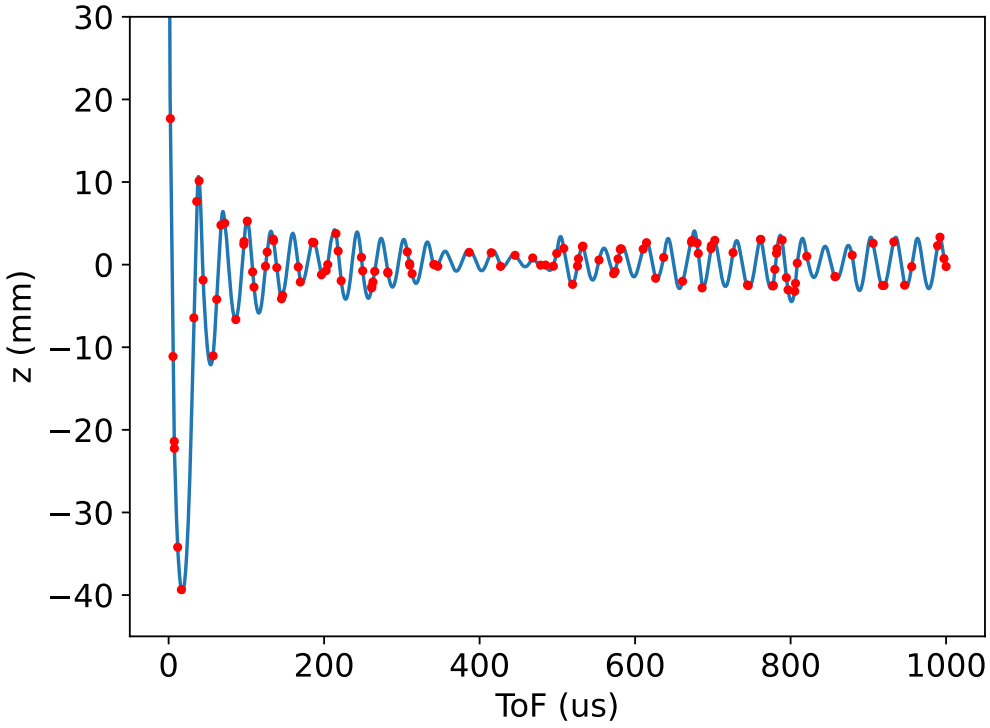

(b)

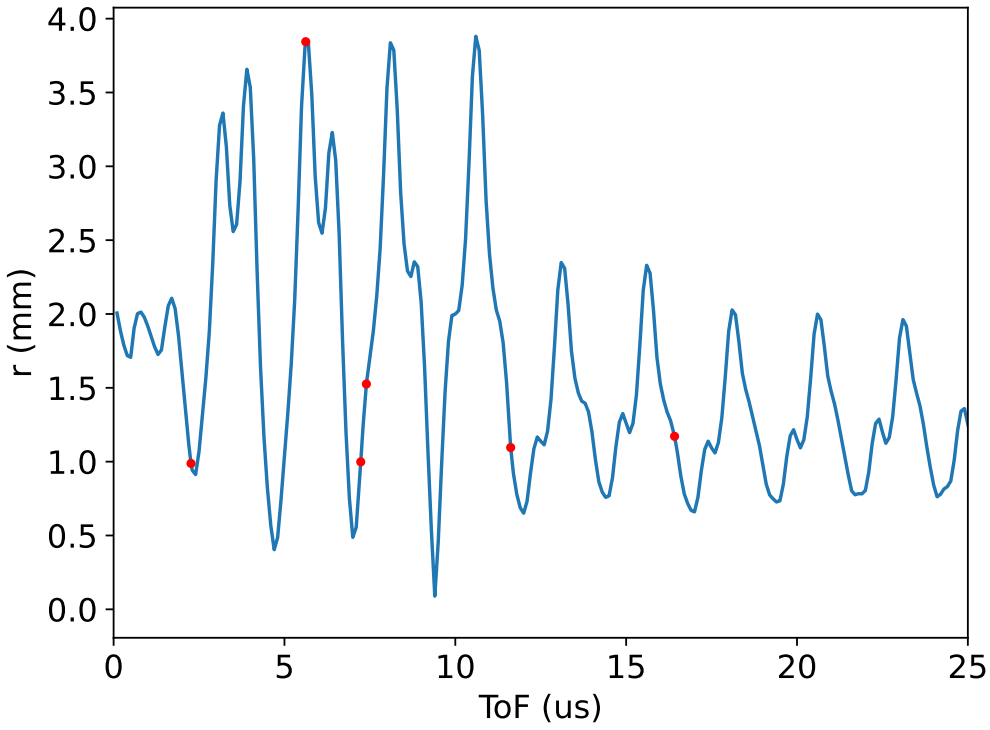

Fig. 4.14: Trajectory of one $^{24}Mg^{+}$ ion being injected into the trap. The top plot shows the longitudinal coordinate of an ion over time and the bottom plot the radial coordinate. Note the different time scale because of the largely different oscillation frequencies. Red dots indicate collision events with buffer gas. The trajectory is simulated at a buffer gas pressure of 10^{-2} mbar. The RF potential is created by an RF amplitude of 240 V and an RF frequency of 1.2 MHz. The used longitudinal potential is shown in Figure 4.4.

order potential at the trap minimum is parabolic. This was characterized in terms of

$$C_2 = \frac{V_{DC}}{z_0^2} \tag{4.5}$$

which defines the depth and shape of a parabolic potential. The C_2 parameter is determined by extracting the potential along the center of the trap from SIMION and fitting a quadratic function to this potential, see Figure 4.16 for an exemplary potential and fit. In Figure 4.15a in the frequency spectrum of the axial motion, the light red area indicates the uncertainty in frequency stemming from the fit of C_2. Overall a good agreement between theoretical prediction and simulations is found.

In radial direction, the frequency of the macromotion can be directly calculated following equation 3.16. The result is indicated in red, in Figure 4.15b. In orange, double the secular frequency, the second order harmonic, is shown. In purple, the RF driver frequency is indicated, which corresponds to the expected frequency of the micromotion. The micromotion frequency seems to be shifted slightly towards lower frequencies, the reason for this shift is not fully understood. In green, the expected positions of higher-order frequency contributions according to equation 3.15 are shown, but they are not significantly appearing in the frequency spectrum. It can therefore be concluded, that the higher-order contributions are small.

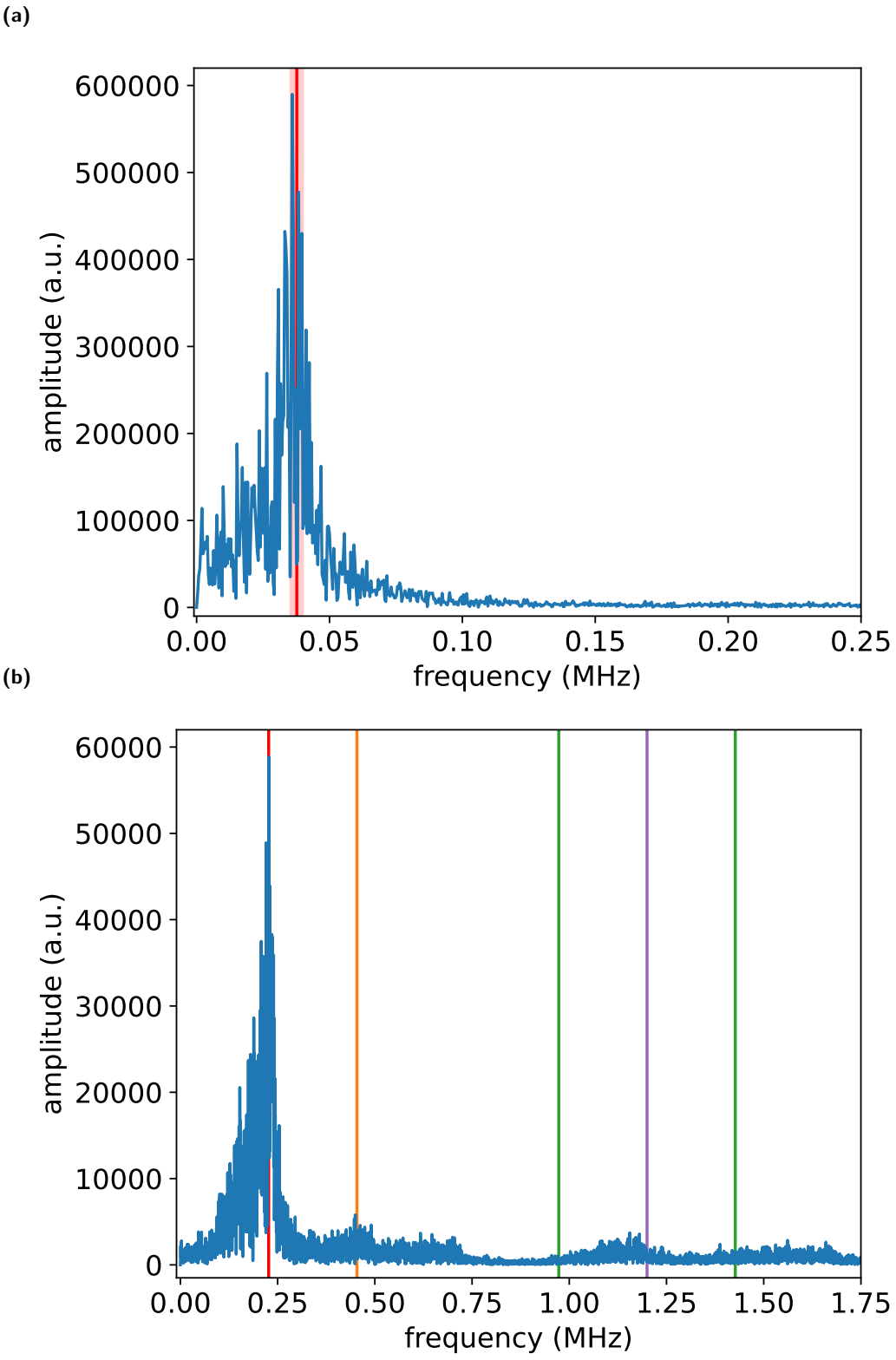

Fig. 4.15: Fourier transformation of the ion trajectory (partially shown in Figure 4.14) in longitudinal (top) and radial (bottom) direction. In red solid lines, the theoretically expected frequency is marked. The red shaded area in the upper plot indicates the uncertainty region stemming from determining the potential parameter C_2. In the lower plot, the second harmonic of the macromotion frequency is marked in orange. Additionally, the micromotion frequency is marked in purple. The green lines indicate the expected position of second-order secular oscillation frequencies. However, the presence of those is not significant. The trajectory is simulated with one $^{24}\mathrm{Mg}^{+}$ ion at a buffer gas pressure of $10^{-2}\,\mathrm{mbar}$. The RF potential was created by an RF amplitude of $240\,\mathrm{V}$ and an RF frequency of $1.2\,\mathrm{MHz}$. The used longitudinal potential is shown in Figure 4.16.

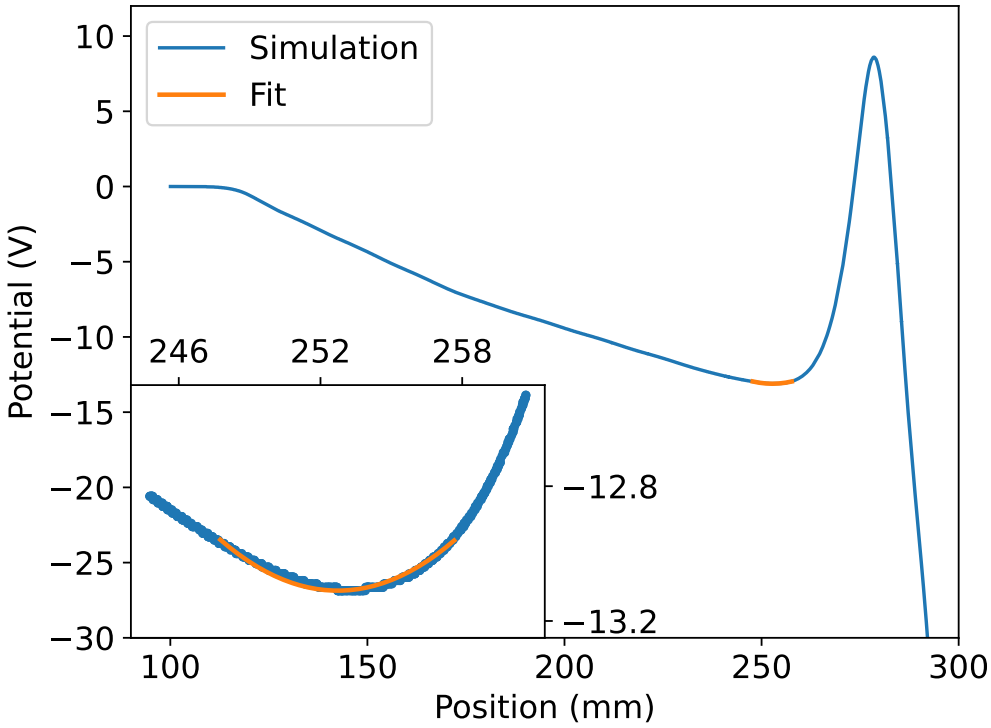

Fig. 4.16: Longitudinal trapping potential extracted from simulations, with a fit $f(z) = U_{\min} + C_2(z - z_0)^2$ around the position of the potential minimum z_0. The insert shows the region $\pm 8\,\mathrm{mm}$ around the potential minimum. This potential is the most shallow potential used in the present work.

4.6 Ion bunching

The cooled ions are extracted from the Paul trap as temporally short ion bunches to be subsequently injected into the MR-ToF ion trap, where the laser spectroscopy measurement will take place. The laser-spectroscopic resolution and sensitivity depends, among others, on the energy, time, and spatial spread of the ion bunch, which can be characterized in terms of longitudinal and radial emittance. Therefore, the obtained emittance for different trapping potentials has been studied in the next simulations.

To reduce complexity and computational time for this simulation, the ions are not injected into the trap but start at the minimum of the trapping potential inside the trap. The initial kinetic energy assigned to them is slightly lower than the expected kinetic energy according to the buffer gas temperature. Subsequently, the ions are simulated in the trap together with buffer gas until thermal equilibrium is reached. It has been verified separately that the ion distributions after injection and cooling are identical to the ion distributions when the ion motion starts in the trap and the motions are thermalized in buffer-gas collisions. After the thermalization, the ions are extracted from the trap into the grounding tube. This geometry is identical to the one used in the previous simulations, see Figure 4.3. For extracting the ions, the potentials downstream of the potential minimum are lowered. The same extraction potential is used for all emittance simulations. A steep extraction potential is chosen to be able to also extract ions from the deepest potential wells. A variation of the extraction potentials themselves is performed at a later stage. The ions' kinematic properties are recorded in the middle of the grounding tube to calculate the ion bunch's emittance.

The emittance of the extracted ion bunch is influenced by two processes. First, by the phase space volume, which is taken up by the ions stored in the trap. This is determined by their temperature and trajectory parameters, as well as the parameters of the trapping potential. Secondly,the emittance is increased by the reheating effects during extraction. Such a reheating of the cold ion ensemble can occur during extraction when already accelerated 'fast' ions collide with a buffer-gas atom along their extraction and acceleration path. To separate those two effects, at first, the phase space in the trap is considered and compared to theoretical expectations. 1000 ions are simulated until they are completely thermalized and then their position and current velocity are recorded. The theoretical expectations on the phase space can be derived from the phase space of a harmonic oscillator, taking the longitudinal and radial trapping potential as the harmonic well potential. The major and minor semi-axes of the ellipse enclosing 95% of the ions can be calculated. For the longitudinal direction this is [34]

$$z_{95\%} = \sqrt{\frac{3k_B T}{eC_2}} \tag{4.6}$$

$$v_{z,95\%} = z_{95\%}\omega_z = \sqrt{\frac{6k_B T}{m}} \tag{4.7}$$

and for the radial direction [34]

$$r_{95\%} = \sqrt{3k_B T \frac{2}{m\omega_r^2}} \tag{4.8}$$

$$v_{r,95\%} = r_{95\%}\omega_r = \sqrt{\frac{6k_B T}{m}} \tag{4.9}$$

with C_2, the deepth and shape parameter of the longitudinal potential, ω_z the longitudinal oscillation frequency, and ω_r the macromotion frequency.

The simulated ions, together with the predicted phase space ellipse, in which 95% of the ions are expected, can be seen in Figure 4.17. In the longitudinal direction, a good agreement between theory and simulations is found. 92% of the ions are enclosed in the 95% ellipse. When taking $340\,\mathrm{K}$ as temperature, as found in the previous simulations, compare section 4.4, this value increases to 94.5% and is in good agreement to the theoretical expectation. In the radial direction, the theoretical description overestimates the phase space, see Figure 4.17b. This is especially true for the position coordinate. This is the case because the harmonic potential used in the theoretical description is less steep than the associated potential generated by the square wave. The insert in the plot shows the radial phase space of an ion cloud in a sinusoidal driven Paul trap together with the theoretical expectation. In this case, a better agreement is observed.

In a next step, the properties of the extracted ion bunch are studied in the field-free region of the grounding tube. In Figure 4.18, the simulated longitudinal and transversal emittance are shown as a function of the longitudinal potential parameter C_2. Two different scenarios are simulated: first, the buffer-gas pressure is kept constant during the complete simulation. Second, the buffer-gas pressure is set to 0 at the time of the extraction. As before, the buffer gas is considered to be non-vanishing only inside the trap, beyond the endcaps perfect vacuum is assumed [3]. The simulated emittances are shown alongside theoretical curves calculated from equation 3.23 and 3.25 for varying ion temperature. The solid line shows the theoretical curve for the temperature, that has been determined for the ions in the trap in the previous chapter.

Both longitudinal emittance curves follow the theoretical trend that a deeper longitudinal trapping potential results in a smaller emittance value, compare 3.23 and 3.10. For larger C_2 values, exceeding $C_2 > 0.2\,\mathrm{V\,mm^{-2}}$, ions can not be successfully trapped any more, as the radial potential is deformed by the longitudinal trapping potential to an extent, at which the ion confinement is lost. The effect of the deepth of the longitudinal trapping potential on the radial trapping potential can be seen in equation 3.11 describing the effective potential. A larger C_2 value decreases the term proportional to r^2, expressing a lower radial trapping potential. In Figure 4.18, only results for potentials which are able to confine all ions are shown.

[3] For a simulation considering buffer gas in the full acceleration region, see section 4.8.

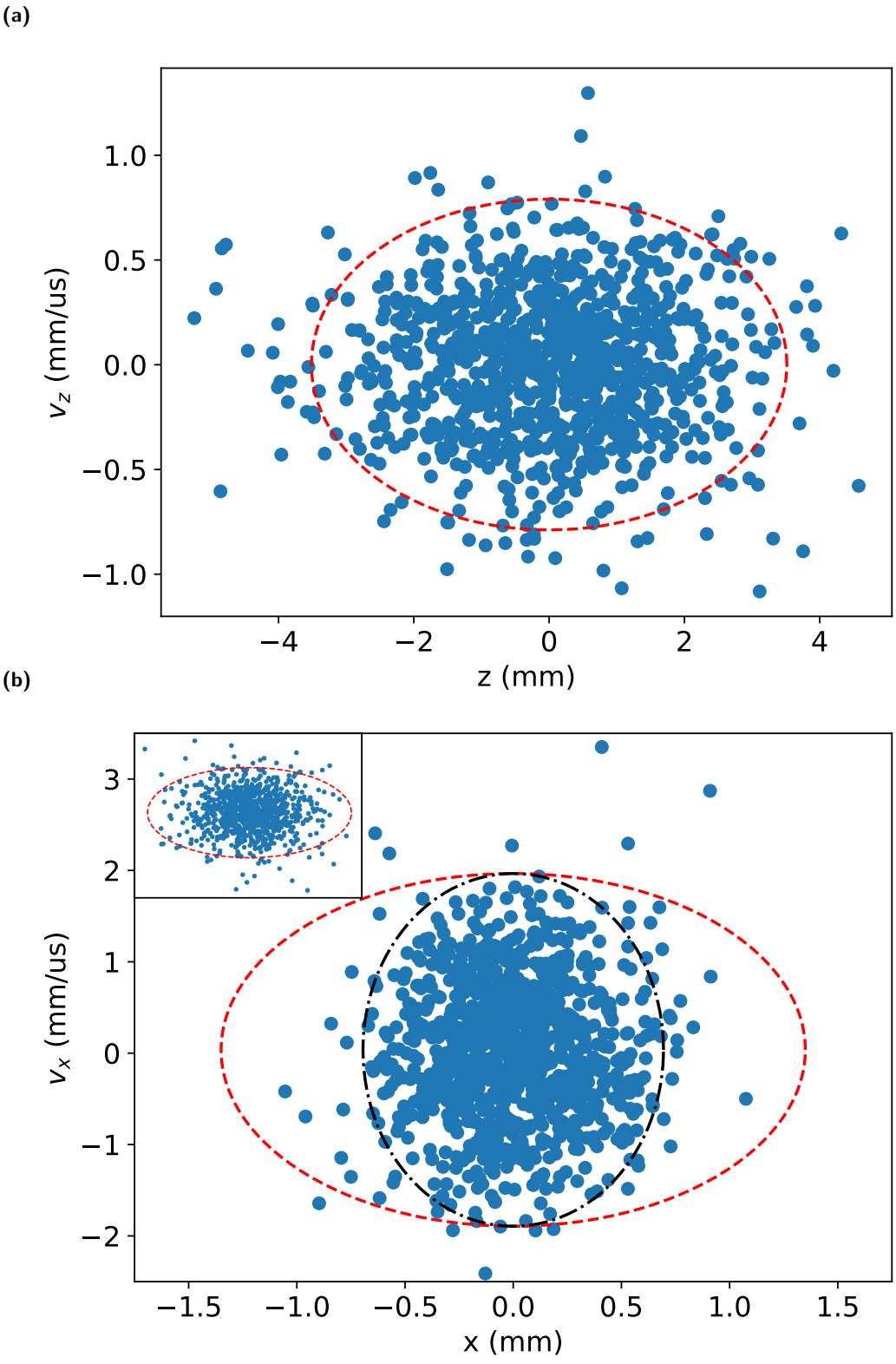

Fig. 4.17: Distribution of the ions in phase space when stored in the Paul trap in longitudinal (top) and radial direction (bottom). Simulated ions are shown by blue dots, the theoretical curve predicted to enclose 95% of the ions is shown in red. The ion temperature for calculating the theoretical curves are 300 K in longitudinal direction and 1800 K in radial direction. For the radial direction, the insert shows a comparison of simulation and theory for a sinusoidal driven Paul trap. The dashed black line indicates the phase space area including 95% of the simulated ions. Simulations are performed with $^{24}Mg^{+}$ ions at a buffer gas pressure of 10^{-2} mbar with a temperature of 300 K. The RF potential was created by an RF amplitude of 240 V and an RF frequency of 1.2 MHz. The used longitudinal potential is shown in Figure 4.4.

As visible in Figure 4.18, the emittance of the simulated ions when simulating helium during the extraction shows a significantly larger emittance than the ones without helium. This is due to collisions with buffer gas during the extraction and acceleration that increase the energy spread and time spread of ions arriving in the grounding tube. Similar to RF reheating inside the trap, the increasing energy spread during the extraction can be described as reheating process and a higher temperature can be assigned to the ion bunch. The exact temperature is determined by a fit with the temperature as the only free parameter, see the dashed lines in Figure 4.18. The reheating effect is larger for small C_2 values, as for the very flat potentials the trapping minima are located further away from the endcap of the trap. Therefore, the path through the buffer gas-filled trap during the extraction is longer and more collisions occur. Thus, the points at small C_2 are not in agreement with the theoretical curve of increased temperature.

For the longitudinal emittance without helium during the extraction it is observed, that the simulated values are smaller than predicted by the theoretical curve at $300\,\mathrm{K}$. The origin of this deviation could not be determined conclusively. One possible explanation could be, that in the theoretical derivation of the emittance in Paul traps, all ion distributions are assumed to be Gaussian. However, the extracted ion bunches clearly deviate from this Gaussian beam shape.

To first order, it is expected that the transversal emittance is independent of the axial C_2 parameter, see equation 3.25. This is to some extent $(0.025 < C_2 < 0.175\,\mathrm{V\,mm^{-2}})$ the case for the simulations when helium is present during the extraction, see dark green data points in in Figure 4.18b. However, such a transverse emittance would correspond to a radial temperature of $2640\,\mathrm{K}$ (see dashed line) and not to the previously found $1800\,\mathrm{K}$ (see black solid line). Such a difference in radial ion temperature could be attributed to the re-heating due to collisions along the extraction, analogously to what is observed in longitudinal direction.

Indeed, the transverse emittance of simulated ions extracted without helium is much lower in value (bright green data points). However, it now shows a dependence on the axial C_2 parameter; for low C_2 values it is even smaller than the prediction of $T = 1800\,\mathrm{K}$ but is steadily increasing with increasing C_2. In order to qualitatively understand this behaviour, a few additional aspects have to be considered.

First, already prior to the the ion extraction the transverse emittance has been found to be compressed compared to the first-order expectation of equation 4.8, see the discussion of Figure 4.17. Thus, a compression factor is extracted from Figure 4.17 as the fraction of the ellipse area in black over the ellipse area in red, to account for the square-wave RF driver. When applying this compression factor, the grey horizontal line in Figure 4.18b is obtained which is lower than the respective simulation results. Second, the deformation of the radial potential due to deeper axial traps has to be considered. Using the effective pseudo-potential approximation from equation 3.11, an additional correction is applied to the emittance estimate based on the compression factor. This correction is finally dependent on the trap depth parameter C_2 and results to an estimated transverse emittance as shown in the dotted line in Figure 4.18b. For C_2 close to 0, this estimate is in fair agreement with the simulation. Moreover, the qualitative increase of the emittance with increasing C_2 is well reproduced although the slope does not reflect the steeper increase. The

results of the simulated emittance is increasing faster with C_2 than the theoretical description does. The origin of this quantitative disagreement is presently not understood.

In Figure 4.19, the simulated longitudinal and transversal emittance as function of the C_2 value are shown for different pressure values. The helium atoms at the same gas pressure are also present during extraction. As the final temperature of the ion cloud in the trap is independent of the pressure, see Figure 4.13, and therefore also the phase space volume occupied by the ions, the difference in the curves is entirely caused by the decreased collision probability during extraction for decreasing buffer gas pressure. Note that the reduction in emittance from $10^{-2}\,\mathrm{mbar}$ to $10^{-3}\,\mathrm{mbar}$ is larger than the decrease by the next magnitude to a pressure of $10^{-4}\,\mathrm{mbar}$.

Finally, the emittance as a function of C_2 was simulated under different RF conditions, while keeping the stability parameter q constant, see Figure 4.20. The longitudinal emittance values are not affected by the changed radial potential. However, larger C_2 values are now possible without losing the ion confinement. In the radial direction, the emittance is decreased by the higher RF amplitude and frequency, due to the deeper radial trapping potential. This is also predicted by the theoretical curve, which directly depends on the RF frequency.

It can be concluded that the reheating due to collisions during the extraction process, represents a significant contribution to the longitudinal and radial emittance. In the pressure regime where the trapping efficiency is sufficiently high and cooling time sufficiently fast, $5 \times 10^{-3}\,\mathrm{mbar}$ to $10^{-2}\,\mathrm{mbar}$, this contribution is dominating. To nevertheless keep the time and energy spread small as required for CLS in an MR-ToF device, the C_2 value should exceed $\approx 0.07\,\mathrm{V\,mm^{-2}}$. Furthermore, the position of the potential minimum should be placed as close to the endcap as possible without creating a large anharmonicity in the longitudinal trapping potential. Future possible strategies to reduce the effect of reheating are to close the Helium supply shortly before the extraction via a piezo-driven valve to decrease the pressure. Another option is a division of the Paul trap into a high-pressure region at the injection side for a high stopping power of the ions, and a low-pressure region at the extraction side, divided by a pumping barrier [35]. This was envisioned in the original design of the trap but was then reduced to one pressure region in favor of a more compact design. If even smaller emittances are required, a cryogenic trap as presented in [35] can be considered since the emittance scales linearly with temperature.

(a)

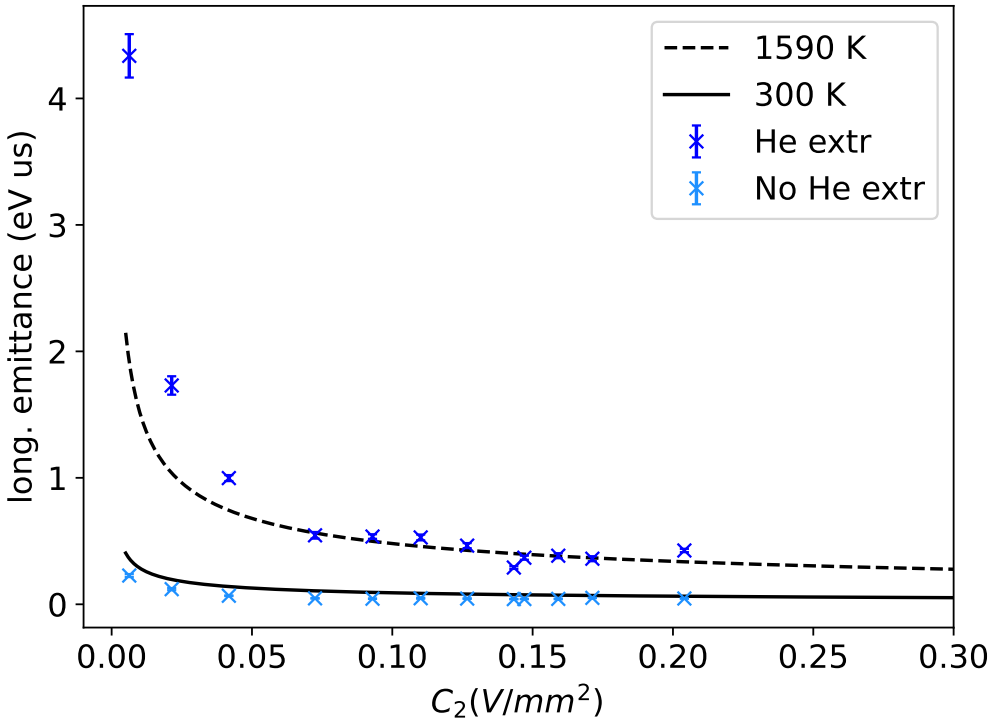

(b)

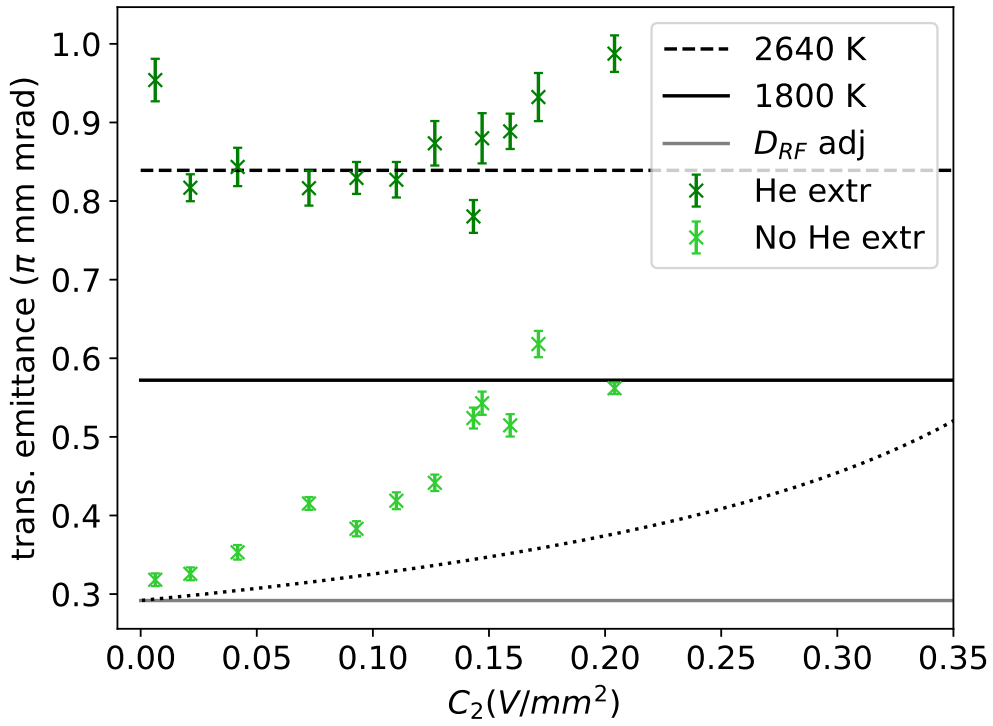

Fig. 4.18: Simulated longitudinal (top) and transversal (bottom) RMS emittance as a function of the longitudinal trapping potential parameter C_2. In each plot, simulations where the buffer gas pressure is kept constant (*He extr*) and simulations where the buffer gas pressure was set to 0 at the time when the electrodes are switched for extracting the ions (*No He extr*) are shown. In black, theoretical curves are shown. The solid lines are for the temperature of the ions, determined from the simulations shown in Figure 4.13, the dashed line indicates an increased temperature. In the plot for the transversal emittance, the grey curve indicates the theoretical calculation with an adjusted trapping depth for the radial potential and the dotted line, a theoretical curve, that considers the deformation of the radial potential by the longitudinal potential. Simulations were performed for $^{24}Mg^{+}$ ions with the RF frequency being $1.2\,\mathrm{MHz}$ and amplitude of $240\,\mathrm{V}$. For interpretation see text.

(a)

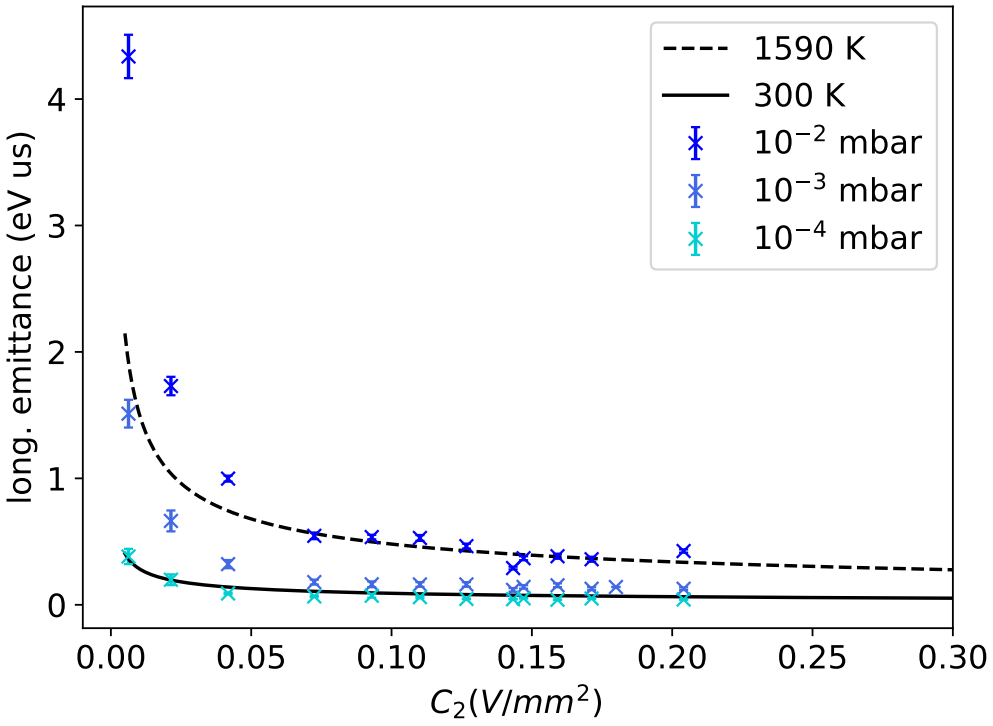

(b)

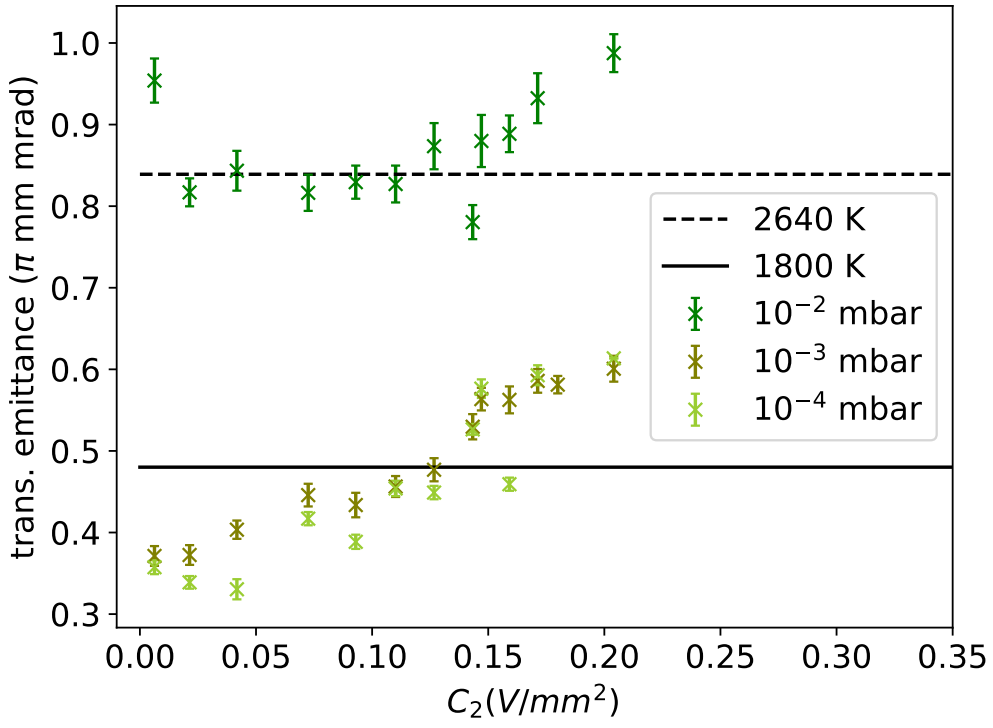

Fig. 4.19: Simulated longitudinal (top) and transversal (bottom) RMS emittance as a function of the axial trapping potential parameter C_2 for different buffer gas pressure in the trap. Simulations are performed for $^{24}Mg^+$ ions with the RF frequency being $1.2\,\mathrm{MHz}$ and amplitude of $240\,\mathrm{V}$. Ions were simulated for at least $5\tau_{1/2}$ at the respective pressure. The pressure was not changed for extracting the ions. Theoretical curves for the temperature of the ions in the trap and for an increased temperature are shown.

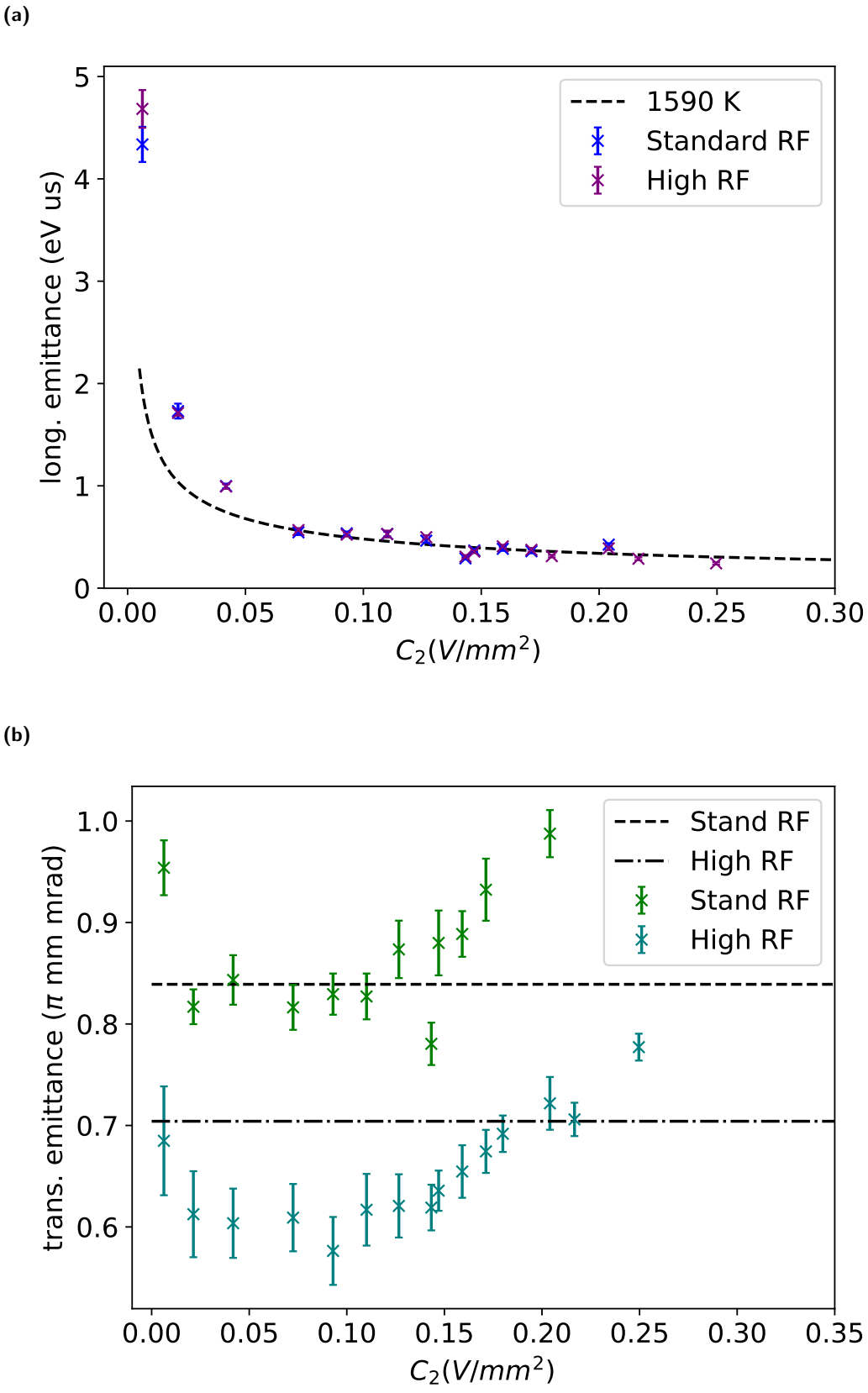

Fig. 4.20: Simulated longitudinal (top) and transversal (bottom) RMS emittance as a function of the axial trapping potential parameter C_2. The simulations are performed for $^{24}Mg^+$ ions for the extraction at a pressure of 10^{-2} mbar. Curves for different RF parameters are shown. Standard RF conditions are $V_0 = 240$ V amplitude and $f = 1.2$ MHz frequency. High RF stands for 400 V amplitude and 1.43 MHz, which translates to the same stability parameter q as the standard RF conditions. The theoretical curves for the different RF conditions are calculated for $T = 2640$ K.

For CLS measurements in the MR-ToF device, not only the longitudinal emittance value is critical, but also the time and energy spread individually. At a fixed emittance value, the energy and time spread can be varied by varying the extraction field. In the following extraction simulations, a potential combination with $C_2 \approx 0.12\,\mathrm{V\,mm^{-2}}$ is used while three different extraction schemes are tested. The used extraction potentials together with the trapping potential are shown in Figure 4.21. The respective voltages applied to the electrodes are given in table 4.2. Finally, the resulting time and energy distributions are shown in Figure 4.22.

Extraction 2 is the simplest extraction pattern. For this extraction scheme, only the endcap and the cone voltages need to be switched, which reduces the costs and complexity of the electronics. However, this scheme introduces a difference in potential before and after switching at the position of the potential minimum. In the realistic case, where the switching of the potential is not infinitely fast, this introduces uncertainties of the starting potential of the ions, which translates into an uncertainty of the kinetic energy in the MR-ToF device [41]. Therefore, two other potentials are additionally tested, for which the potential before and after the switching at the minimum is as close as possible. Note that these schemes require more elements to be switched. For Extraction 1, the last DC segment has to be switched additionally. For Extraction 3 the last two DC segments have to be switched additional to endcap and cone [4].

The time and energy distributions of the ions are recorded in the center of the grounding tube in a field-free region. This position is not the time-focus of the beam, i.e. in the energy-ToF diagram, the enclosing ellipse is rotated. Therefore, the product of time of flight and energy standard deviation is not equal to the longitudinal emittance, but the correlation between both quantities has to be considered according to equation 3.23. The most gentle extraction potential, Extraction 3, shows the largest time spread and the smallest energy spread, see Figure 4.22. For the steep extraction potential, Extraction 2, it is vice versa. Due to the sudden lowering of the potential at the minimum of the ions, the resulting average beam energy is smaller for the steep extraction. As the steeper extraction potential results in a faster extraction, the ions from Extraction 2 arrive earlier.

It is observed that the ion distribution extracted from the same potential well by different extraction methods, shows different emittance values. Theoretically, it is expected that the emittance is conserved under variation of the extraction potential. However, as the different extraction potentials lead to different velocities inside the trap, the reheating effect due to collisions with helium atoms during extraction and acceleration is different. The emittance curves in Figures 4.18, 4.19, and 4.20 are recorded with the steepest extraction potential to also extract from deep potential wells, but this curve shows the highest reheating effect. Using Extraction 3 instead of Extraction 2 reduces the recorded emittance by a factor of 2 compared to what is shown in above figures.

In a next step, which is beyond the scope of the present work, the trajectories of the ions extracted from the Paul trap will be simulated through the complete

[4] For these gentle extraction potentials, the voltage at the cone is comparatively low. Thus, this voltage could be applied continuously to the cone and compensated by a higher potential on the endcap, reducing the number of required switches by one.

Tab. 4.2: Voltages applied to the last DC electrode segments (E8-E12), the extraction endcap (EC), and acceleration cone (Cone), for trapping and three different extraction potentials, see also Figure 4.21.

	E 8 (V)	**E 9 (V)**	**E 10(V)**	**E 11 (V)**	**E 12 (V)**	**EC (V)**	**Cone (V)**
Trap	-45	-45	-45	-100	-170	20	-20
Extr 1	-45	-45	-45	-100	-160	-30	-45
Extr 2	-45	-45	-45	-100	-170	-50	-100
Extr 3	-45	-45	-45	-105	-105	-25	-25

MIRACLS beamline. Their behavior in the MR-ToF ion trap will be studied to verify the suitability of the chosen operation parameters for the subsequent experiment. In a preliminary simulation it has been shown that an ion bunch with time and energy spread of $\sigma_t = 0.40\,\mu$s and $\sigma_E = 0.97\,\mathrm{eV}$, and transversal emittance of $\epsilon_{rms,\mathrm{trans}} = 0.64\pi\mathrm{mm\,mrad}$, could be successfully transferred through the beamline and captured into the MR-ToF device [42]. The beam extracted via Extraction 3 in the present work is characterized by $\sigma_t = 0.27\,\mu$s, $\sigma_E = 0.77\,\mathrm{eV}$, and $\epsilon_{rms,\mathrm{trans}} = 0.54\pi\mathrm{mm\,mrad}$, hence already better than the assumed values for the previous simulation. It is therefore expected that the ion-bunch properties determined as part of this work are suitable for the MR-ToF operation at MIRACLS, too.

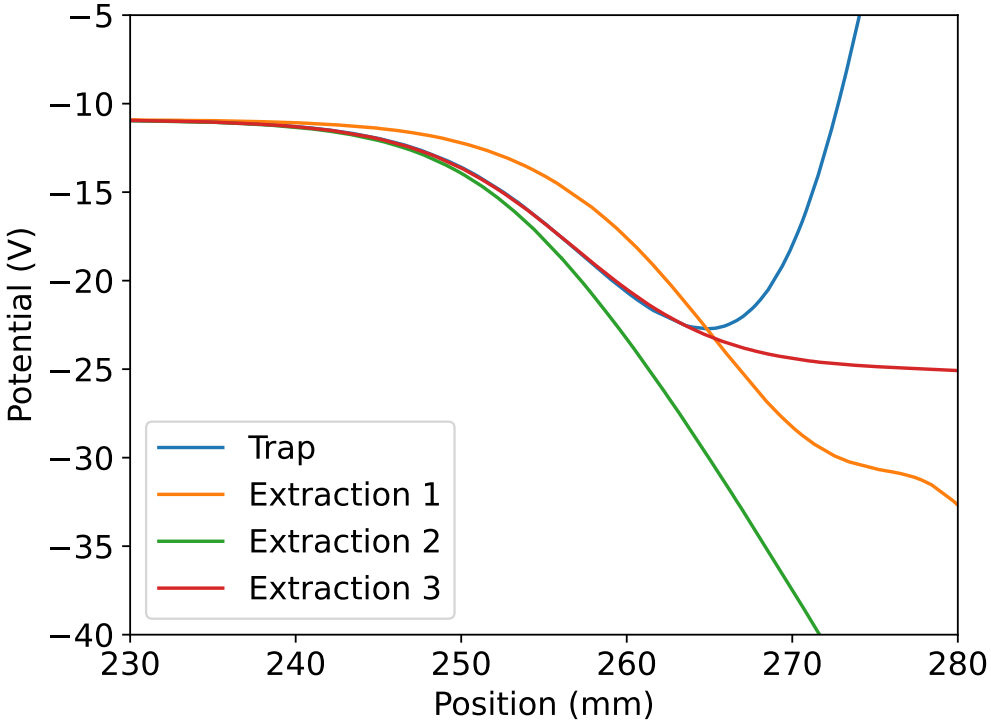

Fig. 4.21: Longitudinal trapping potential and three different extraction potentials.

(a)

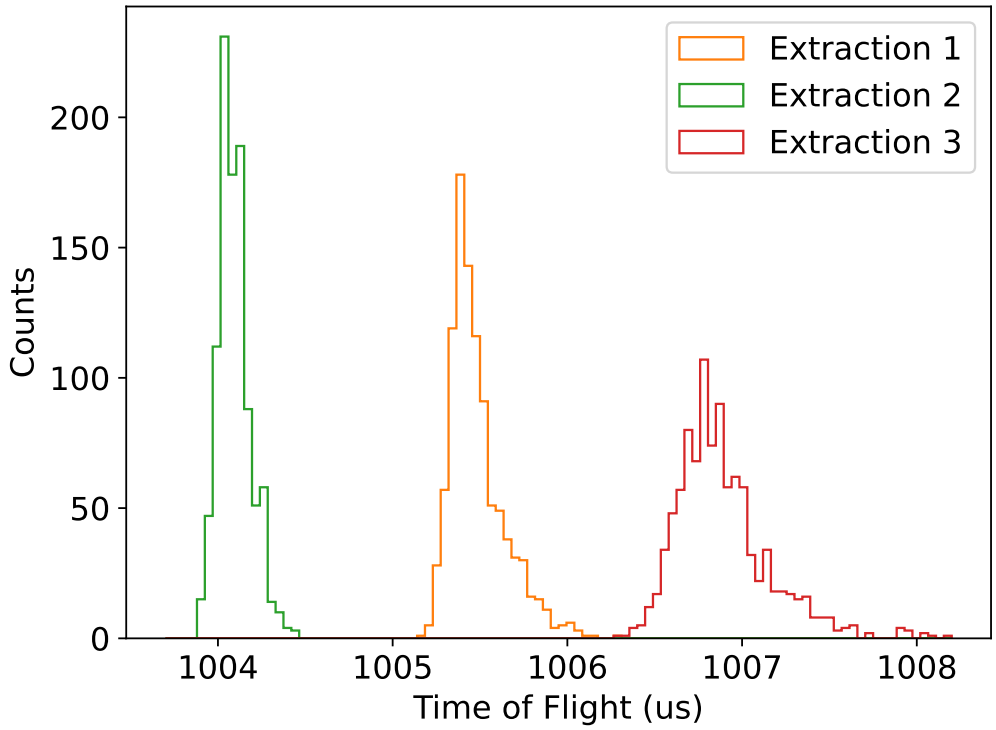

(b)

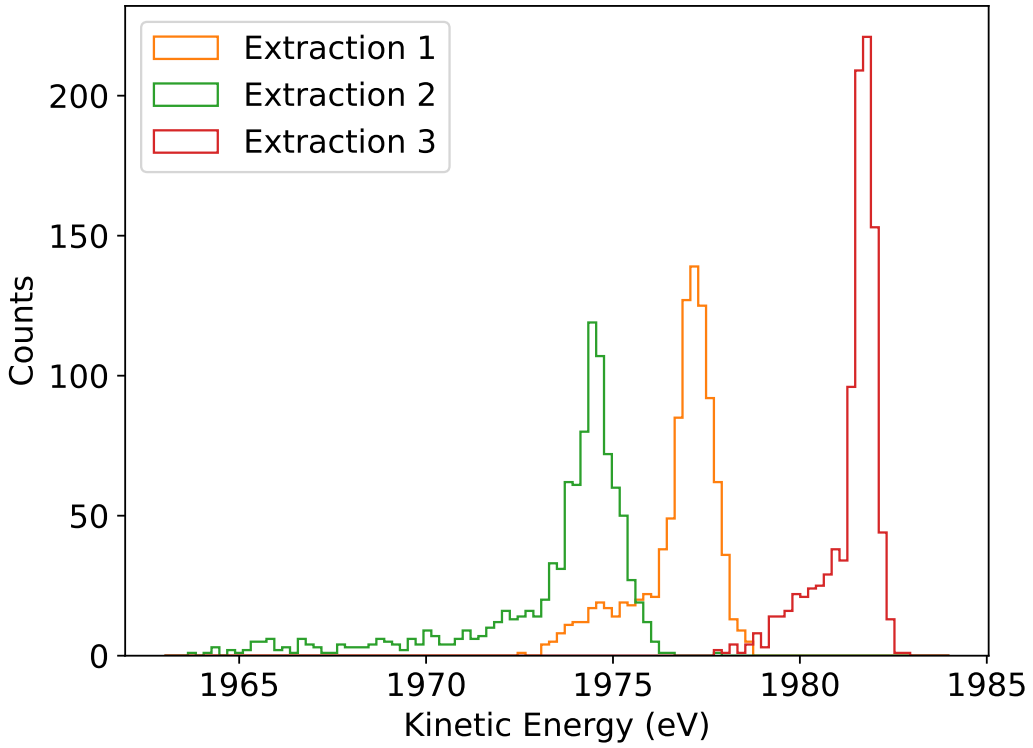

Fig. 4.22: Time and energy distributions of the ion bunch after extraction with different extraction potentials. Simulations are performed for $^{24}Mg^{+}$ ions with the RF frequency being $1.2\,\mathrm{MHz}$ and amplitude of $240\,\mathrm{V}$. The buffer gas pressure in the trap is $5 \times 10^{-3}\,\mathrm{mbar}$. The longitudinal trapping potential is characterized by $C_2 \approx 0.12$ and shown in 4.21.

4.7 Vacuum simulations

The buffer gas pressure required in the Paul trap ($10^{-2}\,\mathrm{mbar}$ - $10^{-3}\,\mathrm{mbar}$) for ion stopping and cooling and the excellent vacuum conditions in the MR-ToF device ($10^{-8}\,\mathrm{mbar}$ - $10^{-10}\,\mathrm{mbar}$), required to reduce ion losses during the MIRACLS measurement, impose a challenge on the design of the vacuum system. Furthermore, it has to be considered, that the ISOLDE beamline is equipped with valves, that will only open if the pressure in the subsequent MIRACLS beamline is better than $5 \times 10^{-6}\,\mathrm{mbar}$ and will be closed again if the pressure exceeds $2 \times 10^{-5}\,\mathrm{mbar}$ [43].

To verify that these requirements are fulfilled by the currently planned vacuum system, simulations of the pressure induced by the buffer gas in the Paul trap are carried out using the open-source simulation tool Molflow [44]. Molflow performs Monte Carlo simulations of gas particles moving in a given geometry. Only collisions of particles with the geometry are considered, but no particle-particle collisions. Therefore, the simulations are only applicable to the molecular flow regime, where the mean free path of the gas is larger than characteristic geometric dimensions. The mean free path for helium at room temperature at $10^{-2}\,\mathrm{mbar}$ is only $12\,\mathrm{mm}$, but at $10^{-4}\,\mathrm{mbar}$ it is already $1.2\,\mathrm{m}$, much larger than the diameter of the simulated vacuum chambers. It is therefore concluded, that the molecular flow regime is suitable for simulating the pressure outside the Paul trap itself, but the pressure distribution in the Paul trap has to be interpreted with caution.

The simulation geometry includes the MIRACLS beamline section from its connection to ISOLDE all the way to the quadrupole bender in MIRACLS' 2-keV beamline section, thus featuring three vacuum chambers. In the 3D CAD software Inventor, a model was created, that features only the hollow parts of the beamline geometry. This model is exported and imported into Molflow, see Figure 4.23. A gas flow rate of $0.1\,\mathrm{mbar\,L\,s^{-1}}$ is assigned to the helium supply tube reaching into the Paul trap. The turbomolecular pumps are simulated by assigning pumping speeds to flanges of the size of the pump. The used pumps were a CF100 pump with a pumping speed of $255\,\mathrm{L\,s^{-1}}$ and a CF160 pump with $655\,\mathrm{L\,s^{-1}}$, both values for helium gas.

The results of this simulation are shown in Figure 4.24. In the Paul trap itself a pressure of $7.6 \times 10^{-3}\,\mathrm{mbar}$ directly at the helium inlet, and $6.4 \times 10^{-3}\,\mathrm{mbar}$ and $5.8 \times 10^{-3}\,\mathrm{mbar}$ at the up- and downstream endcap are determined. The pressure in this simulation scales linearly. When the pressure in the trap is increased by a certain factor, all other pressures scale about the same factor. Directly outside of the Paul trap, still in the vacuum cross of the trap itself, the pressure is simulated to be $2 \times 10^{-4}\,\mathrm{mbar}$. The differential pumping sections on each side of the Paul trap greatly reduce the pressure in the neighboring vacuum chambers. The immediate drop in pressure in the left differential pumping section is larger, as this tube is equipped with a small aperture of $10\,\mathrm{mm}$ diameter. The use of such a small aperture is possible due to the expected small spatial spread of the ion bunch coming from the Paul trap. On the ISOLDE side, a small aperture is unfavorable due to the risk of potentially losing ions of rare isotopes. To compensate for the larger opening, the differential pumping section is longer.

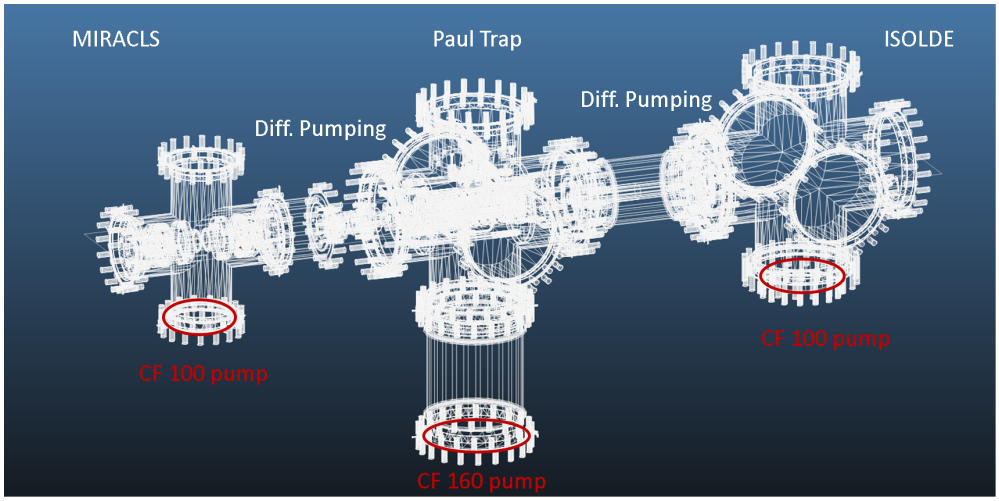

Fig. 4.23: Geometry used for the Molflow simulations. The connection to the ISOLDE beamline is on the right part of the picture, the subsequent beamline to the MIRACLS MR-ToF device on the left part.

Three different scenarios for the employed pumps are simulated, see Figure 4.24, that lead to the same behavior for the Paul-trap chamber and differential pumping regions, but show different pressures at the connection to ISOLDE and the following MIRACLS beamline. Scenario one (blue curve) features a CF160 pump directly underneath the Paul trap, and two CF100 pumps under the two other crosses. This configuration results in a pressure of $\approx 10^{-5}\,\mathrm{mbar}$ towards the remainder of the MIRACLS beamline. This is deemed sufficiently good, as in the subsequent beamline additional vacuum pumps will be utilized and the MR-ToF device itself will be equipped with a set of strong turbomolecular pumps.

On the ISOLDE side, a pressure of $8.7 \times 10^{-6}\,\mathrm{mbar}$ is determined, which is too high for the ISOLDE gate valve to open, but sufficient to not close once it is already open. One strategy of operation could be, to initially reduce the gas inflow into the Paul trap, open the gate valve and then increase the gas flow to reach the desired operating pressure again. In the second scenario (green curve), the CF100 pump on the first cross next to the ISOLDE beamline is exchanged by a CF160 pump. This results in a pressure of $3.4 \times 10^{-6}\,\mathrm{mbar}$, sufficiently low to open the gate valve even at normal helium gas flow. In the third scenario (red curve), the pumping setup is identical to scenario 1 but it is considered, that the beamline sections outside of the simulated volume, also can have a pressure reducing effect due to good vacuum quality. On the ISOLDE side, directly upstream of the gate valve, a CF100 pump is installed. In the simulation, it is assumed that half of its pumping power acts towards the MIRACLS beamline. Also on the MR-ToF end of the simulated volume, half of the pumping power of a CF100 pump is assigned. On the ISOLDE side, this decreased the pressure by about 22%. On the MIRACLS side, the pressure is even reduced by 50%. The slope of pressure in this section is due to the set of einzel lenses positioned in the cross, that act as a weak differential pumping section.

It can be concluded, that the currently envisioned vacuum system for the MIRACLS Paul trap is compatible with the vacuum requirements on the ISOLDE side. When a CF100 pump is used (scenario 1), the opening of the gate valve has to be performed

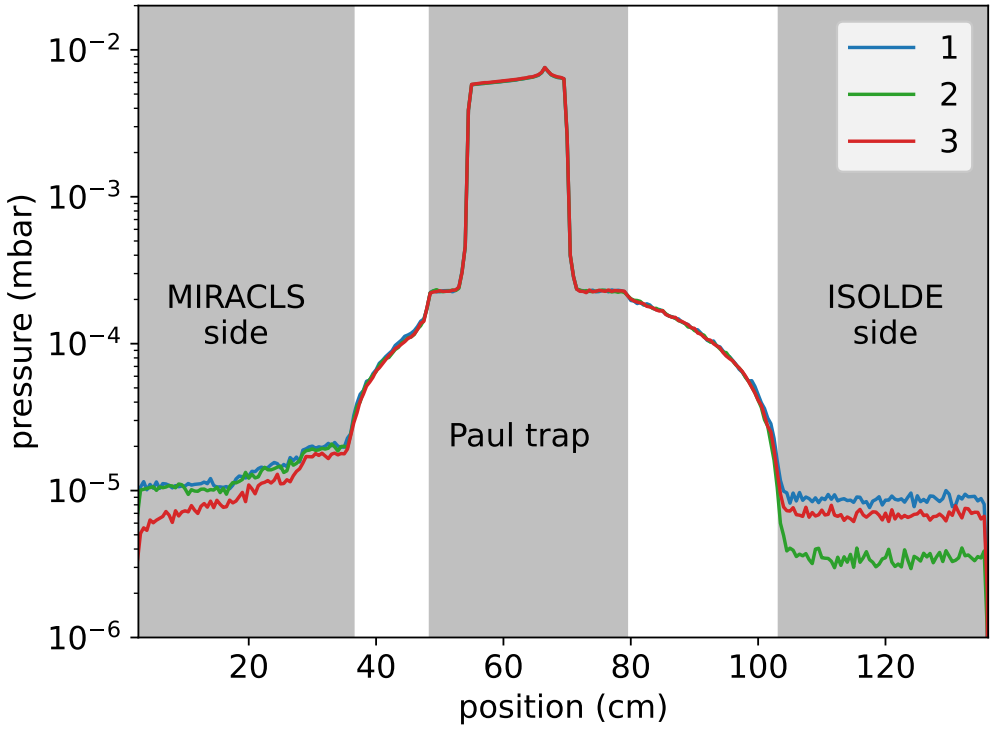

Fig. 4.24: Resulting pressure versus position in the center of the vacuum system induced by filling the Paul trap with buffer gas. The different sections of the beamline are marked by the background color. On the right side, but outside of the simulation region, the ISOLDE beamline is situated. The rightmost shown section is a CF160 chamber, the following section is a differential pumping region, then the Paul trap chamber follows, then a second differential pumping region, and then one CF100 chamber, after which the remainder of the MIRACLS beamline follows. Three different scenarios are simulated: A CF160 pump under the Paul trap section, and one CF100 pump under the two other chambers (1), the CF100 pump on the right CF160 chamber replaced by a CF160 pump (2) and finally considering additional pumping effect from the connecting ISOLDE beamline (3), i.e. when the valve to the ISOLDE transport beamline is open.

with reduced helium pressure in the trap, when a CF160 pump is installed (scenario 2), the valve can be opened at normal helium pressure.

4.8 Impact of gas flow simulation on ion simulation

All previously discussed simulations regarding ion injection and ejection into and from the Paul trap assumed that the buffer gas is exclusively present inside the Paul trap itself. Outside of the endcaps, perfect vacuum has been assumed. As it has now been determined by the gas-flow simulation, the pressure inside the Paul-trap cross is also not negligible. Thus, the ion simulations are revisited in the following.

For the injection simulations from the offline ion source, a pressure of $5 \times 10^{-3}\,\mathrm{mbar}$ of buffer gas inside the trap is assumed. According to the gas-flow simulation shown in Figure 4.24, this results in a pressure of $1.5 \times 10^{-4}\,\mathrm{mbar}$ between the trap and the grounding tube. Inside the grounding tube, the pressure is assumed to be zero. Furthermore, the parameters from Figure 4.5 are applied, namely a floting bias of $0\,\mathrm{V}$, RF amplitude of $240\,\mathrm{V}$, and RF frequency of $1.2\,\mathrm{MHz}$. The injection efficiency decreased from 68.6% to 63.4% due to the buffer gas surrounding the trap. When assuming the same pressure in the grounding tube as in the Paul-trap cross, as a worst-case-scenario, the injection efficiency decreased to 61.2%. Thus, the performance of ion injection from the offline ion source is only slightly affected. The obtained intensity is sufficient for MIRACLS operation.

For the extraction simulations, a pressure of $10^{-3}\,\mathrm{mbar}$ inside the trap was assumed to compare it to the results presented in Figure 4.19. In accordance with the pressure simulations, the pressure outside of the trap is thus assumed to be $3 \times 10^{-5}\,\mathrm{mbar}$. The used longitudinal potential is characterized by $C_2 \approx 0.12\,\mathrm{V\,mm^{-2}}$. The RF amplitude is $240\,\mathrm{V}$ and the RF frequency is $1.2\,\mathrm{MHz}$. These are the same Paul-trap conditions as in Figure 4.22. When analyzing the properties of the extracted ion bunch, an ellipse enclosing 95% of the ions is fitted to the distributions in the time and energy plane. In the present scenario, it is expected that the 95%-emittance delivers a better measure of the beam quality, as the RMS emittance is strongly increased by single ions with a vastly lower energy due to a collision at high energy. Without helium outside of the trap, a longitudinal emittance of $\epsilon_{95\%} = 0.92\,\mathrm{eV\,\mu s}$ has been determined [5]. Considering helium pressures along the complete simulation geometry this value increases to $5.2\,\mathrm{eV\,\mu s}$ while, with helium only in the Paul-trap cross, but not in the tube, the longitudinal emittance is $2.3\,\mathrm{eV\,\mu s}$.

The emittance value when there is helium outside of the trap is much larger than what is required for the subsequent CLS measurement in an MR-ToF device. However, for the kinetic energies reached in the extraction ($2\,\mathrm{keV}$), the validity of the used collision model has to be questioned. In the hardsphere model, a constant cross section based on the dimensions of the atom and ion is used. In reality, the cross section for ion-atom interactions decreases for higher ion velocities [45]. Also, in the hard-sphere model isotropic scattering is assumed but the differential cross section indicates that scattering occurs stronger in forward direction at higher energies, reducing the impact of a collision [46]. No cross-section data for $^{24}\mathrm{Mg}^{+}$ ions and $^{4}\mathrm{He}$ could be found to quantify this effect. The energy dependence of the cross section is of greater importance for the extraction, where the number of collisions greatly alters the energy spread, than for inside the trap, where the ions and buffer gas are close to thermal equilibrium. Even in this scenario, it is observed, that the hard-sphere model overestimates cooling times due to a deviating cross-section at low temperature [47]. It is therefore expected, that the emittance of the ion bunches extracted from the Paul trap at the background pressure found in the Molflow simulations is significantly lower than the results of the present simulation with helium gas all along the ions' acceleration path.

[5] For this simulation $\epsilon_{\mathrm{RMS}} = 0.17\,\mathrm{eV\,\mu s}$. The conversion factor of 6 between RMS and 95% emittance results in slightly different values, as the ion bunch is not completly Gaussian. This discrepancy increases massively for simulations with more collisions.

5 Towards the commissioning of the Paul trap at MIRACLS

In this chapter, the mechanical design of the Paul trap and the associated mounting structure are presented together with a description of the assembly process and alignment of the trap in the cross. The electrical system of RF and DC electrodes and the helium supply system in-vacuum and in-air are described. A test beamline for the first commissioning of the Paul trap is presented, alongside an outlook of the complete commissioning process including online beam from ISOLDE.

5.1 Mechanical design of the Paul trap

The assembled Paul trap can be seen in Figure 5.1. All electrodes were manufactured from 316L stainless steel, which is chosen over the commonly used 304 stainless steel due to the lower magnetic permeability. A fine surface finishing prevents electric field distortions. The RF rods were additionally treated in a tension relief heating cycle to minimize bending of the rods by the mechanical strain induced during the machining. The electrical insulators are machined from MACOR ceramics, which combines a high voltage hold-off capability with UHV compatibility.

The assembly of the Paul trap is started with a stack of DC electrodes and ceramic insulator rings. The ceramic rings are placed into a grove in the DC electrodes, to ensure geometrical alignment. The rotation of the insulator ring is fixed by a vented threaded rod, that is mounted to the DC electrode and sits in an indentation in the ceramic ring. The RF electrodes are held by two DC electrodes, electrically separated by ceramic split bushes. The inner surface of those two DC electrodes is flattened at the mounting positions to ensure a stable and aligned mounting of the RF electrodes.

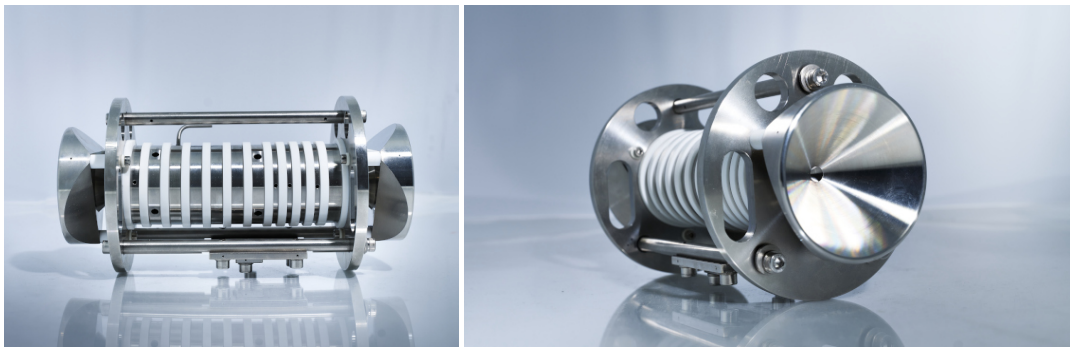

Fig. 5.1: Photographs of the assembled Paul trap. The Paul trap is positioned upside down in this picture. In the left picture, the upstream side is on the left side. The RF electrodes are not included in this assembly. Pictures taken by [48].

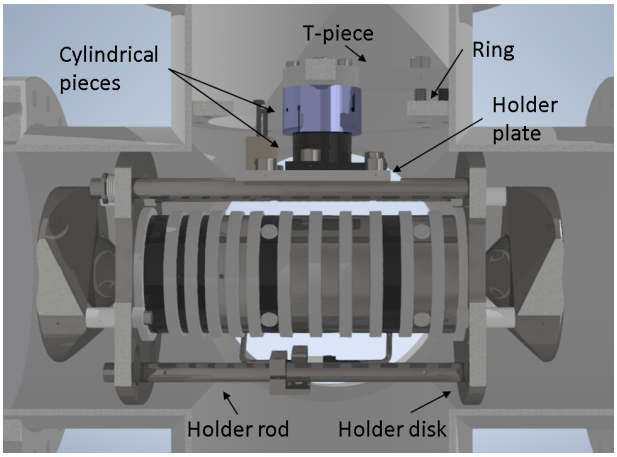

Fig. 5.2: CAD model of the Paul trap mounted into the cross via the mounting structure shown in Figure 5.3.

The last DC electrode on each side of the stack has an adapted design to allow the mounting of the endcaps, which are screwed onto those electrodes while insulated by ceramic split bushes. This stack of DC electrodes and insulators, with the RF electrodes enclosed, is inserted into a holder structure, consisting of two disks and three rods, as marked in Figure 5.2. On one side springs are inserted between the disk and supporting screws, mounted to the rods to ensure sufficient pressure is applied to the electrode stack. The cones for injection and ejection are mounted to the holder structure. On the long vertical rods of the holder structure, a plate is mounted, that features three dowels, which align the Paul trap with a mounting structure inside the vacuum cross.

The CF160 vacuum cross, which hosts the Paul trap, features a welded ring, in which three dowel pins are inserted. These fix the alignment of a T-shaped holder piece, on which a cylinder with three dowels is mounted, see Figure 5.3. The dowels of the holder piece and the dowels mounted on top of the Paul trap are inserted into a cylindrical spacer with tight-fitted holes for the dowels. This ensures the exact alignment of the trap, also for repeated insertions into the cross. The weight of the trap is carried by a screw, that reaches through the complete mounting structure into the plate on top of the Paul trap.

The alignment of the trap with respect to the vacuum cross was determined by laser fiducialization performed by the CERN Survey team. In the initial configuration, the trap showed a tilt downwards on the downstream side of $0.3°$ and a rotation of $0.9°$ towards the right side, looking from the upstream side onto the trap, with respect to the axes of the vacuum cross. Furthermore, a vertical offset of $1.6\,\mathrm{mm}$ and horizontal offset of $1.3\,\mathrm{mm}$ of the injection and ejection cone centers to the centers of the flanges were measured. The rotation of the trap was corrected by manufacturing a new T-shaped holder piece with rotated positions of the three screw holes close to the center of the piece. The tilt and offsets were corrected by adjusting the height of the three dowels in the ring individually. The elongated spherical grooves on the backside of the t-shaped holder piece, allow for a tilt and a shift of the center of this piece.

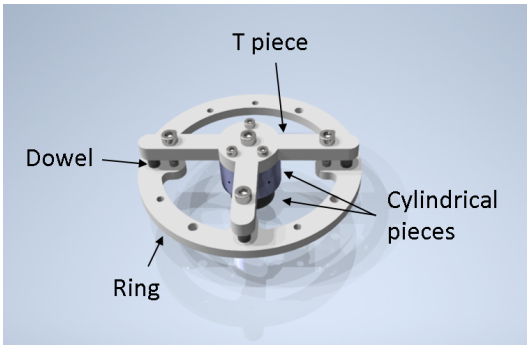

Fig. 5.3: CAD model of the mounting structure for the Paul trap. The ring is welded into the vacuum cross. The dowels screwed into the ring can be used to adjust the tilt and offset of the trap inside the cross. The lowermost cylinder is attached to the top of the Paul trap, the trap is then inserted from the side into the cross, aligned by the dowels fitting into the cylindrical piece, and attached via the central screw, that reaches through all pieces.

5.2 Electrical connections and Helium supply to the Paul trap

The DC voltages for the 12 electrodes, two endcaps and two cones, are supplied by iseg EBS C0 05 and EDS F1 30 modules, operated in an ECH 244 crate. The used channels of the modules are connected to a converter box with SHV sockets as input and a D-Sub connector as output. A D-sub cable connects the converter box with a D-Sub-feedthrough, welded into a flange of the Paul trap vacuum cross. On the vacuum side, a Kapton insulated D-sub ribbon cable with MACOR connectors is used. A further D-Sub connector is mounted to the Paul trap holder. The pins of this connector are crimped to Kapton insulated silver plated copper wires, which are screwed on the other end of the wire via a ring terminal lug onto a threaded rod, which is mounted on each DC electrode. The injection and ejection cones are connected via the same type of wire directly to SHV feedthroughs on the same flange. This is necessary because the cones will be supplied with a potential higher than $500\,\mathrm{V}$, which is the maximal rating for the D-sub connector.

The RF electrodes are electrically connected via one of the threaded rods, which is also used for mounting the RF electrodes. The pair of RF electrodes, which carry the same phase of the field, are connected via short wires to each other. Onto this connection, a third wire is crimped in a Y-shape, which connects the two short wires with a bare wire power feedthrough. The two sets of wires, and the two short wires on each set, have exactly the same lengths to avoid phase differences between the electrodes and are overall kept as short as possible to keep the capacitance of the trap low. The two insulated wires from the trap to the feedthrough are twisted around each other and inserted into stainless steel shielding braid to reduce the emission of RF radiation into the cross. On the atmosphere side, the bare wire feedthrough is connected to a pair of insulated cables, also twisted and inserted into a stainless steel shielding. A connector box, that connects those cables to the connector of the RF generator is built.

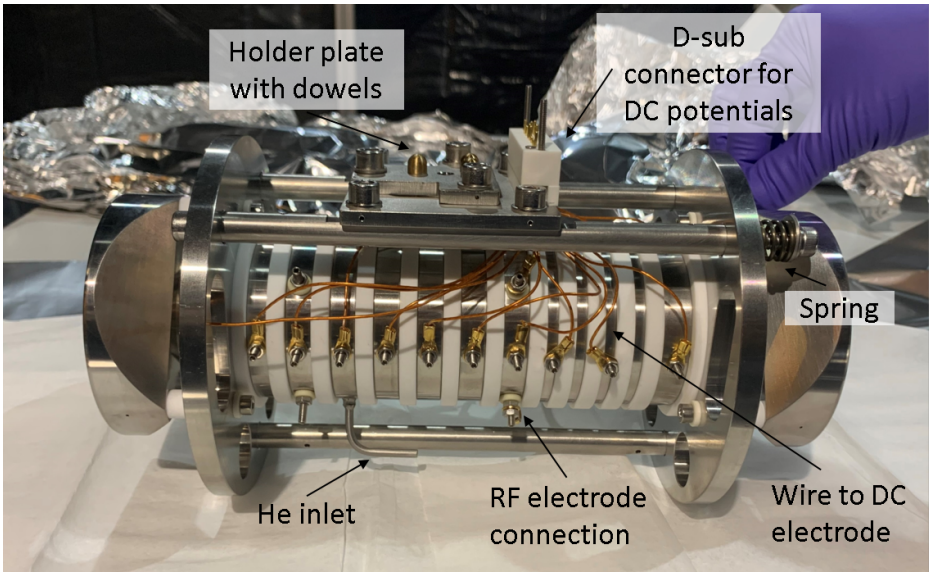

Fig. 5.4: Picture of the Paul trap including the cabling for the DC electrodes and RF electrodes.

The RF signal is supplied to the trap by a CGC AMX400-2ED power switch with two associated power supplies. To achieve optimal switching behavior, the RF driver is tuned to the capacitive load. For this, the capacitance of the RF electrodes including the cables and feedthrough has been measured with a handheld capacitance meter. This resulted in the power switch being tuned to a load of $100\,\mathrm{pF}$. For such a capacitive load, the switch showed a switching time (10% to 90%) of $15\,\mathrm{ns}$ for rising and falling signal for an RF amplitude of $\pm\ 200\,\mathrm{V}$.

The buffer gas is supplied to the trap volume by a 1/8 inch tube welded onto one DC electrode. A tube insulator separates the potential of this DC electrode from the floating potential of the surrounding cross. The insulator is supported by a stainless-steel holder mounted onto the rods of the trap holder. The insulator is connected to a 1/8 inch to 1/4 inch tube connector, which is the diameter of all following tubing. A flexible stainless-steel bellow connects through a CF40 T-piece and a tube to a gas feedthrough. On the second branch of the CF40 T-piece, a full-range pressure gauge is mounted. On the atmosphere side, the feedthrough is connected with a bellow to a mass flow controller, followed by a T-piece. One end is connected to a valve, followed by a bellow to the pressure regulator of a helium bottle. The other end also features a bellow valve together with an adapter to KF25, to be able to evacuate the gas system before injecting helium.

The Paul trap with DC and RF wiring, as well as the tube for the helium supply, can be seen in Figure 5.4.

5.3 Paul trap teststand

Before assembly of the MIRACLS beamline, the Paul trap will be tested and commissioned independently. For this purpose, a short test beamline has been designed, see

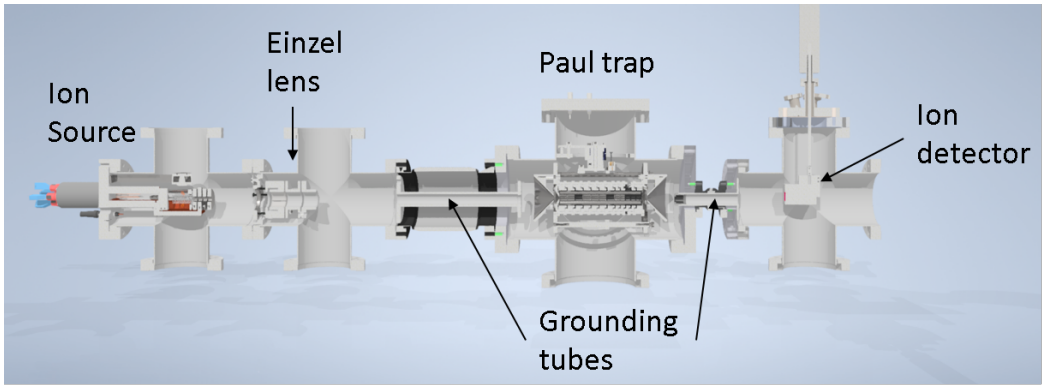

Fig. 5.5: CAD model of the test beamline, consisting of an ion source (left), injection optics, the Paul trap cross and an ion detector (right).

Figure 5.5. The test beamline consists of an ion source, injection optics, the Paul trap cross as described above, and a cross equipped with an ion detector. On both sides of the Paul trap cross, ceramic breaks are mounted to separate the floating potential of the cross and the remaining beamline. Inside the insulators, stainless steel tubes of smaller radius are mounted as differential pumping sections and to ensure a well-defined electric potential seen by the ions.

This simplified beamline features an ion detection directly behind the Paul trap, which could not be realized in the final beamline due to space constraints. Furthermore, easy access to the Paul trap is given in case adjustments have to be made.

As the ion source, a gas-filled electron impact ionization source was chosen over the magnesium source that will be used later on. The operation principle is identical, but the gas can be directly injected into the source instead of being evaporated in an oven inside the source. The gas source is chosen for initial testing due to the higher ion current available and the easier operation of the source without refilling of solid magnesium. The gas ion source is planned to be operated with nitrogen (N_2^+ with $m = 28u$) , as the mass is similar to magnesium, it is inert, and widely available.

For the ion detection system, a magneTOF detector of type ETP 14925 MagneTOF Mini is used. In a magneTOF detector, the ions entering the detector impinge on a cathode, where secondary electrons are released. The electrons are transferred by a crossed electrostatic and non-uniform magnetic field between dynodes to amplify the current, which is finally measured [49]. The detector is mounted via an aluminum holder structure onto a pneumatic linear drive. The linear drive is attached to a multi-port flange, together with the SMA feedthrough required for the signal read-out and the SHV feedthrough required to provide the operating voltage.

All chambers are equipped with turbomolecular pumps connected to a common pre-vacuum pump to achieve the desired vacuum levels. The pump on the Paul trap cross is a CF160 pump connected via a ceramic insulator to be able to operate the pump on the same potential as the other pumps and therefore to attach them to the same pre-vacuum pump. On both the ion source cross and the detection cross a CF100 turbomolecular pump is attached.

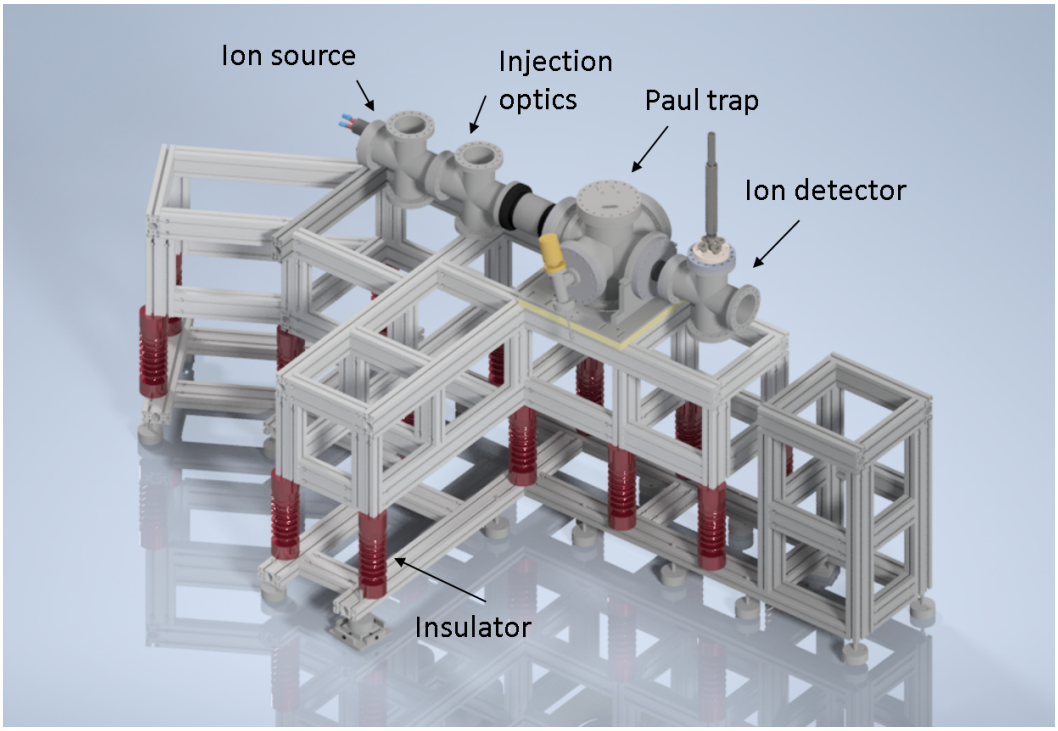

Fig. 5.6: CAD model of the test beamline on the profile structure, that will later hold the 2 keV-section of the MIRACLS beamline.

The chambers are mounted via aluminum chamber mounts, that allow adjusting the height, position, and tilt of each vacuum chamber individually. The chamber mounts are fixed to an aluminum profile structure, that will later hold the complete beamline section, see Figure 5.6. This profile structure features hard rubber insulators, that separate the potential of the beamline from the ground. The complete structure can be adjusted in height and position. The Paul trap chamber will be enclosed by a high-voltage protection cage, that will be attached to the rack, housing the required electronic components.

5.4 Status and next steps

At the time of submitting this thesis, the Paul trap was fully assembled. The internal electrode cabling and the tubing for the Helium were completed. The two sections that will make up the beamline up- and downstream of the Paul trap vacuum cross, are readily assembled, as well as the grounding tubes in the CF insulators, which connect the beamline sections. The beamline can be vacuum sealed, as soon as the alignment of the trap in the cross is confirmed by a final laser fiducialization procedure.

As a first step of establishing the Paul trap operation, all DC electrodes will be held on ground potential, while transmitting a continuous beam of ions from the ion source to the magneToF detector. This ensures that the beamline is aligned with sufficient accuracy and all elements are operational. As the energy distribution of the ion beam emitted by the nitrogen ion source is less well known, the floating

potential of the Paul trap should be scanned, while recording the number of ions still passing through, to determine the boundaries of the energy distribution and find a suitable floating potential for the trap. To avoid overloading the trap with ions, a switchable blocking potential will be applied to the upstream endcap. During the loading time, this potential will be lowered to allow ions to enter the trap. Next, the longitudinal and RF trapping potentials will be applied. It is expected, that when loading ions, only part of the ions are reaching the detector, while the rest of the ions remain trapped. The trapping parameters can now be varied within the desired region of parameters, which were determined in the simulation study in the previous chapter, to maximize the percentage of trapped ions. Finally, the extraction of the ion bunch should be validated by applying the extraction potential after the desired cooling time. The ratio of the detected ion counts for shooting the ion beam through the trap for a given loading time, compared to the ion number for activated trapping and extracted ion bunches, provides an indication of the injection and trapping efficiency.

Following this verification of the Paul trap functionality with the gas-filled offline ion source injecting from the position of the ISOLDE beam, the reverse offline injection with the magnesium ion source as well as injection of ISOLDE beam will be tested. For this endeavor, the ion source cross will be replaced by a CF160 vacuum chamber, that will house beam diagnostics and ion optics, and will be connected to the ISOLDE beamline. The detection cross is replaced by a CF100 cross housing two einzel lenses, followed by the quadrupole bender, like in the planned MIRACLS beamline, shown in Figure 2.4. On one perpendicular branch of the quadrupole bender, the offline ion source will be mounted. On the branch in straight beam direction, the detection section will be installed. In this setup, the offline reverse injection can be tested, as well as taking beam from ISOLDE.

In the next stage of construction, the MR-ToF device will be built and commissioned with ions from the offline ion source, cooled and bunched in the Paul trap. The first beamtime for laser spectroscopy on radioactive ions with the MIRACLS approach is foreseen for spring 2022.

Active Voltage Stabilization

6

In this chapter, an active voltage stabilization system for sensitive beamline potentials is presented. Firstly, the motivation for this study is outlined, then the setup and results achieved for applying this technique to one beamline element of an MR-ToF device combined with laser cooling ions in the Paul trap are presented. Those results motivated a more systematic study of applying the active voltage stabilization to multiple elements of an MR-ToF device and analyzing the remaining noise signals after stabilization.

6.1 Motivation

Voltage fluctuations of potentials applied to beamline elements impose a limit to precision experiments. Even though modern power supplies provide a high intrinsic stability (e.g. $< 1 \cdot 10^{-5} V_{\mathrm{nom}}$ stability and $< 20\,\mathrm{mV}$ ripple and noise [50]), remaining fluctuations are observable and may lead to a reduction in the mass resolution in mass spectroscopy experiments or in resolution and system stability in collinear laser spectroscopy [51].

For the Paul trap operation as cooler and buncher, the potential at the trapping minimum is most critical: The potential at the minimum determines the ion energy for the following experiment. Fluctuations in this potential at the time of ejection from the Paul trap lead to different ion energies, which may result in a laser-spectroscopic line width broadening or instability. Furthermore, it causes a change in time-of-flight in the MR-ToF device. The ToF peak broadens for longer measurements and the mass resolution decreases. For the same reasons the stability of the voltages that compose the ion mirrors in the MR-ToF ion trap is important too. The influence of voltage fluctuations in the MR-ToF device is expected to be even larger than the effect of fluctuations in the Paul trap, as the ions in the MR-ToF device are exposed to the potentials for several thousand times as they are revolving between the two mirrors.

Therefore, the possibility to implement a voltage stabilization and the resulting improvement on the measurement resolution are studied with the aim to apply the procedure to the MR-ToF device and the Paul trap of the MIRACLS experiment.

6.2 Voltage stabilization for laser cooled ions

The voltage stabilization study is performed on the MR-ToF device of the MIRACLS proof-of-principle experiment. The schematic of this setup is shown in Figure 6.1.

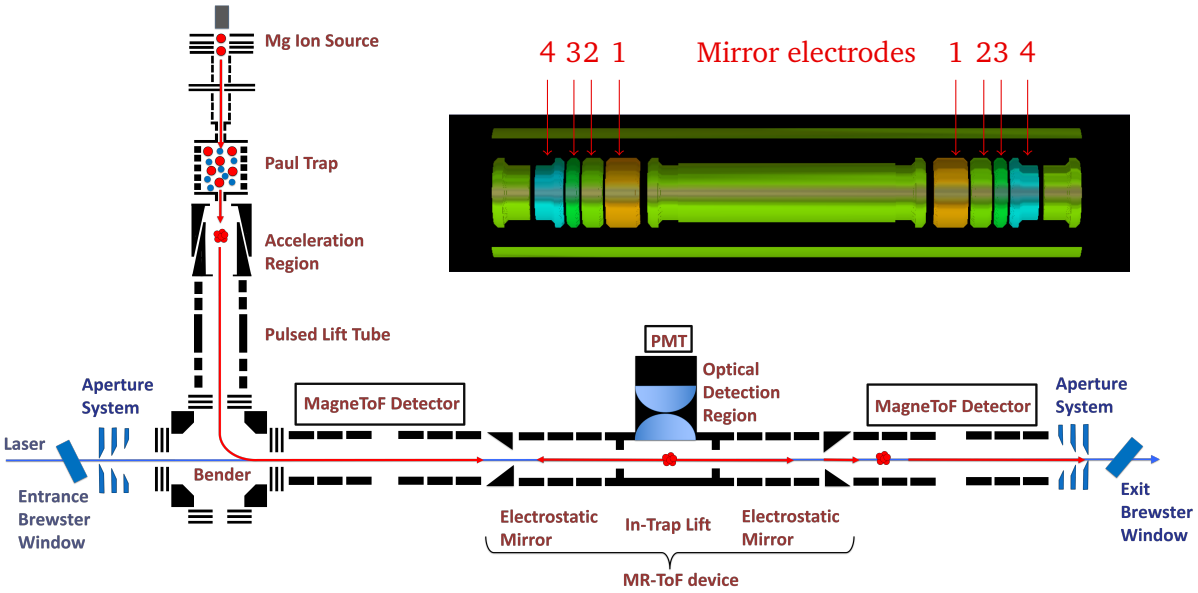

Fig. 6.1: Schematic of the MIRACLS proof-of-principle experimental setup. The ions are generated in the ion source, bunched and cooled in the Paul trap and guided into the MR-ToF device. The inset shows the electrode system of the MR-ToF ion trap, which consists of two mirrors composed of four mirror electrodes enclosing the central drift tube. Figure modified from [16].

An offline electron-impact-ionization ion source produces continuously stable magnesium ions. The ion beam is injected into a linear Paul trap, that is driven by a sinusoidal RF field, where the ions are cooled and ejected from the trap as ion bunches. The ions are accelerated to an energy of about $2.3\,\mathrm{keV}$, then bent onto the laser axis and injected into the MR-ToF ion trap. The MR-ToF device consists of two pairs of four mirror electrodes surrounding the central drift tube. Instead of the usual detection of fluorescence photons emitted from the ions in the MR-ToF device, when performing CLS, for the voltage stabilization measurement, the ions are detected after ejection from the MR-ToF device with a MagneTof detector.

For the first measurement series, the ions are not cooled by buffer gas cooling as usual but by laser cooling, as explained in section 3.3. For the realization of this cooling technique, the setup has to be modified: The ion source is mounted via an additional quadrupole bender orthogonal to the Paul trap to allow laser access into the Paul trap. As cooling laser, a narrow band, continuous wave dye laser with a fundamental wavelength of $560\,\mathrm{nm}$ is frequency-doubled to $280\,\mathrm{nm}$ to reach the wavelength of the D2 transition in $^{24}\mathrm{Mg}^{+}$. The cooling is performed with a slight negative detuning from the transition frequency.

The setup of the voltage stabilization of a mirror electrode is divided into two components: A low pass RC-filter (passive stabilization) and a PID loop running on a computer (active stabilization), that adjusts the set value of the power supply based on the voltage measured at the electrode via a voltage divider and multimeter. Figure 6.2 shows a schematic of the setup. The aim of the passive stabilization is to filter fast voltage fluctuations and reduce the noise that is measured at the

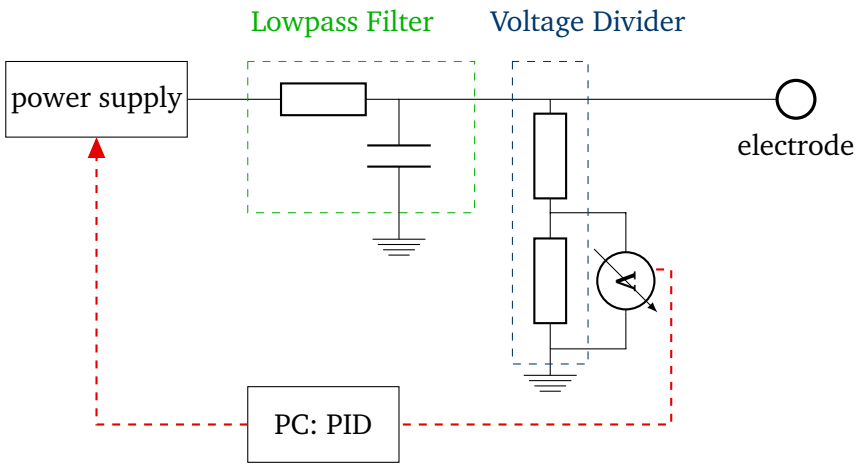

Fig. 6.2: Circuit diagram of the active voltage stabilization. The voltage supplied by the power supply to the MR-ToF is stabilized by a lowpass filter in a passive way and over a voltage divider and multimeter with a PID loop in an active way.

electrode. The active stabilization counteracts long-term drifts of potentials. As one revolution in the MR-ToF device takes about $7\,\mu$s, but the voltage readout with the multimeter takes about $20\,$ms, the active stabilization is not capable of reducing fluctuations on the time scale of the revolutions in the trap. On the other hand, the time constant of the RC-filter should not be increased to also filter out fluctuations seen over a complete measurement run, as the long charging time of the capacitor leads to several impracticalities for the actual operation of the MR-ToF device, for instance when changing the potentials for tuning. Therefore both the active and the passive stabilization component are required for reducing the noise and stabilizing the voltages on longer time scales.

For the following measurements, the 3 outer mirrors (2,3, & 4) are passively stabilized via an RC-low-pass filter, utilizing a capacitor of $40\,\mu$F and a resistor of $1\,$MΩ. The voltage of mirror 4 of the MR-ToF is actively stabilized by a PI loop implemented in LabView (from [51]). The voltage at the electrode is read out by a digital multimeter (Keithley DMM7510) via a voltage divider.

The effect of an active stabilization is investigated for trapping the ions for about 4000 revolutions in the MR-ToF device by comparing the ToF peak width with and without stabilization, see Figure 6.3. It can be seen that the FWHM is reduced by 29.8% through the stabilization, which translates to an equal gain in mass resolving power. With the combination of laser cooling the ions in the Paul trap and actively stabilizing the voltages of the ion mirrors in the MR-ToF device the highest measured mass resolving power of $R \approx 243000$ for this set-up so far has been reached for about 2000 revolutions in the MR-ToF device.

These promising results motivate a more systematic investigation of the effects of an active voltage stabilization system on the individual mirror potentials and the overall ToF stability and to extend it to all four mirrors of the MR-ToF ion trap.

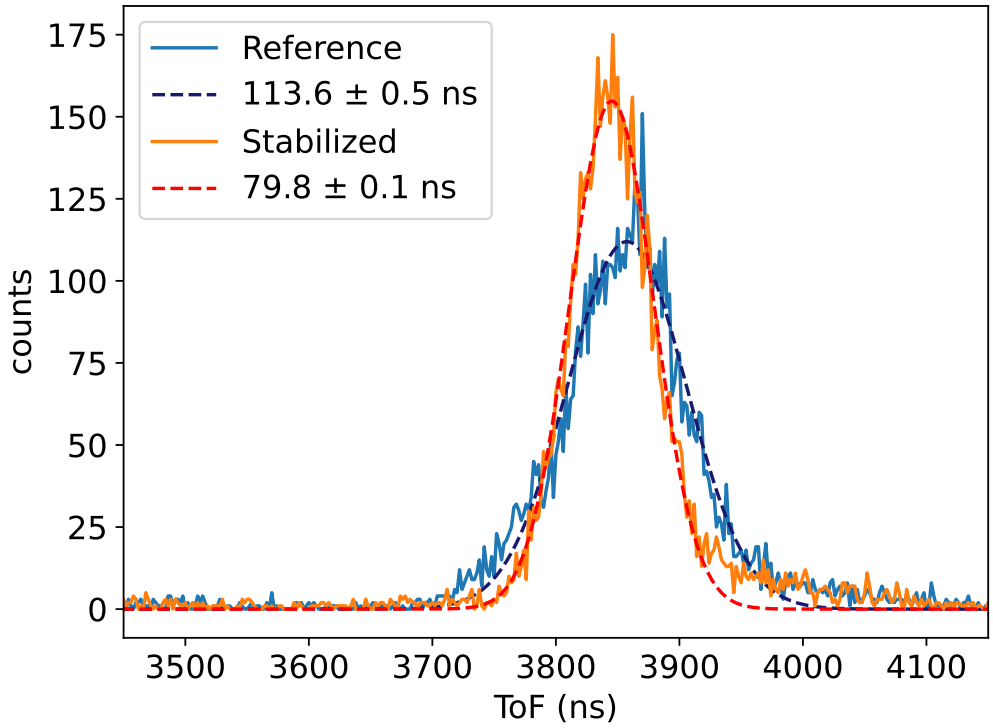

Fig. 6.3: Accumulated ToF signal of laser cooled ions. For the orange curve, the active voltage stabilization is activated and for the blue curve, only the passive stabilization is included. Both peaks are fitted with a Gaussian distribution and the FWHM is given in the legend.

6.3 Stabilization setup for all mirrors

The stabilization concept of mirror 4 is now extended to all mirrors of the MR-ToF device: For the passive stabilization, two self-built low-pass filters are used, composed out of a capacitor of $40\,\mu\mathrm{F}$ and a resistor of $1\,\mathrm{M}\Omega$. For the active voltage stabilization, two different types of voltage dividers are available: through-hole voltage dividers (CADDOCK HVD5-A20M-050-05, 1000:1) that are mounted into a protective housing and one standalone high-precision voltage divider (Ohmlabs KV-30A). For the voltage measurements two 7.5 digit multimeters (Keithley DMM7510), one 7.5 digit multimeter (Keithley 2001), and one 8.5 digit multimeter (Keithley 2002) are used. The voltages are supplied by iseg EHS ($< 1 \cdot 10^{-4} V_{\mathrm{nom}}$ stability and $10\,\mathrm{mV}$ noise and ripples), EBS ($< 1 \cdot 10^{-5} V_{\mathrm{nom}}$ stability and $20\,\mathrm{mV}$ noise and ripples) and NHR modules ($< 2 \cdot 10^{-4} V_{\mathrm{nom}}$ stability and $10\,\mathrm{mV}$ noise and ripples).

The PID loop is implemented in Labview. The script follows a producer-consumer architecture to decouple the readout and computation of the set-value from the sending of the value to the power supply, which allows for overall faster execution of the script, as new values from the multimeter can be read-in and processed, while the sending process is still ongoing. The DMM7510 multimeters are read out via Ethernet, the Keithley 2001 and 2002 via GPIB. The EHS and EBS voltage modules are controlled via the SNMP protocol and the NHR module via the SCPI protocol. For each mirror, one separate LabView script is executed.

To decide which hardware is used to stabilize each mirror, a sensitivity study of the mirrors is conducted, see Figure 6.4. The voltage of one mirror is changed, then a ToF spectrum is recorded with 500 shots of ion bunches in the MR-ToF device. Each ion bunch contains about 10 ions. The ions undergo about 4000 revolutions in the MR-ToF ion trap before being ejected onto the MagneToF detector. The resulting ToF peak is fitted with a Gaussian distribution and the relative change of the centroid of this distribution is shown over the relative change in voltage. The fit uncertainty is smaller than visible in the plot.

It can be seen that mirror 1 is the most sensitive, followed by mirror 2 and 4, while mirror 3 shows only a small influence on the time-of-flight. Based on this measurement, the stabilization setup is determined, see table 6.1. The low pass filter units for the passive stabilization are added to mirrors 2 and 4, as the voltage of mirror 1 is higher than the maximal rating of the capacitor used in the unit, and mirror 3 shows the smallest sensitivity. The high potential of mirror 1 can only be measured by the stand-alone Ohmlabs voltage divider. The remaining voltages are measured via the self-mounted Caddock voltage dividers except for mirror 3, where the potential can be measured without division.

6.4 Results

In the first place, the effect of only the passive stabilization is studied, see Figure 6.5. The noise of the voltage signal is significantly reduced, but fluctuations on longer timescales are remaining.

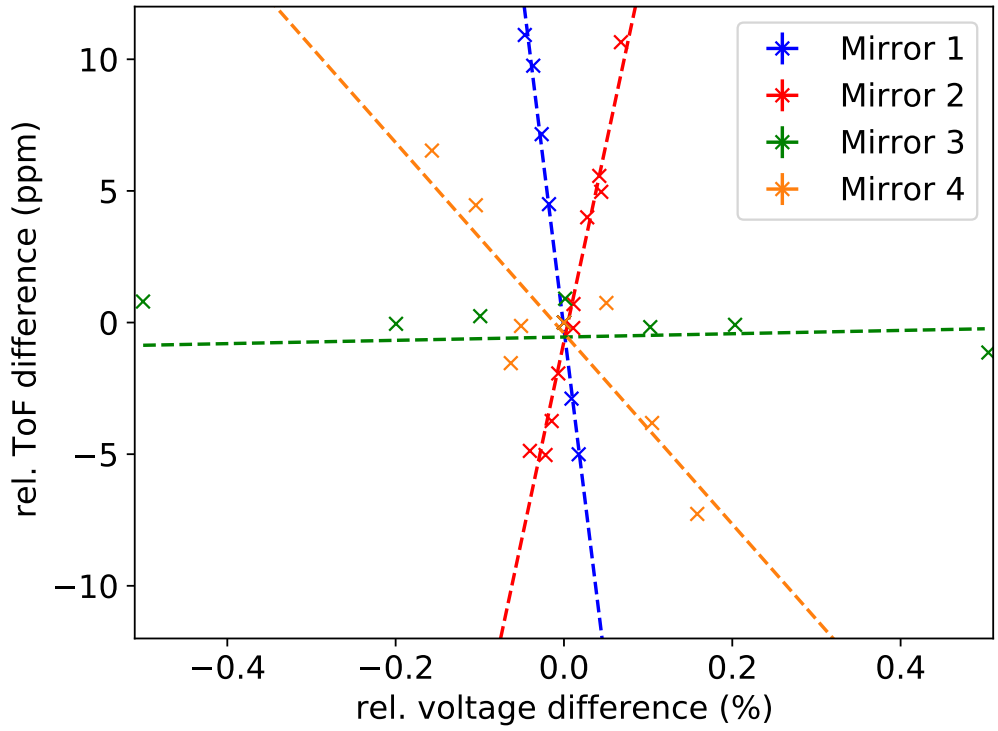

Fig. 6.4: Sensitivity of the ion time-of-flight to changes of the respective mirror potential.

Tab. 6.1: Configuration of the voltage stabilization setup for the different electrodes based on the ToF sensitivity towards voltage fluctuations and the voltage. The sensitivity is extracted from the measurements shown in Figure 6.4.

Mirror	Voltage (V)	Sensitivity	Voltage Divider	Multimeter
1	-4776.80	$2.59 \cdot 10^{-2}$	Ohmlabs	2001
2	1215.77	$1.50 \cdot 10^{-2}$	Caddock	DMM7510
3	995.24	$6.27 \cdot 10^{-5}$	-	2002
4	1883.40	$3.62 \cdot 10^{-3}$	Caddock	DMM7510

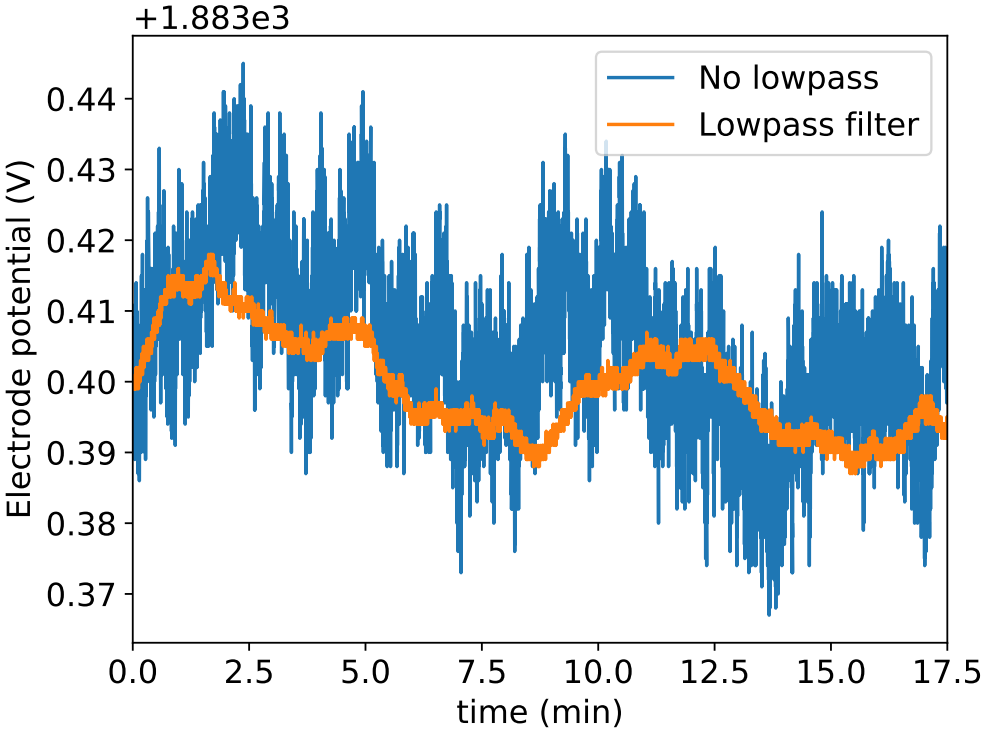

Fig. 6.5: Voltage over time of mirror 1 recorded once with passive stabilization (lowpass filter) included and once without.

With an activated active voltage stabilization those slow fluctuations are further reduced, see Figure 6.6. The stability improvement for each mirror potential and the ion ToF is given in table 6.2, while the resulting accumulated ToF signal from each measurement run is shown in Figure 6.7.

When comparing the voltage signals of the different mirrors with each other in Figure 6.6, the effect of the passive stabilization on mirrors 2 and 4 is directly visible: the overall relative noise level is much smaller than the one of mirrors 1 and 3. The difference between mirrors 1 and 3 could be based on two effects: Mirror 3 is measured without an additional voltage divider, which could induce additional noise, and mirror 3 is measured with the more precise multimeter. When

Tab. 6.2: Noise level of the ion ToF signal and the voltage with and without active voltage stabilization expressed as the standard deviation of the relative fluctuations.

	No / Passive Stab (ppm)	Active Stab (ppm)	Improvement (%)
Ion ToF	1.05	0.67	36.2
Mirror 1	18.16	16.04	11.7
Mirror 2	3.02	0.66	78.2
Mirror 3	8.64	5.69	34.1
Mirror 4	3.70	0.56	84.9

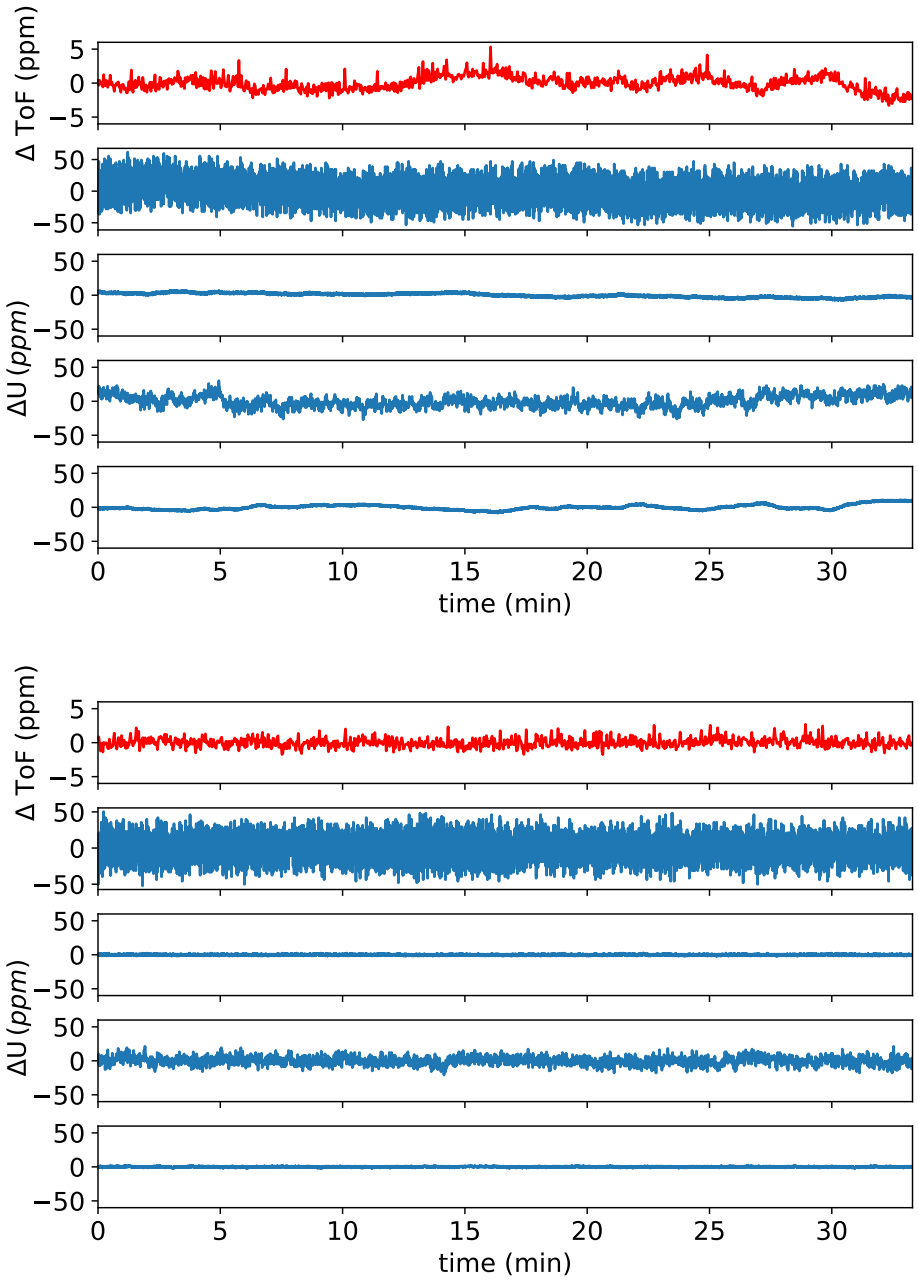

Fig. 6.6: Comparison of the ion ToF (red) centroid and mirror voltages (blue, mirror 1 to 4 from top to bottom) over time without (top) and with activated active voltage stabilization (bottom). Mirrors 2 and 4 are in both measurements additionally passively stabilized. For each measurement point shown in the plot, the ToF centroid is determined from 20 shots of ions containing about 7.5 ions each.

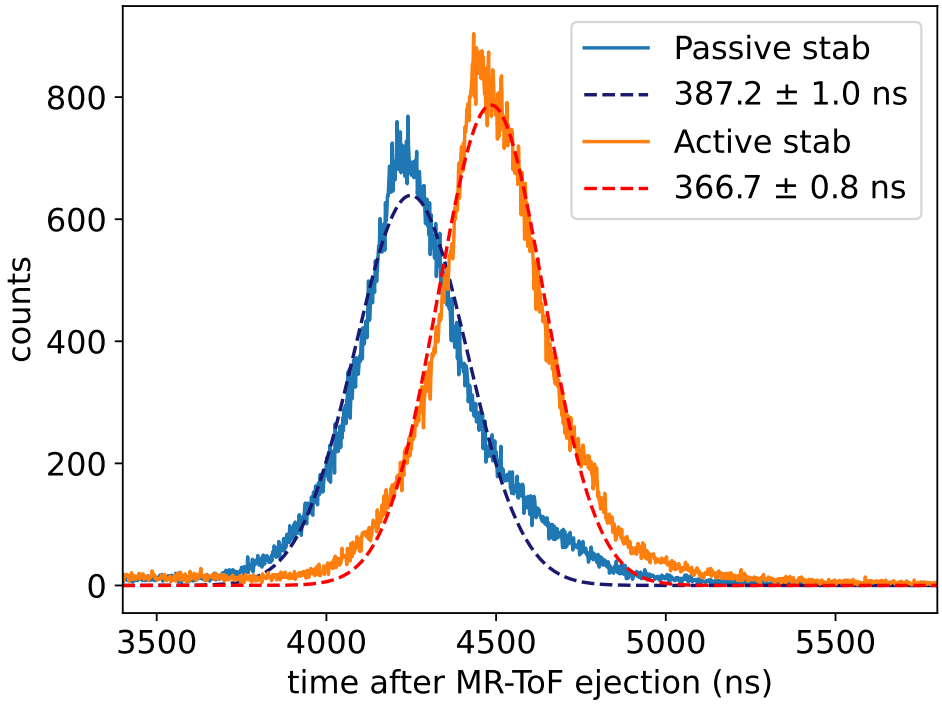

Fig. 6.7: Cumulated ToF signals of one measurement run with partially passive stabilization (blue) and active stabilization (orange) and the respective fit with Gaussian distributions. The FWHM determined in the fit is given in the legend.

considering the stability improvement between the two measurement series, mirrors 2 and 4 show the highest decrease in fluctuation level. This demonstrates that the passive stabilization not only decreases the overall noise level by filtering out the fast fluctuations, but it also leads to a more functional active voltage stabilization as the comparatively slow-performing PI loop receives a time-averaged input and is, therefore, able to correct the long-term fluctuations without overreacting to small fluctuations. Mirror 1 has the lowest stability gain, which can be explained by the high noise level of the unstabilized voltage.

The ion ToF fluctuations decrease when activating the PI loop on the voltages, see red curves of Figure 6.6, showing the ion ToF centroid of each measurement interval. This shows that indeed voltage fluctuations limit the precision of ToF measurements in the MR-ToF device and therefore the mass resolving power. To judge the effect on the mass resolving power, the cumulative ToF peak has to be considered, see Figure 6.7. Besides the accumulated ion data from the two measurement runs above, a Gaussian fit for each run is shown. The shift between the two peaks can be explained by a drift of voltages in the reference measurement from the set-point of the PI loop for the active stabilization. It can be observed that the FWHM decreases when switching on the active stabilization. The decrease in peak width is significantly smaller than the before observed decrease of stability for the ion ToF, as given in table 6.2. From the higher gain in stability than decrease in peak width, it can be concluded that the peak width is mainly governed by the ToF width within each measurement interval and less by the fluctuations between the measurement intervals, as those were significantly reduced. This indicates that the stability should be further improved on the time scale of one measurement interval to further increase the mass resolving power.

The remaining noise on the signal can be investigated by the means of the Allan deviation

$$\sigma_y(\tau) = \sqrt{\frac{1}{2} < (\bar{y}_{i+1} - \bar{y}_i)^2 >} \quad , \tag{6.1}$$

where $\bar{y}_i$ is a measurement value averaged over the sample period τ [52]. The Allan deviation is calculated from the sample to sample fluctuations of one measurement instead of the difference of single values to the measurement average, as the standard deviation, and is, therefore, a better estimator for the measurement stability and also allows to distinguish between different types of noise. Observing the Allan deviation as a function of the sample period gives insight to noise on different timescales. In Figure 6.8 the Allan deviation of one mirror voltage and the ion ToF signal with and without the active voltage stabilization is shown. The error of the Allan deviation calculation on a finite data set of length N is given by

$$\delta(m) = \frac{1}{\sqrt{2(\frac{N}{m} - 1)}} \quad , \tag{6.2}$$

where m denotes over how many measurement values y is averaged, with $\tau = m\tau_0$, where τ_0 is the measurement period [53]. The relative error increases with increasing τ, therefore only values up to a relative error of 50% are shown in Figure 6.8.

In the Allan deviation plot of the voltage (Figure 6.8 top) it can be seen that in general the voltage without stabilization shows the highest level of instabilities. With the passive stabilization, the Allan deviation decreases for small averaging times, which shows stability for this sample time region. An Allan deviation decreasing with increasing sample time is a sign of a stable measurement signal, as noise is averaged out by the longer sampling periods. The increase of deviation with longer sampling times is a sign of slow drifts and fluctuations. For the active voltage stabilization (including a passive voltage stabilization), the initial decrease in deviation is less pronounced than for the passive stabilization, indicating that the PI loop introduces also additional fluctuations. Towards larger time scales the deviations for the active stabilization stay significantly lower than with the passive stabilization demonstrating a positive effect at large sampling times. The high fluctuations on all curves for large sampling times are due to low statistics and should be excluded from the analysis of the noise sources. For a signal, that is solely impaired by the white noise of the measurement, a $1/\tau$ dependence is expected. This cannot be observed for any of the curves, indicating that there are still additional noise sources present.

In the Allan deviation plot of the ion ToF (Figure 6.8 bottom), the ToF signal, measured with two mirrors not stabilized and two mirrors passively stabilized (blue), shows a behavior similar to the passively stabilized voltage curve: first increasing stability and decreasing stability towards large sampling time, but less pronounced than for the voltage curve. The explanation for this is that ToF stability is directly influenced by the voltage stability and only two out of the four mirrors are stabilized, therefore decreasing the magnitude of the stabilization effect. For the active stabilization (orange), a continuous decrease in deviation can be observed, but the slope is not steep enough to only contain white noise. It is expected that the stability will increase further when all four mirrors are passively stabilized, especially as it has been shown earlier that the active stabilization shows a larger improvement of stability on signals that are already passively stabilized.

6.5 Conclusion and Outlook

It can be concluded that the implemented stabilization on the MR-ToF device mirrors shows a significant improvement in the mirror voltage stability, leading to a stabilization of the ion ToF centroid and through this to an increase in mass resolving power. An especially high impact is observed during ToF measurements of laser-cooled ions: Although only a simplified version of the stabilization is applied there, the mass resolution power increases by about 30%. At the same time, several improvement possibilities are identified: By adding a lowpass filter to the most sensitive mirror (mirror 1) an even higher ToF stability is expected. This was not possible so far, as no capacitor rated for more than $5\,\mathrm{kV}$ with a sufficiently high capacitance could be acquired. The addition of the low-pass filter is expected to not only filter the fast fluctuations but also to enable better performance of the active stabilization. By an analysis of Allan deviation plots it is also noticed that even on a passively and

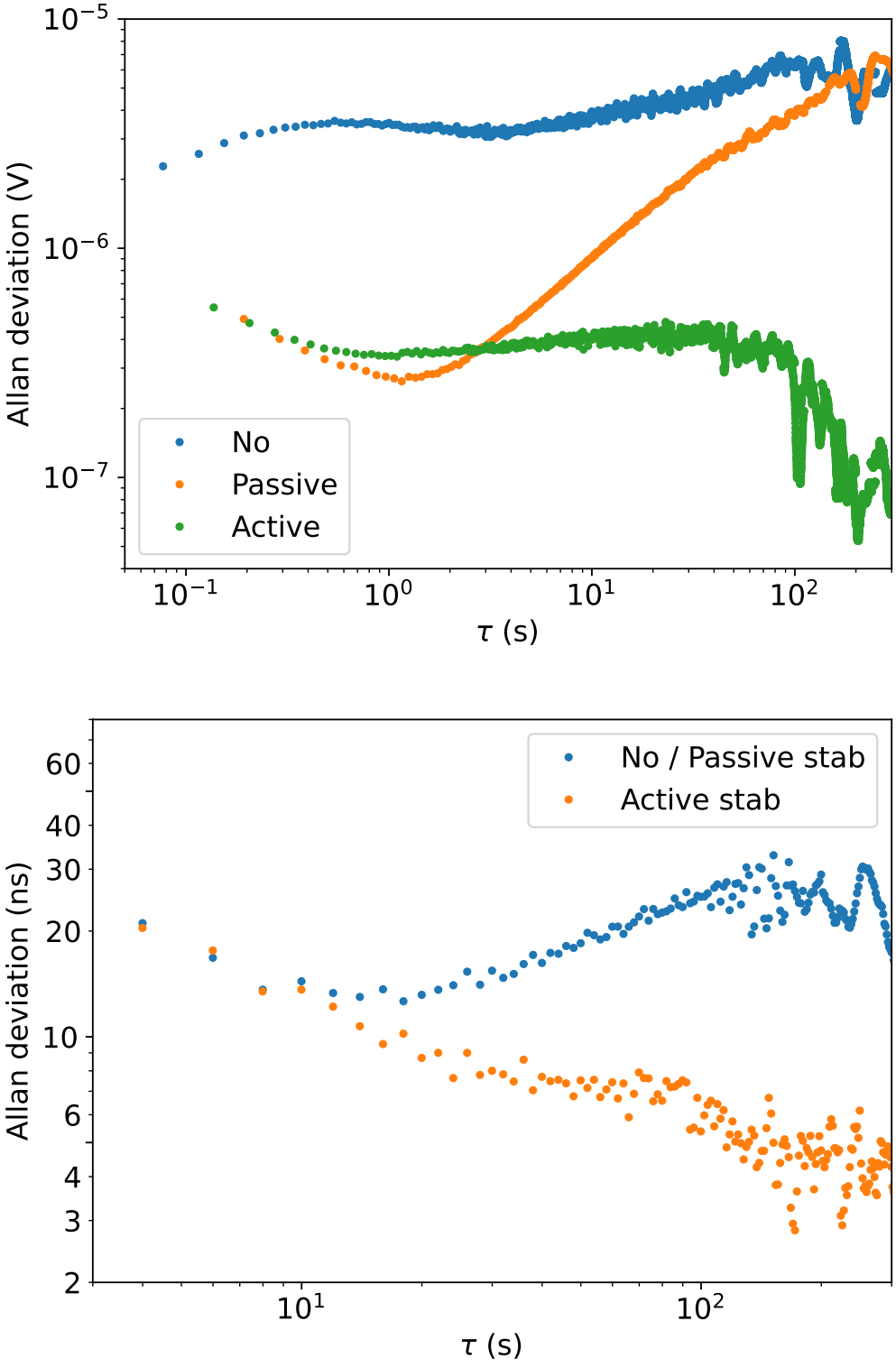

Fig. 6.8: Allan deviation over sample time of the voltage of mirror 4 (top) and the ion ToF signal (bottom). The deviation is calculated from the measurement data presented in Figure 6.6.

actively stabilized mirror voltage sources of noise and drifts other than unavoidable white noise are still present. The origin of those should be identified to potentially reduce fluctuations further.

The effect of the active voltage stabilization on the MIRACLS proof-of-principle experiment encourages the implementation of stabilization into the 30-keV MR-ToF device and Paul trap of the MIRACLS setup. Critical for the implementation is the identification of components such as precision voltage dividers and capacitors, that are rated for up to $60\,\mathrm{kV}$ as required by the beam energy of MIRACLS.

Furthermore, it needs to be studied how the stabilization influences the CLS signal, which will be the main measurement method for MIRACLS, opposed to the ion ToF measurements, that are conducted in this thesis.

7 Conclusion

In this thesis, the Paul trap for the MIRACLS experiment, currently under construction at the radioactive ion beam facility ISOLDE at CERN, was characterized in a simulation study. Furthermore, the Paul trap itself was constructed, as well as parts of a test beamline, where the experimental characterization of the Paul trap will take place in the very near future.

The MIRACLS experiment seeks to improve the sensitivity of collinear laser spectroscopy on exotic short-lived radionuclides by performing the measurements in an MR-ToF ion trap. In this novel approach, the ions are revolving inside the MR-ToF device and can be probed by the spectroscopy laser several thousand times, compared to only once in conventional single-passage collinear laser spectroscopy. The combination of the two techniques, collinear laser spectroscopy and MR-ToF ion trapping, imposes stringent requirements on the properties of the probed ion bunch: the time spread has to be small for a successful MR-ToF operation, and the energy spread has to be small to achieve good resolution in laser spectroscopy. For this purpose, a Paul trap has been designed, that will be used as a radiofrequency cooler and buncher, matching the properties of the radioactive ion beam supplied by ISOLDE to the requirements of the MIRACLS experiment.

The Paul trap is designed as a linear Paul trap with segmented DC electrodes, and cylinder sections as RF electrodes. The trap is operated with a square wave alternating voltage. The optimal operation parameters for this trap were studied in ion-optical simulations.

First, the reverse injection from an offline ion source installed on the beamline was simulated, which will be used for commissioning, setup, and reference measurements during online beamtimes at ISOLDE. Transfer efficiencies of 78% for stable $^{24}\mathrm{Mg}^{+}$ ions from the online ion source into the Paul trap were achieved. The trapping efficiency for reverse injection was studied as dependent on the helium buffer-gas pressure in the trap, the floating potential of the trap, and the parameters of the radial potential supplied by the RF electrodes. For maximal trapping efficiency, the buffer gas pressure in the trap has to exceed $4 \times 10^{-3}\,\mathrm{mbar}$. The floating potential of the trap should be slightly lower than the average beam energy of the ions, to allow most of the ions to enter the trap, but also to decelerate the ions sufficiently to be trapped. The exact floating potential has to be optimized for the buffer gas pressure used. For the two parameters of the RF potential, the amplitude and frequency of the supplied square wave, the resulting stability parameter q has been mapped and the resulting trapping efficiency analyzed. High trapping efficiencies have been found for q values between 0.3 and 0.6, especially in combination with amplitudes higher than $300\,\mathrm{V}$. Overall, trapping efficiencies of up to 97% of successfully injected ions could be achieved.

In the study of the cooling process of the ions, different equilibrium temperatures of the ion cloud were found in the longitudinal and the radial direction of motion. Due to RF reheating, the temperature in the radial direction is significantly higher ($\approx$ $1800\,\mathrm{K}$) than the temperature of the room-temperature buffer gas. In the longitudinal direction, a temperature of $340\,\mathrm{K}$, slightly above the buffer gas temperature was found, which can be possibly explained by redistribution of energy from radial direction to longitudinal direction in buffer-gas collisions and higher-order coupling of the motions. In the cooling process, the ions show an exponential decrease of energy over time. The half-time of this decay is inversely proportional to the buffer gas pressure, with faster cooling at higher pressure. Furthermore, the ion trajectories during and after cooling were simulated. It was shown that the motion corresponds to a high degree to the predicted frequencies in the longitudinal and radial direction and no distinct higher-order frequencies could be identified.

A central aspect of the Paul trap performance is the longitudinal emittance of the extracted bunches, a measure for the energy and time spread. The longitudinal emittance was studied systematically as dependent on the deepth parameter of the longitudinal trapping potential under different pressure and RF conditions. It was found, that a significant contribution to the longitudinal emittance is caused by collisions of the ions with buffer gas atoms during the ion extraction and acceleration process out of the Paul trap. It is therefore favorable to reduce the pressure for the extraction process or choose a reduced overall operation pressure, that still provides sufficient trapping efficiency and sufficiently fast cooling. Additionally, this reheating effect can be reduced by choosing a potential combination for ion trapping, in which the potential minimum is close to the extraction endcap, and/or choosing a slow extraction scheme. Different extraction schemes that provide either small energy spreads or small time spreads were presented. These simulations confirmed, that the extracted ion bunches are suitable for transfer through the MIRACLS beamline and storage in the MR-ToF device.

Finally, the vacuum system of the MIRACLS beamline was studied in a molecular flow simulation. It was concluded that the vacuum system and pumps planned for the beamline are sufficient to operate the Paul trap at optimal pressure and to reach the vacuum requirements of the ISOLDE beamline and the MIRACLS MR-ToF device.

Following this simulation study, the steps toward an experimental characterization of the Paul trap were outlined. As part of this work, the Paul trap was assembled, a first alignment of the trap inside the chamber performed, the electrical and gas system installed, and a test beamline designed. After the confirmation of final alignment, the Paul trap cross can be inserted in the test beamline, additionally hosting an ion source and ion detector, that will be used to characterize the performance of the Paul trap.

Finally, a technique to further increase the quality of the ion beam supplied of the Paul trap was studied. The Active Voltage Stabilization aims to increase the stability of the most sensitive beamline elements, by passively filtering the voltage from power supplies and regulating trends on longer time scales by a PI regulator. For collinear laser spectroscopy it is usually the floating potential of the Paul trap which defines the ion energy and, thus, has to be as stable as possible. The technique

was studied on the potentials of the electrostatic mirrors of the MR-ToF ion trap of the MIRACLS proof-of-principle experiment, where the highest impact of the stabilization was expected. Overall an improvement of ion signal stability of 36% was achieved, although the active voltage stabilization could not be applied fully to all four mirror electrodes due to missing suitable components. On a single electrode with full active voltage stabilization, an increase in voltage stability of 85% has been observed, which demonstrates the potential of this technique. This motivates the stabilization of all MR-ToF electrodes in future work as well as of the floating potential of the MIRACLS Paul trap.

Overall, the present work of simulation and construction of a compact, gas-filled Paul trap represents a critical milestone in the commissioning of the Multi-Ion Reflection Apparatus for Collinear Laser Spectroscopy (MIRACLS) at ISOLDE (CERN). Exploiting the Paul trap of this thesis as a cooler bucher of short-lived radionuclides will provide high quality ion beams to MIRACLS unique MR-ToF device. This will allow highly sensitive collinear measurements at MIRACLS currently out of reach in conventional, fluorescence based CLS. The present room-temperature Paul trap will be adequate for MIRACLS operation as demonstrated in this thesis for magnesium ions. To further improve the ion beam quality in the future, a cryogenic Paul trap has been designed as part of the MIRACLS project.

In the meantime, the present Paul trap will enable the first online MIRACLS measurements to determine nuclear ground state observables such as nuclear charge radii for nuclear structure research far away from stability. Additionally, copies of the same Paul trap, desgined at MIRACLS, will be used for the study of (radioactive) molecules at MIT, for ion cluster studies at the University of Greifswald and in the context of the PUMA experiment at CERN, which aims to employ antiprotons as probes to examine the surface of short-lived radionuclides. Thus, the present characterization work is relevant for several different fields of physics research.

Acknowledgment

Firstly, I would like to thank Dr. Stephan Malbrunot for giving me the opportunity to conduct my Master's thesis project at CERN. To the same extent, I would like to thank Prof. Dr. Peter Hommelhoff for supporting this undertaking from the side of the FAU. For overcoming the bureaucratic challenges for such a collaboration I would like to thank Prof. Dr. Stefan Funk and Dr. Adrian Zink from the Erlangen Centre for Astroparticle Physics (ECAP).

I would like to thank the complete MIRACLS group, from whom I learned a lot, and working together was always a pleasure. Especially I would like to thank Franziska, for teaching me how to operate the proof-of-principle setup, Simon, for the joint work on the Paul trap, and Markus for keeping us organized on the task of building a completely new beamline. Special thanks also go to summer student Moritz Epping, who supported me with great motivation with the construction work of the Paul trap. Finally, I would like to thank Ivana Belosevic for proof-reading this thesis.

I gratefully acknowledge the PROMOS scholarship by the German Academic Exchange Service (DAAD), supporting this project financially.

Bibliography

1. García Borge, M. J. & Blaum, K. Focus on exotic beams at ISOLDE: a laboratory portrait (2017).
2. *ISOLDE Logos, Layouts and Templates* http://isolde.web.cern.ch/isolde-logos-layouts-and-templates#.
3. Köster, U., Catherall, R., *et al.* Isomer separation and measurement of nuclear moments with the ISOLDE RILIS. *Hyperfine Interactions* **127,** 417–420 (2000).
4. Kugler, E. The ISOLDE facility. *Hyperfine interactions* **129,** 23–42 (2000).
5. Dean, D. J. *Beyond the nuclear shell model* Nov. 2007.
6. Hergert, H. A Guided Tour of ab initio Nuclear Many-Body Theory. *Frontiers in Physics* **8** (Oct. 2020).
7. Neugart, R., Billowes, J., *et al.* Collinear laser spectroscopy at ISOLDE: new methods and highlights. **44,** 064002 (Apr. 2017).
8. Foot, C. J. *et al. Atomic physics* (Oxford University Press, 2005).
9. Lechner, S., Xu, Z. Y., *et al.* Probing the single-particle behavior above $^{132}\mathrm{Sn}$ via electromagnetic moments of $^{133,134}\mathrm{Sb}$ and $N = 82$ isotones. *Phys. Rev. C* **104,** 014302 (1 July 2021).
10. Kaufman, S. High-resolution laser spectroscopy in fast beams. *Optics Communications* **17,** 309–312 (1976).
11. Sels, S., Fischer, P., *et al.* First steps in the development of the multi ion reflection apparatus for collinear laser spectroscopy. *Nuclear Instruments and Methods in Physics Research Section B: Beam Interactions with Materials and Atoms* **463,** 310–314 (2020).
12. Haller, V., Stepman, H., *et al. MIRACLS Experiment* miracls.web.cern.ch/experiment.html (Sept. 3, 2021).
13. Wolf, R. N., Marx, G., *et al.* Static-mirror ion capture and time focusing for electrostatic ion-beam traps and multi-reflection time-of-flight mass analyzers by use of an in-trap potential lift. *International Journal of Mass Spectrometry* **313,** 8–14 (2012).

14. Wolf, R., Beck, D., *et al.* On-line separation of short-lived nuclei by a multi-reflection time-of-flight device. *Nuclear Instruments and Methods in Physics Research Section A: Accelerators, Spectrometers, Detectors and Associated Equipment* **686,** 82–90 (2012).

15. Rosenbusch, M., Wada, M., *et al. The new MRTOF spectrograph for nuclear masses following RIBF's ZeroDegree spectrometer, featuring new methodologies for ion selection and mirror optimization* 2021.

16. Maier, F. *Laser Spectroscopy of Short-Lived Radionuclides in an Ion Trap: MIRACLS' proof-of-principle experiment and the simulation of the future 30-keV MR-ToF device* 2019.

17. Vilén, M., Malbrunot-Ettenauer, S., *et al. MIRACLS at ISOLDE: The Charge Radii of Exotic Magnesium Isotopes* tech. rep. (2020).

18. Paul, W. *Electromagnetic traps for charged and neutral particles* https://www.nobelprize.org/uploads/2018/06/paul-lecture.pdf (Sept. 4, 2021).

19. Heinrich, J. *A Be+ ion trap for H2+ spectroscopy* PhD thesis (Sorbonne université, 2018).

20. Herfurth, F., Dilling, J., *et al.* A linear radiofrequency ion trap for accumulation, bunching, and emittance improvement of radioactive ion beams. *Nuclear Instruments and Methods in Physics Research Section A: Accelerators, Spectrometers, Detectors and Associated Equipment* **469,** 254–275 (2001).

21. Kłosowski, Ł., Piwiński, M., *et al.* Nonlinear resonances in linear segmented Paul trap of short central segment. *Journal of Mass Spectrometry* **53,** 541–547 (2018).

22. Ding, L. & Kumashiro, S. Ion motion in the rectangular wave quadrupole field and digital operation mode of a quadrupole ion trap mass spectrometer. *Rapid Communications in Mass Spectrometry: An International Journal Devoted to the Rapid Dissemination of Up-to-the-Minute Research in Mass Spectrometry* **20,** 3–8 (2006).

23. Smith, M. J. *A mass measurement of the short-lived halo nucleus 11Li with the TITAN Penning trap spectrometer* PhD thesis (University of British Columbia, 2008).

24. Ding, L., Sudakov, M., *et al.* A digital ion trap mass spectrometer coupled with atmospheric pressure ion sources. *Journal of mass spectrometry : JMS* **39,** 471–84 (May 2004).

25. Delahaye, P. Analytical model of an ion cloud cooled by collisions in a Paul trap. *The European Physical Journal A* **55,** 1–12 (2019).

26. *The Nobel Prize in Physics 1997* https://www.nobelprize.org/prizes/physics/1997/summary/ (Oct. 29, 2021).

27. Borisenko, A., Zalivako, I., *et al.* Motional states of laser cooled Yb ions in an optimized radiofrequency trap. **29,** 095201 (July 2019).

28. Fan, M., Holliman, C. A., *et al.* Laser Cooling of Radium Ions. *Phys. Rev. Lett.* **122,** 223001 (22 June 2019).

29. Sakemi, Y., Harada, K.-i., *et al.* in *Proceedings of 10th International Conference on Nuclear Physics at Storage Rings (STORI'17)* ().

30. Sels, S., Maier, F. M., *et al. Doppler-and sympathetic ion cooling for the investigation of short-lived radionuclides* In preparation. 2021.

31. Ryjkov, V. L. *Laser cooling and sympathetic cooling in a linear quadrupole RF Trap* (Texas A&M University, 2003).

32. Reiser, M. *Theory and design of charged particle beams* (John Wiley & Sons, 2008).

33. Barquest, B. R. *An advanced ion guide for beam cooling and bunching for collinear laser spectroscopy of rare isotopes* (Michigan State University, 2014).

34. Moore, R. B., Dezfuli, A. M. G., *et al.* Production, transfer and injection of charged particles in traps and storage rings. **T59,** 93–105 (Jan. 1995).

35. Lechner, S. *Laser Spectroscopy of Antimony Isotopes and the Design of a Cryogenic Paul Trap* disertation (Vienna University of Technology, 2021).

36. Scientific Instrument Services, Inc. *SIMION* 2020.

37. Scientific Instrument Services, Inc. *Collision Model HS1* 2020.

38. Sailer, S. *Improvements of the Optical Detection Setup for Collinear Laser Spectroscopy of Short-Lived Radioactive Nuclides and Spectroscopic Studies on the Hyperfine Parameters of 208Bi* PhD thesis (Technical University Munich, 2016).

39. Scientific Instrument Services, Inc. *simionx.SimplexOptimizer - Simplex optimizer* 2020.

40. National Nuclear Data Center, Brookhaven National Laboratory. *NuDat 2.8* https://www.nndc.bnl.gov/nudat2/ (Nov. 2, 2021).

41. Lagaki, V., Heylen, H., *et al.* An accuracy benchmark of the MIRACLS apparatus: Conventional, single-passage collinear laser spectroscopy inside a MR-ToF device. *Nuclear Instruments and Methods in Physics Research Section A: Accelerators, Spectrometers, Detectors and Associated Equipment* **1014,** 165663 (2021).

42. Maier, F. M. *Personal communication* 2021.

43. Siesling, E. *Personal communication* 2021.

44. Kersevan, R., Ady, M., *et al. Recent developments of Monte-Carlo codes molflow+ and synrad+* in *Proceedings of the 10th International Particle Accelerator Conference (IPAC'19), Melbourne, Australia* (2019), 19–24.

45. Schwarz, S. IonCool—A versatile code to characterize gas-filled ion bunchers and coolers (not only) for nuclear physics applications. *Nuclear Instruments and Methods in Physics Research Section A: Accelerators, Spectrometers, Detectors and Associated Equipment* **566,** 233–243 (2006).

46. Sida, D. W. The scattering of positive ions by neutral atoms. *The Philosophical Magazine: A Journal of Theoretical Experimental and Applied Physics* **2,** 761–771 (1957).

47. Lunney, M. & Moore, R. Cooling of mass-separated beams using a radiofrequency quadrupole ion guide11Dedicated to J.F.J. Todd and R.E. March in recognition of their original contributions to quadrupole ion trap mass spectrometry. *International Journal of Mass Spectrometry* **190-191,** 153–160 (1999).

48. Brice, M. *Paul trap for the MIRACLS experiment* 2021.

49. Stresau, D., Hunter, K., *et al. A new class of robust sub-nanosecond TOF detectors with high dynamic range* in *54 th ASMS Conference Proceedings* (2006).

50. Iseg Spezialelektronik GmbH. *EBS - Bipolar 4 Quadrant High Voltage Module with Common Floating Ground (CFG)* 2021.

51. Wienholtz, F., Blaum, K., *et al.* Improved stability of multi-reflection time-of-flight mass spectrometers through passive and active voltage stabilization. *Nuclear Instruments and Methods in Physics Research, Section B: Beam Interactions with Materials and Atoms* (May 2019).

52. Riley, W. J. *Handbook of frequency stability analysis* (US Department of Commerce, National Institute of Standards and Technology, 2008).

53. Niu, X., Chen, Q., *et al.* Using Allan variance to analyze the error characteristics of GNSS positioning. *GPS Solutions* **18** (Apr. 2014).

Eigenständigkeitserklärung

Hiermit bestätige ich, dass ich diese Arbeit selbstständig und nur unter Verwendung der angegebenen Hilfsmittel angefertigt habe.

Genf, den 04.11.2021 Carina Kanitz